

EPITAXIAL GROWTH AND SURFACE MORPHOLOGY  
OF SOME  
METAL AND SEMICONDUCTOR STRUCTURES

by

Andrew David Johnson

A thesis submitted to the University of Leicester  
for the degree of Doctor of Philosophy

July 1989

UMI Number: U497028

All rights reserved

INFORMATION TO ALL USERS

The quality of this reproduction is dependent upon the quality of the copy submitted.

In the unlikely event that the author did not send a complete manuscript and there are missing pages, these will be noted. Also, if material had to be removed, a note will indicate the deletion.



UMI U497028

Published by ProQuest LLC 2015. Copyright in the Dissertation held by the Author.  
Microform Edition © ProQuest LLC.

All rights reserved. This work is protected against  
unauthorized copying under Title 17, United States Code.



ProQuest LLC  
789 East Eisenhower Parkway  
P.O. Box 1346  
Ann Arbor, MI 48106-1346



7500478413

x751593485

# EPITAXIAL GROWTH AND SURFACE MORPHOLOGY OF SOME

## METAL AND SEMICONDUCTOR STRUCTURES

by A.D.Johnson

### ABSTRACT

Forward focussing of medium energy Auger and photoelectrons have been used along with LEED and Auger electron spectroscopy to investigate the initial stages of growth of both Cr and Co on Ag(001). Cr was found to grow epitaxially on Ag in the bcc phase up to ~2ML, in agreement with previous results. Co also grows epitaxially on Ag up to 3ML although it is proposed that the Co lattice is in the FCC phase but no comment can be made as to whether the overlayer is laterally expanded.

Polarised Neutron Reflection measurements have been made on Ag/Cr/Ag sandwich structures with varying thicknesses of Cr. It is shown that for Cr thicknesses of 2 and 3.3ML the Cr is ordered non-ferromagnetically and it is proposed that at these thicknesses the Cr has reverted to its bulk antiferromagnetic order. However measurements on samples with Cr thicknesses of 0.33ML indicate ferromagnetic ordering with a greatly enhanced magnetic moment per atom over the bulk Cr value, in partial agreement with previous theoretical predictions. PNR measurements on a Ag/Fe/Ag(001) structure with thickness of Fe of 8ML have yielded an accurate measurement of the magnetic moment per atom for the Fe film of  $1.0 \pm 0.15\mu_B$ , indicating a reduced value from that of bulk Fe of  $2.22\mu_B$ .

X-ray scattering from a Ge(001) surface has been used to show that the surface undergoes a reversible phase transition at  $T = 954 \pm 7K$ . It is proposed that the transition occurs due to the formation of vacancy-adatom pairs as some of the surface dimers break with increasing temperature. The data is explained in terms of a three level model used to describe the vacancy-adatom creation. The three level model results are compared with results from a simple Monte-Carlo simulation and an energy of  $0.41 \pm 0.05eV$  is deduced as the energy required to break the dimer bonds on the surface of Ge(001). Further X-ray scattering from a miscut Ge(001) surface shows that the surface is made up of regularly spaced steps of double atomic height, in agreement with theoretical and previous experimental studies. It is shown that perpendicular to the steps the reconstructed domains are limited in dimension by the steps, although both orientations of the reconstruction are possible

## ACKNOWLEDGEMENTS

Many thanks must be expressed to Dr C Norris for his supervision and suggestions during the course of this work and special mention must also be made of Dr C Binns for many useful discussions and the use of many of his data acquisition programs.

For the Neutron Reflection work undertaken at Grenoble I am indebted to Dr J A C Bland from the Cavendish Laboratory for introducing me to the technique and all his help during both the experiments and the data analysis. I must also thank the staff of the I.L.L. Grenoble, especially Dr H J Lauter, for all of their valuable assistance.

The X-ray Diffraction measurements made at Daresbury Laboratory have been very much a team effort and I express my gratitude to the groups from FOM Institute Amsterdam and University College Cardiff for all their assistance. I must make special mention of Prof J F Van Der Veen of the FOM Institute for the use of his UHV chamber for the experiments and for the loan of Ge(001) samples.

There has been much development of equipment at Leicester and none of this could have been possible without the excellent technical support of Mr J S G Taylor and Mr S C Thornton and the Leicester Physics Department mechanical and electronic workshops. I also would like to acknowledge Mrs R Christmas for the careful drawing of many of the diagrams in this thesis.

Finally, the deepest thanks of all must go to my parents for their interest, advice and encouragement in everything that I have undertaken in the last twenty-five years; I cannot thank them enough.

## CONTENTS

	<u>Page</u>
CHAPTER 1 : INTRODUCTION	1
CHAPTER 2 : BASIC THEORY	5
2.1 Introduction	6
2.2 Auger Electron Spectroscopy	7
2.2.1 The Auger Process	7
2.2.2 Monitoring Overlayer Growth With The A-st Plot	8
2.3 Surface Structure Determination With Forward Focussing Of Medium Energy Electrons	10
2.3.1 Scattering Of Electrons By Atoms	10
2.3.2 Structure Determination	12
2.3.3 Choice Of Suitable Electron Series	14
2.4 The Study Of Magnetic Layers Using Polarised Neutron Reflection	15
2.4.1 Neutron Refractive Index For A Ferromagnet	15
2.4.2 Neutron Reflectivity	17
2.5 The Study Of Surfaces With X-ray Diffraction	20
2.5.1 Critical Angle And Refractive Index	21
2.5.2 Basic Diffraction Theory	22
2.5.3 Surface X-ray Diffraction	25
2.5.4 Integrated Intensity	25
CHAPTER 3 : EXPERIMENTAL DETAILS	28
3.1 Introduction	29
3.2 Angle Resolved XPS/AES	30
3.2.1 UHV System	30

3.2.2	Sample Manipulator	31
3.2.3	LEED And Auger Electron Spectroscopy	31
3.2.4	X-ray And UV Photon Sources	33
3.2.5	Hemispherical Electron Analyser	34
3.2.6	Data Acquisition System	37
3.2.7	Sample Preparation	38
3.2.8	Vapour Sources	39
3.3	Polarised Neutron Reflection Measurements	39
3.3.1	Experimental Arrangement	39
3.3.2	Sample Preparation	40
3.4	Surface X-ray Diffraction Measurements	41
3.4.1	Synchrotron Radiation	41
3.4.2	Beamline And X-ray Monochromator	42
3.4.3	Surface X-ray Diffraction UHV Chamber	43
3.4.4	5-Circle Diffractometer And Sample Alignment	44
3.4.5	Data Acquisition	45
3.4.6	Sample Preparation	46
 <b>CHAPTER 4 : THE INITIAL STAGES OF THE GROWTH OF Cr AND Co ON Ag(001)</b>		<b>47</b>
<b>STUDIED USING FORWARD FOCUSING OF MEDIUM ENERGY ELECTRONS</b>		
4.1	Introduction	48
4.2	Epitaxial Growth Of Cr On Ag(001)	49
4.2.1	Introduction	49
4.2.2	LEED And As-t Results	51
4.2.3	Polar Angle Auger Electron Intensity Results	52
4.2.4	Discussion	55
4.3	Epitaxial Growth Of Co On Ag(001)	56
4.3.1	Introduction	56
4.3.2	LEED And As-t Results	59
4.3.3	Polar Angle Auger Electron Intensity Results	60

4.3.4	Discussion	63
4.4	Summary	65
CHAPTER 5 : POLARISED NEUTRON REFLECTION STUDIES OF THE MAGNETIC ORDERING OF Ag/Cr/Ag(001) and Ag/Fe/Ag(001) SANDWICH STRUCTURES		67
5.1	Introduction	68
5.2	Magnetic Ordering Of Cr In Ag/Cr/Ag(001) Structures	69
5.2.1	Introduction	69
5.2.2	PNR Results	72
5.2.3	Discussion	75
5.3	Magnetic Ordering Of Fe In An Ag/Fe/Ag(001) Structure	77
5.3.1	Introduction	77
5.3.2	PNR Results	80
5.3.3	Discussion	82
5.4	Summary	83
CHAPTER 6 : X-RAY SCATTERING FROM Ge(001) SURFACES		85
6.1	Introduction	86
6.2	Thermal Disordering Of The Surface Of Ge(001)	87
6.2.1	Introduction	87
6.2.2	Results	88
6.2.3	Three Level Model	96
6.2.4	Monte-Carlo Simulation	99
6.2.5	Discussion	99
6.3	X-ray Scattering From A Vicinal Ge(001) Surface	100
6.3.1	Introduction	100
6.3.2	Results	101
6.3.3	Discussion	106
6.4	Summary	107

<b>CHAPTER 7 : SUMMARY AND SUGGESTIONS FOR FUTURE WORK</b>	<b>109</b>
7.1 Introduction	110
7.2 Overlayer Growth	110
7.3 Polarised Neutron Reflection Results	112
7.4 X-ray Scattering Results	113
7.5 Suggestions For Future Work	114
<b>REFERENCES</b>	<b>117</b>

## CHAPTER 1

### INTRODUCTION

The termination of a crystal at its surface can induce many unique properties not associated with the bulk. The most obvious case is the formation of surface reconstructions with unit cell arrangements which differ from the underlying lattice. Moreover, the reduced coordination number at the surface and surface strain can lead to changes in electronic structure with consequent changes in properties such as magnetism (see Klebanoff et al, 1984 for Cr(001)).

Ultrathin layers of metals supported on oriented metallic and semiconductor substrates are a special class of adsorbate systems of particular technological and fundamental interest. They offer the possibility of exploring new physics associated with reduced dimensionality, interlayer coupling, superlattices and metastable phases and, in consequence, of engineering new materials on an atomic scale for specific applications.

The 3d transition metals have received much attention in view of their itinerant magnetic behaviour and coverage sensitivity to structural rearrangements. Strikingly different magnetic properties have been predicted theoretically for such layers adsorbed onto noble metal substrates (Fu et al, 1985). The intimate relationship between layer morphology and such magnetic character emphasises the need for good growth conditions and an accurate knowledge of local atomic order. For example, Co which is HCP in the bulk, grows epitaxially as BCC on GaAs(110) (Prinz, 1985) and FCC on Cu(001) (Gonzalez et al, 1981). Thus by controlled epitaxial growth with artificially increased atomic volume

(negative pressure) it should be possible to increase the magnetic moment of such structures with consequent technological implications. This thesis describes a study of such transition metal overlayers and a determination of both their structural and magnetic properties.

The most widely used techniques in the study of ultrathin metal overlayers are low energy electron diffraction (LEED) and Auger electron spectroscopy (AES), which have both been used in this work to study the initial growth of 3d transition metals on Ag(001). It has been shown that photoelectrons and Auger electrons with kinetic energies of above ~300eV can be focussed along major internuclear axes of overlayer lattices (Egelhoff, 1984) and can thus be used to give information on the structure of the overlayer and the initial stages of its growth. This technique has been used to monitor the growth of Cr and Co layers deposited on Ag(001) held at room temperature.

Cr has been previously studied on both Ag and Au(001), but there is still controversy about both its structure and magnetic properties. The present study makes important proposals about both such properties. Co on the other hand, has not previously been studied on Ag(001) but as it has been shown to grow epitaxially in metastable phases on Cu and GaAs, it was hoped that like other 3d transition metals it would grow epitaxially in the BCC phase on Ag(001).

Direct quantitative measurements of the magnetic moments of such ultrathin films (and surfaces) are difficult, with consequent dispute about their accuracy. Felcher (1982), has shown that by using a polarised beam of neutrons it is possible to directly measure the ferromagnetic moments of such structures by collecting the reflected neutron beam near the critical angle for total external reflection. The large penetration

depth of neutrons is overcome by the grazing incidence angle which preferentially illuminates the surface and creates surface sensitivity. This technique has been used to study the magnetic ordering of ultrathin Cr and Fe layers in Ag/Cr/Ag(001) and Ag/Fe/Ag(001) sandwich structures.

X-ray diffraction has been the most widely used probe of the structure of bulk crystals for over seventy years. By making a highly collimated X-ray beam incident on a crystal at a grazing angle near the critical angle, the surface region of the crystal becomes illuminated and, as with neutrons, surface sensitivity is achieved. This technique has been used to study the surface of the (001) face of Ge.

Ge is an elemental semiconductor with a structure very similar to Si. Most work on Ge surfaces has centred on the energetically more stable (111) face but more and more work is being undertaken on the (001) surface as it becomes better understood. The main impetus behind the present X-ray study was to understand thermal disordering on the surface with the possibility of surface roughening, melting and vacancy creation. Such disordering events represent two dimensional phase behaviour and the corresponding phase transitions play a critical role in the theory of critical phenomena (Bauer, 1987). The report of a surface phase transition on Ge(111) at 150K below its bulk melting temperature (McRae and Malic, 1987) gave added incentive to the present study as it was of interest to see whether a similar transition would occur on the (001) face.

Further X-ray scattering measurements on a vicinal Ge surface were undertaken in order to compare with previous theoretical and experimental studies on both Si and Ge(001) such surfaces. Such surfaces, by their nature, create a large number of steps which are of particular interest

in the stabilisation of highly ordered layers of III-V semiconductor layers and alloy semiconductor structures on Si and Ge(001). Thus the atomic structure of such steps and their effect on surface morphology must be accurately determined before such overlayers can be grown. The high resolution of X-ray diffraction makes it an ideal technique to study such surfaces. Moreover, the single scattering (kinematical) analysis of X-ray diffraction measurements makes such experiments much easier to interpret.

An outline to the theory of the electron spectroscopies used in the study of overlayer growth is given in chapter 2 of this thesis, along with the basic theory of polarised neutron reflection (PNR) and surface X-ray diffraction (SXRD). Chapter 3 explains the experimental details involved with the above techniques including equipment that was specially designed for specific purposes. The growth and overlayer structure of Cr/Ag(001) and Co/Ag(001) determined with forward focussing of medium energy Auger electrons are described in chapter 4. The magnetic ordering of Ag/Cr/Ag(001) and Ag/Fe/Ag(001) sandwich structures by polarised neutron reflection is presented in chapter 5 and X-ray scattering from both flat and vicinal Ge(001) surfaces is described in chapter 6.

A brief summary with some general comments is presented in chapter 7 along with some suggestions for future experiments, followed by a list of references used in this work.

## CHAPTER 2

### BASIC THEORY

#### 2.1 Introduction

#### 2.2 Auger Electron Spectroscopy

##### 2.2.1 The Auger Process

##### 2.2.2 Monitoring Overlayer Growth With The As-t Plot

#### 2.3 Surface Structure Determination With Forward Focussing Of Medium Energy Electrons

##### 2.3.1 Scattering Of Electrons By Atoms

##### 2.3.2 Structure Determination

##### 2.3.3 Choice Of Suitable Electron Series

#### 2.4 The Study Of Magnetic Layers Using Polarised Neutron Reflection

##### 2.4.1 Neutron Refractive Index For A Ferromagnet

##### 2.4.2 Neutron Reflectivity

#### 2.5 The Study Of Surfaces With X-ray Diffraction

##### 2.5.1 Critical Angle And Refractive Index

##### 2.5.2 Basic Diffraction Theory

##### 2.5.3 Surface X-ray Diffraction

##### 2.5.4 Integrated Intensity

## CHAPTER 2

### BASIC THEORY

#### 2.1 INTRODUCTION

Electrons have been widely used in surface analysis for many years. This is because the mean free path for inelastic scattering is short enough that the electrons which escape without energy loss must have originated in the first few layers of the sample (see figure (2.1)). Low energy electron diffraction (LEED) and Auger electron spectroscopy (AES) are two of the most widely used techniques in the study of surfaces.

The interaction of Neutrons and X-rays with matter is much weaker and the radiation is far more penetrating into solids, but by using an angle of incidence close to that for total external reflection surface sensitivity can nevertheless be achieved. The ferromagnetic moments of surfaces, overlayers or buried layers can be measured by Polarised Neutron Reflection (PNR) by utilizing the magnetic interaction between an incident neutron and that magnetic moment. Surface X-ray diffraction (SXRD) has been used to solve surface structures and to provide information about surface morphology on a range of semiconductor and metallic surfaces (see Feidenhans'1 1986 and references therein).

A kinematical or single scattering approach can be used to describe the scattering of neutrons and X-rays by a surface. This simplifies data analysis and contrasts with the interpretation of electron diffraction in which multiple scattering must be included. For relatively high energy electrons (>500eV), a single scattering approximation can be used. This chapter will describe the underlying theory used in the PNR and SXRD techniques, and also how focussing of relatively high energy electrons

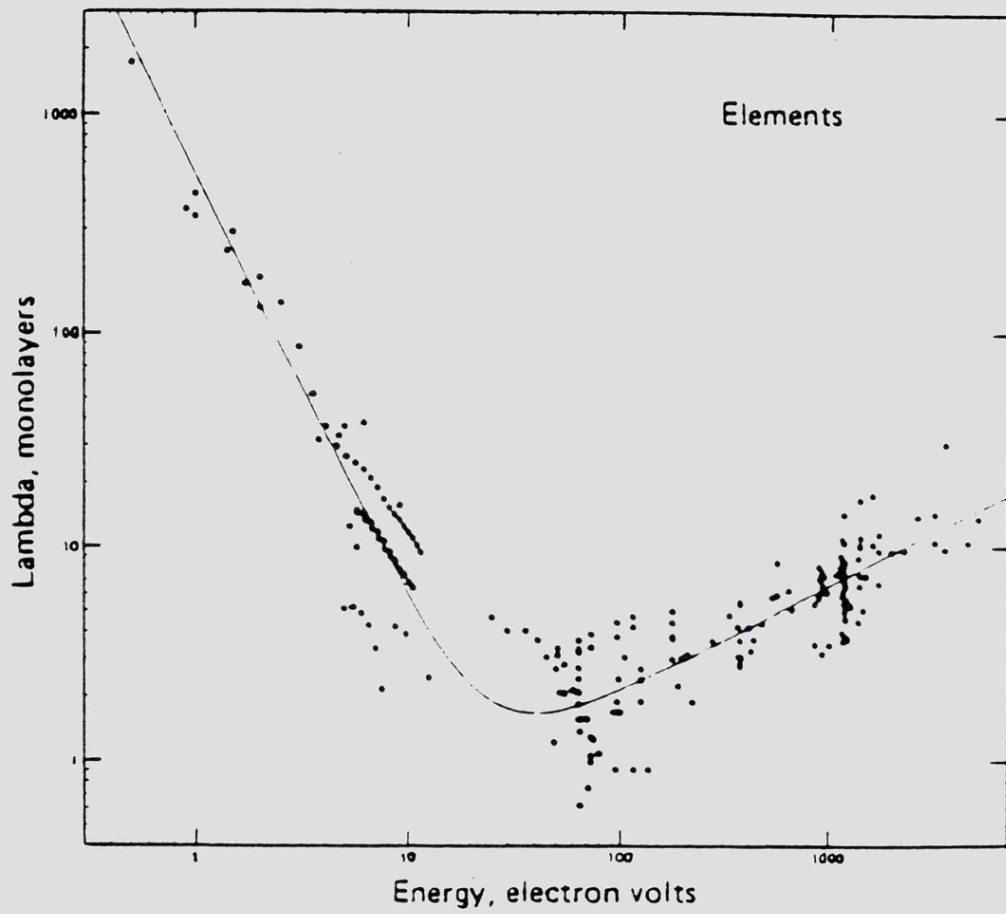


Figure (2.1) Inelastic mean free paths for the elements, from Seah and Dench (1979).

can be used in the study of the initial stages of epitaxial growth.

## 2.2 AUGER ELECTRON SPECTROSCOPY (AES)

The Auger process was first recognised by Pierre Auger in 1925. Following Harris(1968), who noted that increased sensitivity could be obtained by differentiating the Auger signal, AES has become one of the most widely used techniques in surface analysis.

### 2.2.1.THE AUGER PROCESS

Auger electrons are emitted after a core hole is created when an atom is ionised, either by a photon (X-ray) or a sufficiently high energy electron. The hole is eventually filled by an electron from a shallow energy level, together with the emission of energy, and the energy release is taken up either by the creation of a photon or the excitation of another electron (see figure (2.2)). The photon emission process dominates if the initial core hole is deeper than ~10KeV (this is the process used in conventional laboratory X-ray tubes). At lower energies the electron emission process is more probable.

A particular Auger emission is denoted by  $A_{pqr}$ , where A is the initial core level (K,L,M etc. using standard X-ray notation), B is the level from which the hole is filled and C the level from which the electron is emitted. The relevant quantum numbers of these levels are represented by p,q and r. For example,  $L_1$  is the 2s level,  $L_{2,3}$  the  $2p_{1/2}$  and  $2p_{3/2}$  levels, and so on. A and/or B may be levels in the valence band, in which case each valence level is given the label V, with the suffix omitted.

As the emitted electrons have energies defined by the energy levels involved in their production, each element has its own characteristic

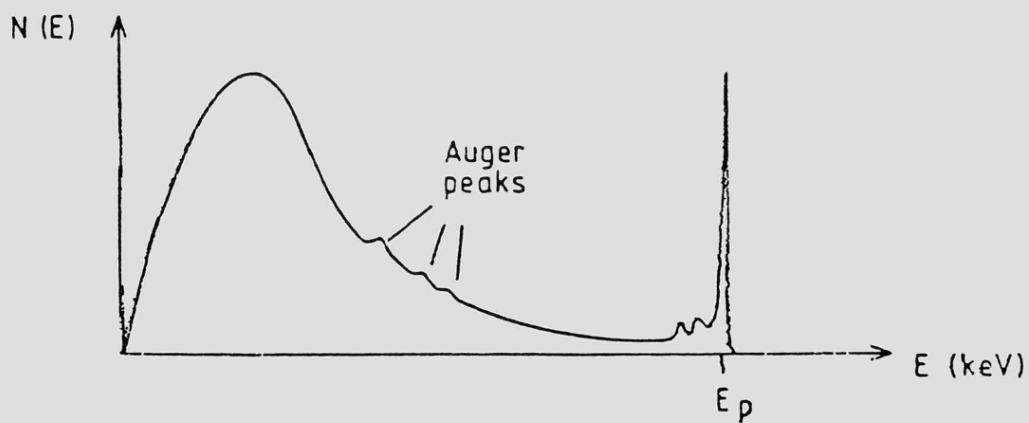
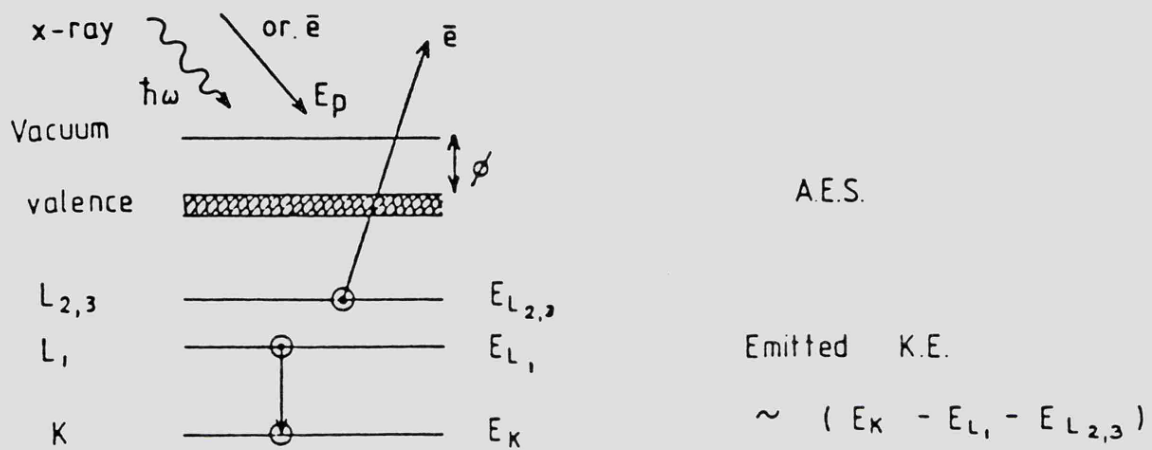


Figure (2.2) The Auger process for a metal with energies referred to the vacuum level and  $\phi$  is the work function.

Auger spectrum. As a result, AES has become widely used for surface chemical analysis and monitoring overlayer growth. Although Auger electrons can easily be produced with X-rays, it is more usual for electron beams to be used because of the ease with which such beams can be produced (~1.5–5KeV, 1–100 $\mu$ A).

Ignoring the work function  $\phi$ , an approximate expression for the kinetic of an emitted ABC Auger electron can be given by:-

$$KE = E_a^z - \frac{1}{2}(E_b^z + E_b^{z+1}) - \frac{1}{2}(E_c^z + E_c^{z+1}) \quad - (2.1)$$

where z is the atomic number. such expressions were widely used in the early days of surface science, but today collections of standard spectra for all of the elements are readily available (e.g. Davis et al 1976).

### 2.2.2. MONITORING OVERLAYER GROWTH WITH THE As-t PLOT

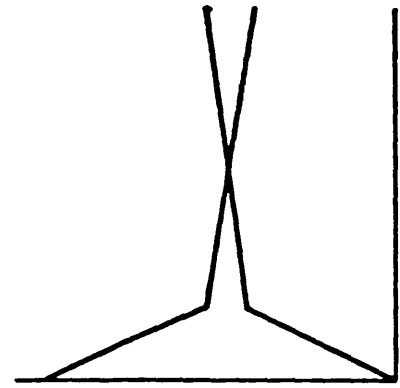
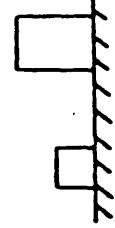
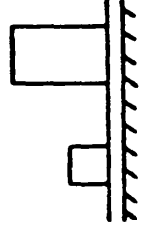
By monitoring the Auger electron intensity from the substrate or the adsorbate during overlayer growth, one can produce important information as to the structure and growth mode of that overlayer. The subsequent Auger signal-time plot (As-t plot) can take many forms, subject to the growth mechanism.

Figure (2.3) shows the three basic growth mechanisms and their corresponding As-t plots. The Volmer-Weber (VW) growth mode shows a distinctive As-t plot where both the substrate and overlayer signals change very slowly with no break in the curve. This corresponds to the adsorbate atoms nucleating to form islands or crystallites with no monolayer formation. The islands grow in size due to surface diffusion of the incoming adsorbate atoms.

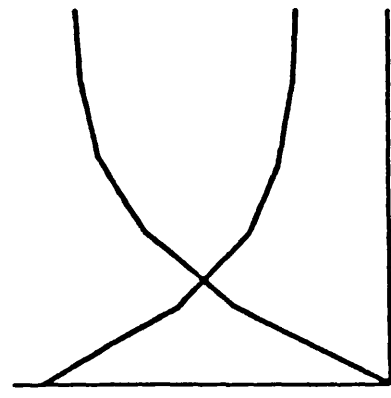
Volmer - Weber

Frank - van der Merwe

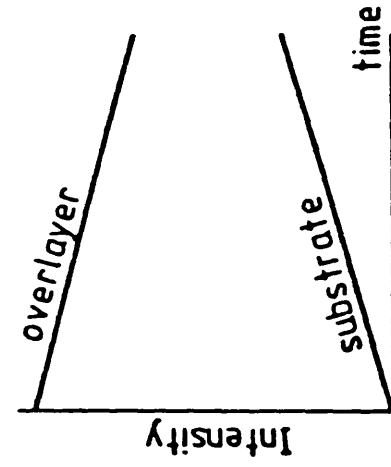
Stranski - Krastanov



island growth on adsorbed layer



layer growth



island growth on substrate

Figure (2.3) Three typical growth modes and their corresponding As-t plots.

Frank-van der Merwe (FM) growth gives an As-t plot comprised of a series of straight lines interconnected by well defined (and usually equally spaced in time) breaks in the curve. Each break implies the completion of a layer and the beginning of the next, i.e. layer by layer growth. The Stranski-Krastanov (SK) growth mechanism is indicated by a horizontal or slowly varying plateau in the As-t plot following a sharp break in the curve. This often suggests that island formation is occurring after the formation of one (or possibly more) monolayers.

These three growth modes are a simplification of what can happen in practise and variations on them can be observed. For example, with 'simultaneous multilayer' (SM) (see Barthès and Rolland, 1981), both the adsorbate and substrate Auger signals appear as exponential curves. SM and FM growth modes can easily be mistaken, as for example the breaks in some FM curves are often rounded due to changes in the sticking coefficient.

It is difficult to predict which particular growth mode will occur for a particular adsorbate - substrate system. Growth can be influenced by many parameters, e.g. substrate temperature, substrate flatness, substrate cleanliness, pressure, evaporation rate, lattice mismatch and substrate orientation etc. The As-t plot can, however, often indicate the growth mode for the first few layers of a particular system. It can also be used to deposit a particular thickness of adsorbate to an accuracy of within ~2% of a monolayer. The As-t plot is normally used in conjunction with Low Energy Electron Diffraction (LEED) as a standard LEED optics system can easily be modified into a retarding field analyser (see section 3.2.3 of this thesis). Thus it is possible to get further information on the surface atomic periodicity by depositing to a given overlayer thickness using the As-t plot and then studying the resulting

surface with LEED.

### 2.3. SURFACE STRUCTURE DETERMINATION WITH FORWARD FOCUSING OF MEDIUM ENERGY ELECTRONS

The use of forward focussed electrons for structure determination of the initial stages of epitaxial growth was first demonstrated by Egelhoff (1984). It was shown that focussing of high energy Auger or photoelectrons along major interatomic axes in a crystal by the atomic potentials could be used to determine relative atomic positions. The analysis is straightforward and the method makes use of equipment that is readily available in many surface science laboratories.

#### 2.3.1. SCATTERING OF ELECTRONS BY ATOMS

When an electron is scattered by the atoms in a solid, the scattering process changes the amplitude and phase of the scattered electron wave. These changes depend on the wavelength  $\lambda$ , the identity of the scattering atom and on its position. By measuring the angular distribution of scattered electrons it is possible to obtain information about the scattering centres and their positions.

Figure (2.4) is a diagram of the results of a calculation undertaken by Kono et al (1978,1980). It shows the polar intensity of Oxygen 1s electrons emitted with a kinetic energy of 965eV, after scattering by a single Cu atom placed 5Å from the emitter. The intensity is plotted against scattering angle  $\theta$ , measured between the incident and scattered electrons;  $\theta=0^\circ$  corresponds to forward scattering whilst  $\theta=180^\circ$  corresponds to back scattering. There is a sharp intensity peak along the O-Cu axis with full width at half maximum (FWHM) of  $12^\circ$  and a peak intensity that is  $\sim 3x$  stronger than the primary intensity (the circle in figure (2.4)). Aside from the region  $\theta \leq 30^\circ$ , there is no modulation of the

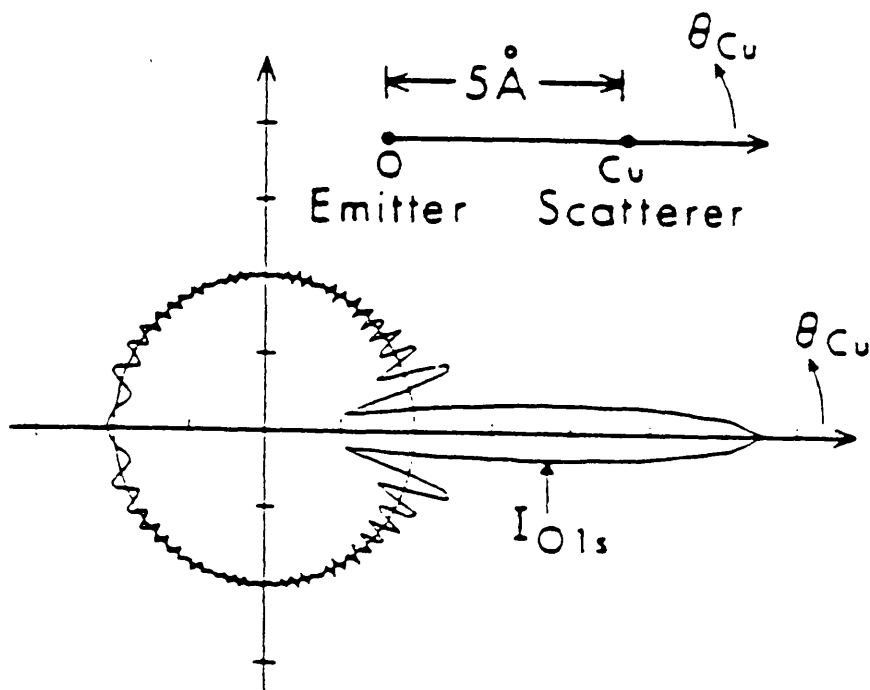


Figure (2.4) Polar intensity of an O 1s electron with kinetic energy 965eV incident on a single Cu atom, after Kono et al (1980).

primary energy greater than 10%. Kono et al found that the forward scattered intensity was strongly dependent on the O-Cu distance; for a distance of 15Å, the forward intensity is ~50% of the primary intensity, but rises to ten times the primary intensity for a O-Cu distance of 2Å.

A simple but effective model of electron scattering by atoms has been developed by Fadley and co-workers for studying photoelectron-diffraction using a single scattering cluster (SSC) arrangement (see Fadley(1984) and references therein). Radiation incident on an atom in the cluster ejects a core-level photoelectron. If  $\phi_0(\underline{r}, \underline{r}_j \rightarrow \underline{k})$  is the wave resulting from an atom at  $\underline{r}$ , in direction  $\underline{k}$  towards a scatterer  $j$  at  $\underline{r}_j$ , then subsequent scattering will give an overall wave amplitude of:-

$$\psi(\underline{r}, \underline{k}) = \phi_0(\underline{r}, \underline{k}) + \sum_j \phi_j(\underline{r}, \underline{r}_j \rightarrow \underline{k}) \quad - (2.2)$$

with photoelectron intensity given by

$$I(\underline{k}) \propto |\psi(\underline{r}, \underline{k})|^2 \quad - (2.3)$$

As the detector is at  $\underline{r} = \infty$  along  $\underline{k}$ , the waves can be taken to having the spherical forms

$$\phi_0 \propto \exp(ikr)/r \quad - (2.4)$$

$$\phi_j \propto \exp(ik|\underline{r}-\underline{r}_j|)/|\underline{r}-\underline{r}_j| \quad - (2.5)$$

Then if  $\theta_j$  is the scattering angle, the path length difference between  $\phi_0$  and  $\phi_j$  is:-

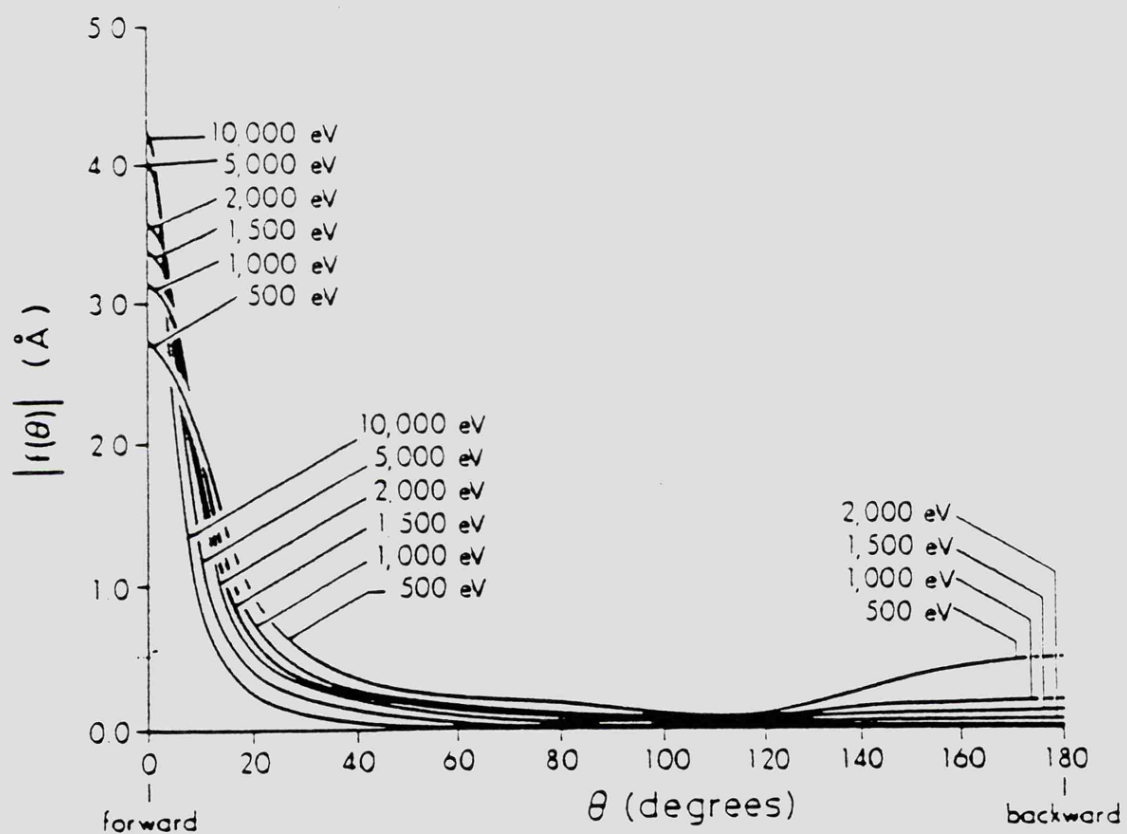


Figure (2.5) Angular dependence of scattering factor  $f(\theta)$  for Cu in energy range 500-10000eV, from Fadley (1984).

$$r_j(1-\cos\theta_j) \quad - (2.6)$$

Neglecting thermal vibration effects, the wave amplitude  $\phi_j$  after scattering at site  $j$  is given by:-

$$\phi_j \propto f_j(\theta_j)\exp(ik|\underline{r}-\underline{r}_j|)/|\underline{r}-\underline{r}_j| \quad - (2.7)$$

where  $f_j(\theta_j)$  is the complex atomic scattering factor

$$f_j(\theta_j) = |f_j(\theta_j)|[\exp(i\alpha_j(\theta_j))] \quad - (2.8)$$

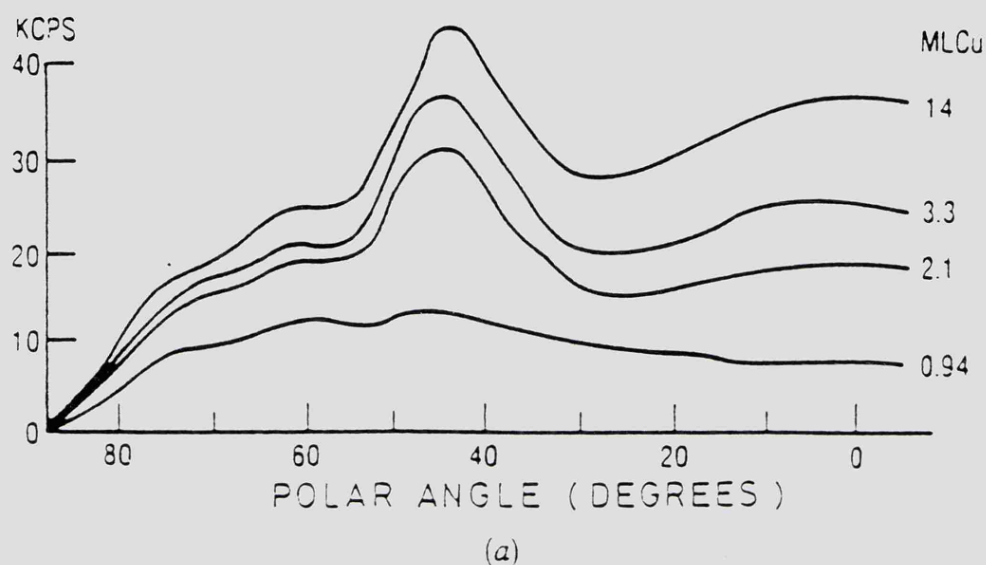
and  $\alpha_j(\theta_j)$  is the phase shift associated with the scattering. The overall phase shift of  $\phi_j$  relative to  $\phi_0$  is given by

$$kr_j(1-\cos\theta_j) + \alpha_j(\theta_j) \quad - (2.9)$$

due to both path length difference and scattering. Figure (2.5) shows the angular dependence of  $f(\theta)$  for Cu in the energy range 500 - 10000eV (from Fadley(1984)and see also Thomson and Fadley (1985)). It can be seen that the backscattered amplitude is ~18% of the forward scattered amplitude at 500eV, whereas this falls to ~6% at 1000eV and less than 1% at 2000eV.

### 2.3.2 STRUCTURE DETERMINATION

Egelhoff (1984) has given a very elegant demonstration of the predominance of forward scattering of electrons at high kinetic energies (>300eV). Figure (2.6a) shows electron intensity versus polar angle (polar angle and azimuthal angle are defined in figure (2.7)) of the  $\text{Cu}2p_{3/2}$  photoelectron emission for different thicknesses of epitaxial Cu on Ni(001), in the Ni[100] surface azimuth. The lattice mismatch of bulk fcc Cu and Ni is 2.5%, Cu having previously been shown to grow in a layer by layer fashion on Ni(001) (Chambers and Jackson, 1975). Figure (2.6b)



ANGLES FOR ENHANCED FORWARD SCATTERING

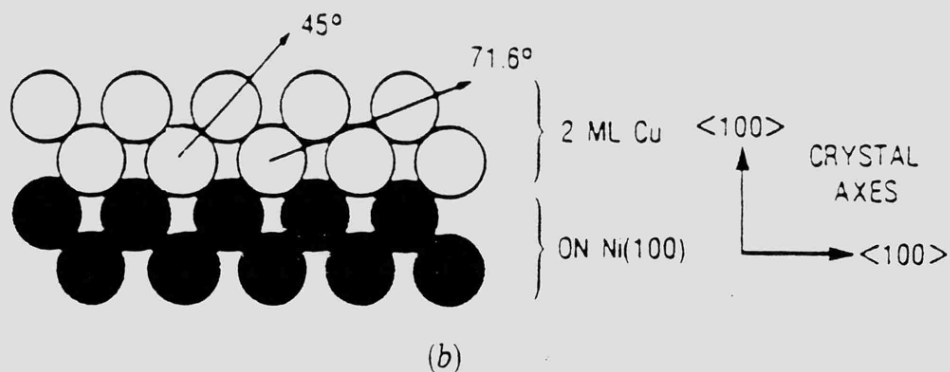


Figure (2.6) (a) Intensity versus polar angle of Cu 2p photoelectron emission as a function of Cu thickness in ML, kinetic energy = 317eV. (b) Angles at which forward scattering by overlying Cu layers causes enhance Cu intensities, from Egelhoff (1984).

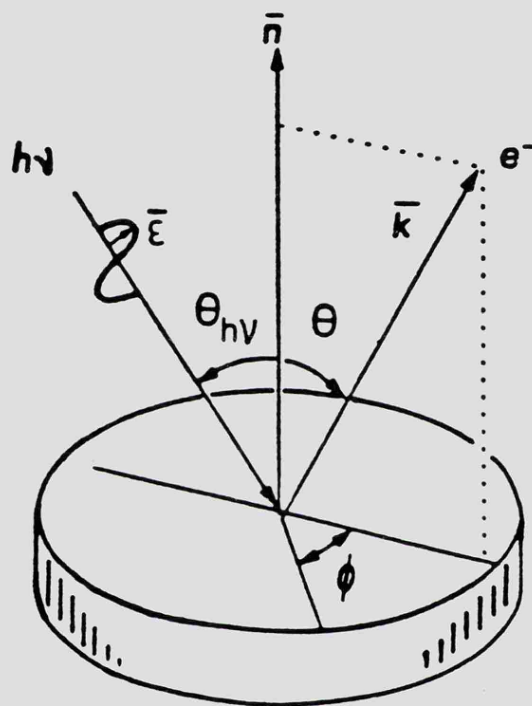


Figure (2.7) Typical experimental arrangement for photoemission defining azimuthal angle  $\phi$  and polar angle  $\theta$ .

illustrates the polar angles at which forward scattering of photoelectrons emitted from the lower layer of a 2 monolayer (ML) Cu layer on Ni(001) by the top layer causes enhanced Cu  $2p_{3/2}$  intensities in the polar scan.

As can be seen in the figure, the polar intensity curve for 0.94ML of Cu is basically featureless reflecting the response function of the electron detector, but between 1 and 2 ML a peak appears at  $\theta=45^\circ$ . This can be explained in terms of forward scattering of the Cu  $2p_{3/2}$  electrons along the bulk [101] fcc crystallographic axis (see figure (2.6b)).

Egelhoff found that by using electron kinetic energies far in excess of the 317eV used in figure (2.6a), far more detail could be observed in the polar intensity plots due to the increased influence of forward scattering at these higher energies. Moreover, as the forward scattering effects are only reliant on the kinetic energy of the measured electrons, Auger electrons also show the same angular dependence as photoelectrons. This is an advantage in that Auger energies do not change with changing photon energy, and higher count rates can be achieved by excitation of Auger electrons by electron beams.

The solid line in figure (2.8) shows polar angle intensity plots of the Cu LMM (917eV) Auger line for various coverages of Cu on Ni(001). For 1 ML of Cu the plot is featureless as before, but for a coverage of 2ML and above strong intensity peaks appear at  $\theta=45^\circ$  and  $90^\circ$ , corresponding to forward scattering of the Cu LMM electrons along the [101] and [001] axes of the fcc Cu lattice. The dashed line in the figure is from a calculation by Bullock and Fadley (1985) using the single scattering cluster model. In this work Bullock and Fadley have concluded that the peaks at  $45^\circ$  and  $90^\circ$  (peaks c and e in figure (2.8)) are totally due to forward scattering effects, as explained by Egelhoff, whilst other

EPITAXIAL Cu on Ni (001)

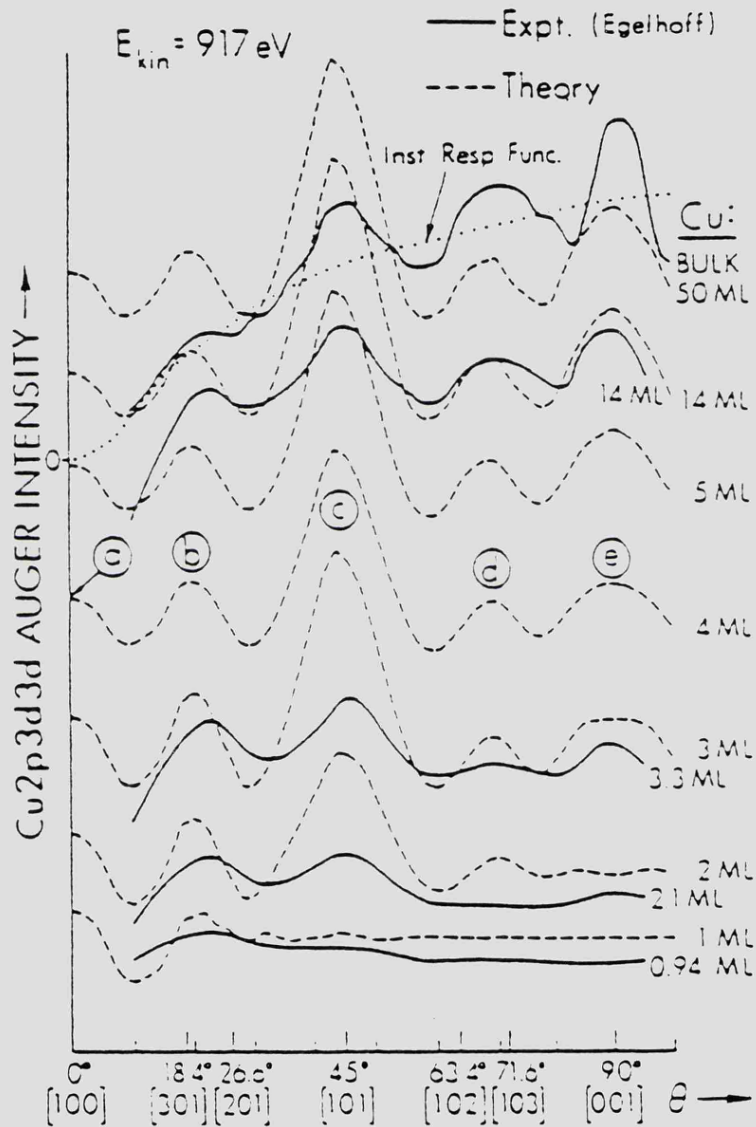


Figure (2.8) Calculated and experimental polar angle electron intensity curves for Cu/Ni(001), from Bullock and Fadley (1985).

features (peaks a,b and d) also have contributions due to first order diffraction from other scattering sites and cannot be interpreted solely as being due to forward scattering. This is in agreement with earlier work by Poon and Tong (1984) who have also studied Cu on Ni(001) using a single scattering approach. They have concluded that forward scattering is dominant only for scattering by nearest-neighbour and next-nearest-neighbour atoms at kinetic energies above ~300eV.

Therefore, by monitoring electrons with energies above 300eV, and by only considering scattering by nearest and next-nearest atoms, during epitaxial growth in the 0-5ML range it is possible to gather useful information both on overlayer structure and growth mode. This has been illustrated more recently by Chambers et al (1986), who have measured the outward vertical relaxation of Cu overlayers on Ni(001) by measuring relative shifts in position of peaks in polar intensity plots. Wesner et al (1986) have used electron forward scattering to measure the orientation of CO molecules adsorbed on K covered Pt(111).

### 2.3.3 CHOICE OF SUITABLE ELECTRON SERIES

As has been described in the previous section, both photoelectrons and Auger electrons exhibit forward scattering at high kinetic energies, and so can be used in the determination of structure and overlayer growth. However, apart from a high kinetic energy, other factors must be considered when deciding which electrons are to be monitored. Firstly the electron series must be intense; either photoelectrons with a high cross-section at the desired photon energy, or similarly intense Auger lines must be used. Secondly, when monitoring an overlayer, care must be taken to ensure that the overlayer electron series being measured is well separated from any Auger or photoelectron lines due to the substrate. Any overlap between substrate and overlayer electron series can lead to a

large contribution in the polar angle intensity distribution plot due to the substrate rather than the overlayer.

#### 2.4 THE STUDY OF MAGNETIC LAYERS USING POLARISED NEUTRON REFLECTION(PNR)

There is currently much interest in magnetic properties of surfaces and ultra-thin metallic layers due to the dramatic changes in magnetic behaviour predicted for such structures (see for example, 'Magnetic Properties of Low Dimensional Systems' edited by Falicov and Morán-López (1986) and references therein). This behaviour is thought to be influenced by electronic environment, reduced dimensionality, strain introduced into epitaxial layers and by changes in the coordination number.

The use of polarised neutrons to study surface magnetism was first proposed by Felcher (1981). As the neutron scattering amplitude per atom is of the order  $\sim 10^{-12}$ cm (i.e.  $\sim$ a nuclear radius), neutrons penetrate deeply into matter. Surface sensitivity can be greatly enhanced by using a highly collimated beam of long wavelength neutrons ( $\lambda \approx 5-15\text{\AA}$ ) at grazing incidence, close to the condition for total external reflection.

##### 2.4.1. NEUTRON REFRACTIVE INDEX FOR A FERROMAGNET

The important parameter which describes neutron behaviour close to the critical angle is the refractive index  $n$ . As the neutron passes from one medium (1) to another (2), the refractive index is given by:-

$$n_{1,2} = k_1/k_2 \quad - (2.10)$$

$k_j$  being the wave vector in the appropriate medium. If the neutron kinetic energy is given by  $E_1$  in medium (1), and it experiences a mean change in potential  $\langle V \rangle$  when it enters medium (2), then

$$n_{1,2} = [(E_1 - \langle V \rangle) / E_1]^{1/2} \quad - (2.11)$$

Since  $\langle V \rangle \ll E_1$ , ( $n$  is generally  $< 1.0$  and  $|1-n| \sim 10^{-6}$ )

$$n_{1,2} \approx 1 - \langle V \rangle / 2E_1 \quad - (2.12)$$

Taking medium (1) to be a vacuum,  $E_1$  can be written in terms of a de Broglie wavelength  $\lambda$ ,

$$E_1 = h^2 / (2m\lambda^2) \quad - (2.13)$$

For a ferromagnet, there is both a nuclear and magnetic contribution to the refractive index (see Hughes (1954) and Williams (1988)).

$$n = n_N + n_M \quad - (2.14)$$

Thus, if medium (2) is a ferromagnet,  $\langle V \rangle$  has both a nuclear and magnetic part. The nuclear part of  $\langle V \rangle$  is given by an averaged potential derived from the Fermi pseudopotential (see Williams (1988)):-

$$\langle V \rangle_N = h^2 N b / 2m \quad - (2.15)$$

Where  $b$  is the nuclear coherent scattering amplitude for medium (2),  $N$  is the number density of the scattering nuclei, and  $m$  is the neutron mass.

The magnetic part of the potential  $\langle V \rangle$  is given by:-

$$\langle V \rangle_M = -\underline{\mu}_n \cdot \underline{B} = \pm |\mu_n B| \quad - (2.16)$$

Where  $\underline{\mu}_n$  is the neutron magnetic moment vector, and  $\pm$  refers to the

neutron spins being parallel (+) or anti-parallel (-) to the applied magnetic field  $\underline{B}$  ( $\underline{B}$  is assumed to be applied in the plane of the surface of medium (2)). By taking both nuclear and magnetic parts for the potential  $\langle V \rangle$ , and substituting into equation (2.9), one can arrive at:-

$$n_{1,2}^{\pm} = 1 - \lambda^2 [(Nb/2\pi) \pm (m\mu_n B/\lambda^2)] \quad - (2.17)$$

or, assuming  $B = \mu_0 M$  where  $M$  is the layer magnetisation,

$$n_{1,2}^{\pm} = 1 - (\lambda^2 N/2\pi)(b \pm C\mu(z)) \quad - (2.18)$$

Where  $C = \text{a constant} = 0.2695 \times 10^{-12} \text{ cm}/\mu_B$ .

$\mu(z)$  is the magnetic moment per atom of the ferromagnet ( $z$  is the direction normal to the surface).

#### 2.4.2 NEUTRON REFLECTIVITY

Born and Wolf (1975) have discussed the propagation of a plane wave in a medium with refractive index  $n(z)$ , and have shown that the exact reflectivity cannot be given in closed form for an arbitrary  $n(z)$ . Felcher used the well known expression for the reflectivity from a semi-infinite slab of material with constant refractive index  $n$  (see Goldberger and Seitz(1947)):-

$$R_{\pm} = \left| \frac{\sin\theta - (n_{\pm}^2 - \cos^2\theta)^{1/2}}{\sin\theta + (n_{\pm}^2 - \cos^2\theta)^{1/2}} \right|^2 \quad - (2.19)$$

to calculate the reflectivity from Ni(001), where  $\theta$  is the glancing incident angle and  $n_{\pm}$  is given by equation (2.18) with a constant magnetic moment of  $0.6\mu_B/\text{atom}$ .  $R^+$  is the reflectivity for neutrons polarised parallel, and  $R^-$  the reflectivity for neutrons polarised anti-parallel to the applied magnetic field.

The ratio  $R^+/R^-$  is known as the flipping ratio  $F(R)$ , and can provide important information about the magnetic properties of the reflecting medium. Moreover,  $F(R)$  is independent of many experimental variables. Figure (2.9) is the result obtained by Felcher for  $F(R)$  for Ni(001) using equation (2.18). The plot shows  $F(R)$  versus glancing incidence angle  $\theta$  with  $\theta_c$  denoting the critical angle given by:-

$$\theta_c = \cos^{-1}(n_{\pm}) \quad - (2.20)$$

It can be seen that there are two critical angles, one for each neutron polarisation state. Below  $\theta_c(-)$  (the critical angle for anti-parallel polarisation) the reflectivity for both spin states is unity corresponding to total external reflection. Between  $\theta_c(-)$  and  $\theta_c(+)$   $F(R)$  rises rapidly as only neutrons polarised positively are totally reflected. Above  $\theta_c(+)$ ,  $F(R)$  decreases to an asymptotic value.

In order to use neutron reflectivity to study Ni(001) with a  $z$  dependent magnetisation, Felcher used a step function as a magnetic perturbation at the surface with a constant decrement in magnetic moment per atom over a given thickness of material. In this way he was able to show that the effect of the reduced magnetisation at the surface is to decrease  $F(R)$  above  $\theta_c(+)$  such that  $F(R)$  decreases more sharply than for the constant magnetisation case shown in figure (2.9) and that this variation in  $F(R)$  is experimentally measureable.

To study the magnetic properties of ultra-thin ferromagnetic layers, the neutron reflectivity can be calculated by taking into account the phase of the neutron wave at each interface (see Felcher et al (1985)). By assigning a refractive index  $n_j$  and thickness  $t_j$  to each successive layer, the reflectivity from a three medium system of (1)

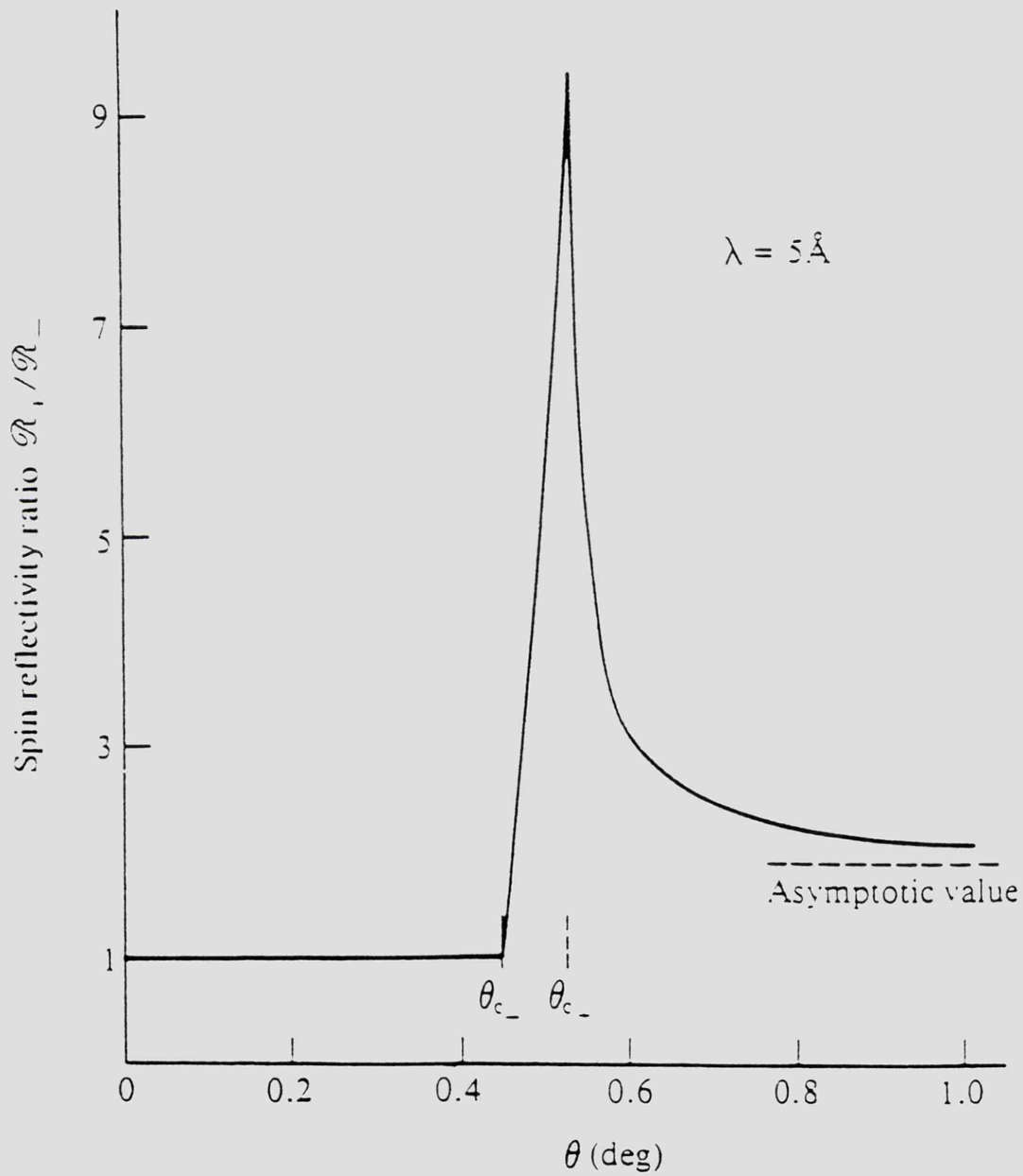


Figure (2.9) Spin reflectivity (Flipping) ratio for reflection from ferromagnetic Ni with uniform magnetic field of  $0.6\mu_B/\text{atom}$ , after Felcher (1981).

vacuum, (2) magnetic overlayer and (3) non-magnetic substrate is given by:-

$$R^{\pm}(q) = \left| \frac{r_{12}^{\pm} + r_{23}^{\pm} \exp(2iq_2^{\pm} t_2)}{1 + r_{12}^{\pm} + r_{23}^{\pm} \exp(2iq_2^{\pm} t_2)} \right|^2 \quad - (2.21)$$

$$\text{where } r_{ij} = \frac{p_i - p_j}{p_i + p_j} \quad \text{and } p_j = n_j \cos \theta_j$$

and  $q^{\pm}$  is the perpendicular component of the neutron wavevector given by:-

$$q^{\pm} = k_1 (n_1^{\pm 2} - \cos^2 \theta_i)^{1/2} \quad - (2.22)$$

for the lth medium where  $k=(2\pi/\lambda)$  is the incident wavevector in vacuum and  $\theta_i$  is the incident glancing angle.

The above expressions can easily be extended to the four medium structure shown in figure (2.10), comprising (1) vacuum/ (2) non-magnetic overlayer/ (3) magnetic thin film/ (4) non-magnetic substrate, to give:-

$$R^{\pm}(q) = \left| \frac{r_{12}^{\pm} + r_{234}^{\pm} \exp(2iq_2^{\pm} t_2)}{1 + r_{12}^{\pm} + r_{234}^{\pm} \exp(2iq_2^{\pm} t_2)} \right|^2 \quad - (2.23a)$$

where

$$r_{234}^{\pm} = \left| \frac{r_{23}^{\pm} + r_{34}^{\pm} \exp(2iq_3^{\pm} t_3)}{1 + r_{23}^{\pm} + r_{34}^{\pm} \exp(2iq_3^{\pm} t_3)} \right| \quad - (2.23b)$$

Bland et al (1987) have used the above expressions to calculate  $F(R)$  for Co epitaxially deposited onto Cu(001). Curve A in figure (2.11) shows the calculated flipping ratio  $F(R)$  for 18Å of Co with magnetic moment of  $1.7\mu_B$  per atom, deposited on Cu(001). As can be seen from the

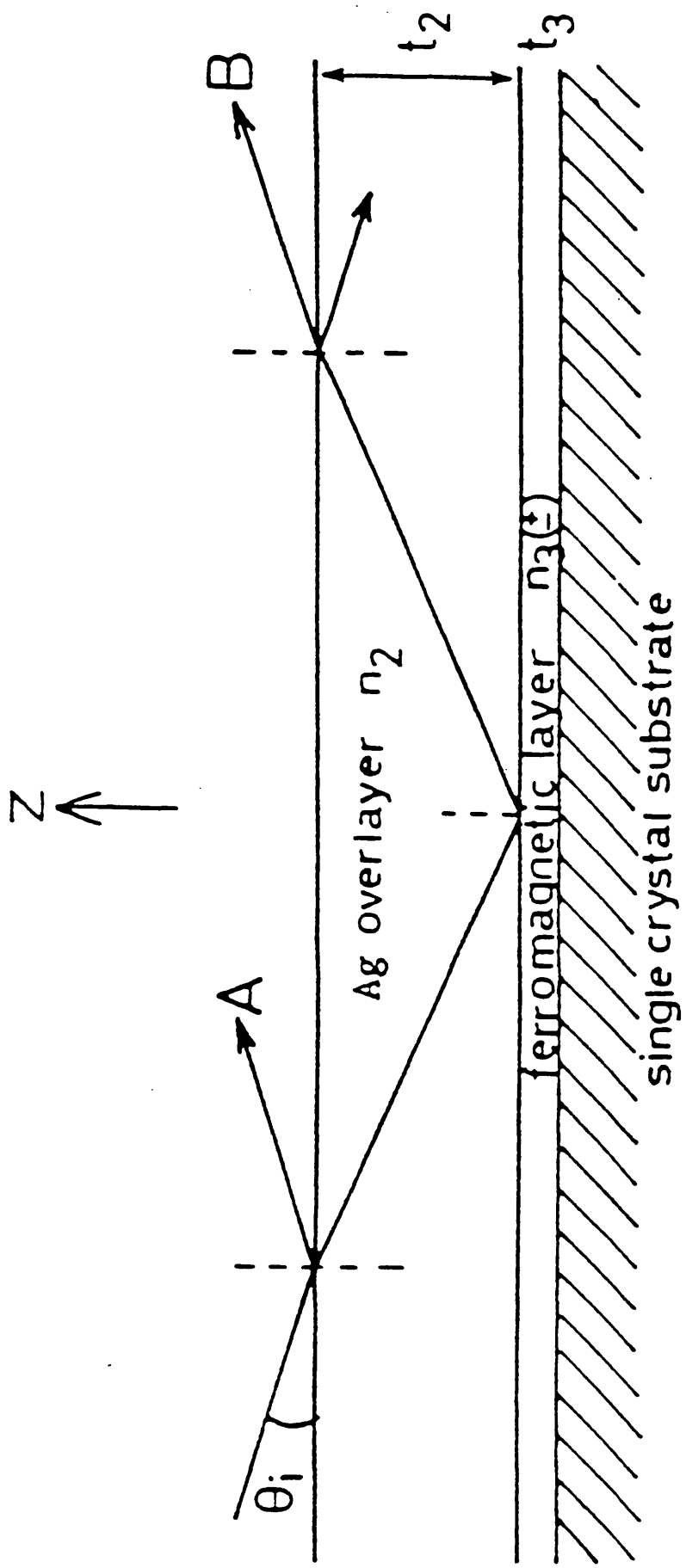


Figure (2.10) Sandwich structure whose reflectivity is described by equation (2.23), comprising (1) vacuum/ (2) non-magnetic overlayer/ (3) ferromagnetic thin film/ (4) non-magnetic substrate.

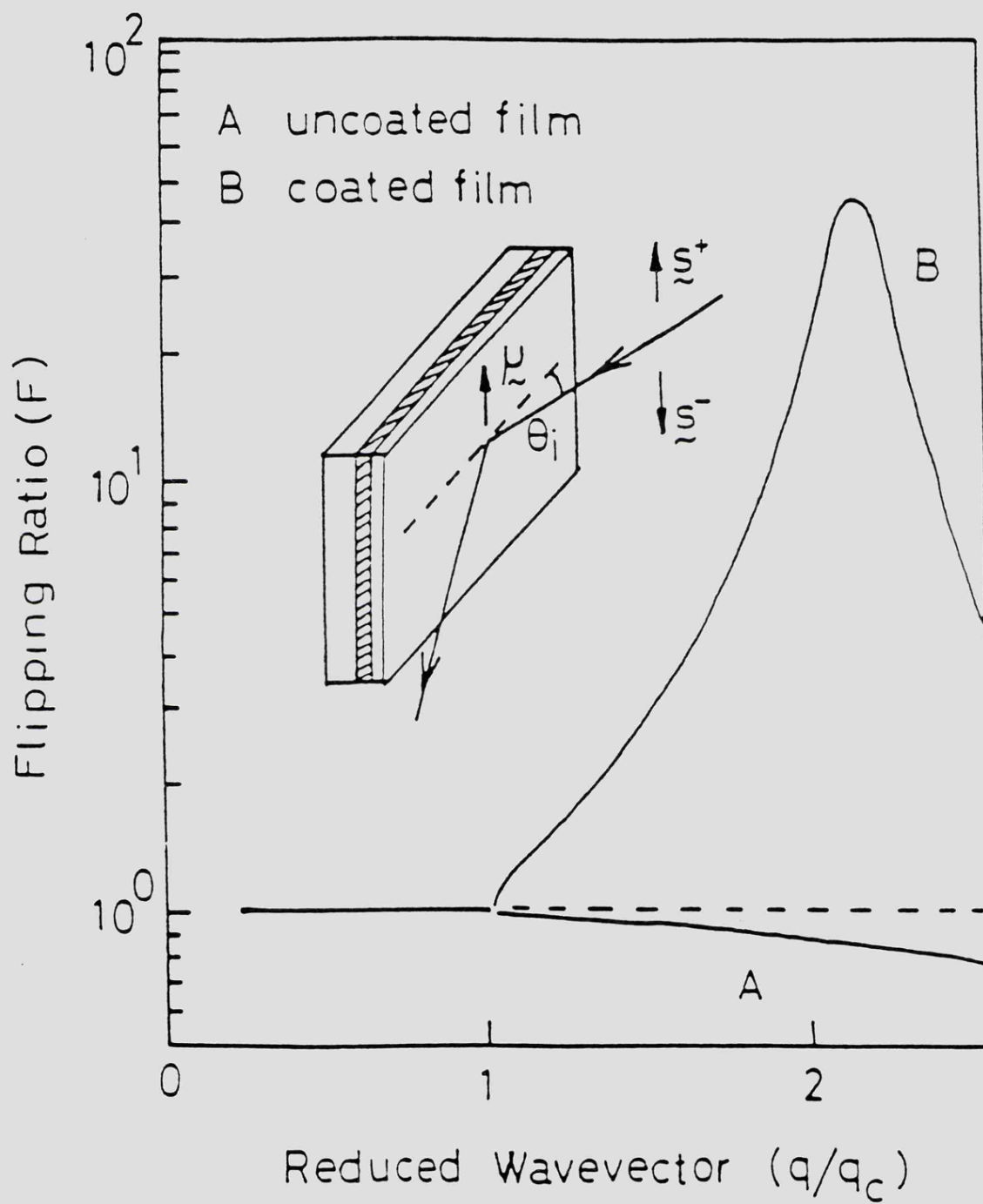


Figure (2.11) Calculated flipping ratios Co/Cu(001) showing enhanced signal B due to non-magnetic overlayer, from Bland et al (1987).

figure, there is very little deviation from unity with  $\Delta F \approx 0.12$  at  $2q_c$ . However, by calculating  $F(R)$  for the same Co/Cu(001) system with 42Å of Cu(001) adsorbed on top of the Co layer, Bland et al obtained curve B in figure (2.11). As can be seen a resonance peak in  $F(R)$  of the order  $\Delta F \approx 50$  has appeared at  $q = 2q_c$ . This peak is due to constructive interference between neutron waves A and B in figure (2.10).

The position of the peak maximum in  $q$  is dependent on overlayer thickness  $t_2$ , the maximum moving to larger  $q$  with decreasing overlayer thickness  $t_2$ . The peak height is a measure of the product  $\mu t_3$ , where  $t_3$  is the thickness of the ferromagnetic layer (see figure (2.10)) and  $\mu$  is the magnetic moment per atom of the magnetic layer in  $\mu_B$ . By fitting to experimental data obtained from a 42ÅCu/18ÅCo/Cu(001) structure, Bland et al obtained a value of  $\mu = 1.8 \pm 0.25\mu_B$  per atom for the Co layer, in agreement with the calculation of Marcus and Moruzzi(1985) of  $1.7\mu_B$ .

Thus by judicious choice of layer thicknesses PNR can provide an accurate measurement of magnetic moment per atom of ferromagnetic surfaces and thin films of monolayer thickness. With a suitable sample holder it is also possible to measure temperature dependence of the moments of such structures.

## 2.5 THE STUDY OF SURFACES USING X-RAY DIFFRACTION

X-ray diffraction has been the most widely used technique in the study of the atomic structure of bulk solids during the past 70 years. Following the work of Eisenberger and Marra (1981) it has become increasingly used in the study of surfaces. The main advantages of X-ray diffraction over other techniques follows from the weak interaction of X-rays with solids, which for example allows the scattered intensity to be analysed with a single scattering (kinematical) theory.

The main reason why X-ray diffraction has been so little used to study surfaces is that the lack of sensitivity. The penetration depth of X-rays is of the order of  $\sim 10\mu\text{m}$ , and as the diffracted intensity goes as the number of scatterers squared it can be seen that the surface contribution is  $\sim 10^7$  less than that of the bulk. It has been shown that by using grazing incidence geometry, near the angle for total external reflection, one can preferentially illuminate the surface region (see Marra et al (1979)). Furthermore count rates can be increased by several orders of magnitude by using the intense radiation produced by a synchrotron source, the increasing availability of such sources contributing to the rise in the number of surface X-ray diffraction experiments. For a good review of bulk X-ray diffraction see Warren (1969), and for surface X-ray diffraction see Robinson in 'Handbook of Synchrotron Radiation' and Vlieg (1988).

### 2.5.1 CRITICAL ANGLE AND REFRACTIVE INDEX

Ignoring absorption, the refractive index for X-rays at a vacuum-solid interface can be approximately given by the Drude theory (see for example, Ashcroft and Mermin, 1976):-

$$n = 1 - \delta \quad - (2.24)$$

$$\text{or} \quad n = 1 - \frac{e^2}{2\pi mc^2} \frac{N_A \sum_i Z_i}{\sum_i A_i} \rho \lambda^2 \quad - (2.25)$$

Where  $N$  = Avogadro's number

$e$  = electron charge

$m$  = electron mass

$c$  = velocity of light

$z_i$  = atomic number of atom  $i$  in the unit cell

$A_i$  = atomic mass of atom  $i$  in unit cell in atomic units

$\rho$  = mass density in  $\text{g/cm}^3$

$\lambda$  = wavelength in  $\text{\AA}$

and summations are over the unit cell. The critical angle  $\theta_c$  is then defined as:-

$$\cos\theta_c = n \quad - (2.26)$$

and since  $1-n$  is typically  $\sim 10^{-6}$ , this can be approximated to:-

$$\theta_c = (2\delta)^{\frac{1}{2}} \quad - (2.27)$$

For Ge, using radiation of wavelength  $1.13\text{\AA}$ ,  $\theta_c = 0.243^\circ$ .

### 2.5.2 BASIC DIFFRACTION THEORY

The electric field amplitude diffracted by a single atom situated at  $\underline{r}$ , at a distance  $R$  from the scattering site is given using the Born approximation (see Warren, 1969):-

$$E = E_0 \frac{e^2}{mc^2 R} \int e^{-i\underline{Q} \cdot (\underline{r} + \underline{r}')} \rho(\underline{r}') d^3 \underline{r}' \quad - (2.28)$$

Where  $E_0$  is the incident electric field amplitude,  $e$  is the electron charge and  $m$  is the electron mass. The momentum transfer  $\underline{Q}$  is defined as  $\underline{Q} = \underline{k}_f - \underline{k}_i$  (see figure (2.12)), and  $\rho(\underline{r}')$  is the electron density about

$\underline{r}$ . The atomic form factor is defined as the Fourier transform of the electron density such that:-

$$f(\underline{Q}) = \int e^{-i\underline{Q}\cdot\underline{r}'} \rho(\underline{r}') d^3\underline{r}' \quad - (2.29)$$

and

$$E = E_0 \frac{e^2}{mc^2 R} f(\underline{Q}) e^{-i\underline{Q}\cdot\underline{r}} \quad - (2.30)$$

Writing  $\underline{r} = xa_1 + ya_2 + za_3$ , where  $a_1$ ,  $a_2$  and  $a_3$  define the unit cell, and summing over all atoms  $j$  in a unit cell, the structure factor for a reflection denoted by  $hkl$  is defined as:-

$$F(\underline{Q}) = \sum_j f_j(\underline{Q}) \exp(-2\pi i(hx_j + ky_j + lz_j)) \quad - (2.31)$$

The above expression only describes atoms that have fixed positions represented by the vectors  $\underline{r}_j$ . In general atoms vibrate about their equilibrium position due to thermal effects, causing the diffracted intensity to decrease at increasing temperature. The diffracted intensity that has been lost appears as thermal diffuse scattering in the form of a background intensity. A more general description of the structure factor would be:-

$$F(\underline{Q}) = \sum_j f_j(\underline{Q}) \exp(-M_j) \exp(-2\pi i(hx_j + ky_j + lz_j)) \quad - (2.32)$$

Where  $M$  is the Debye-Waller factor and is related to the mean-square thermal vibrational amplitude by:-

$$M = \frac{1}{2} Q^2 \langle u^2 \rangle \quad - (2.33)$$

Where  $\underline{Q}$  is defined in figure (2.12) and is given by  $\underline{Q} = 2\underline{k} \sin\beta$ , where  $|\underline{k}| = 2\pi/\lambda$ .

The diffracted electric field amplitude can thus be written as:-

$$E = E_0 \frac{e^2}{mc^2 R} F(\underline{Q}) \quad - (2.34)$$

The diffracted intensity is given by  $EE^*c/(8\pi)$ , and so for a crystal of lattice parameters  $a_1, a_2, a_3$  and  $N_1, N_2, N_3$  unit cells defined by primitive vectors  $\underline{a}_1, \underline{a}_2, \underline{a}_3$  and reciprocal lattice vectors  $\underline{b}_1, \underline{b}_2, \underline{b}_3$ , the diffracted intensity is given by:-

$$I = I_0 \frac{e^4}{m^2 c^4 R^2} |F(\underline{Q})|^2 \left| \sum_{j_1=1}^{N_1} \sum_{j_2=1}^{N_2} \sum_{j_3=1}^{N_3} e^{-i(q_1 a_1 j_1 + q_2 a_2 j_2 + q_3 a_3 j_3)} \right|^2 \quad (2.35)$$

where  $I_0 = E_0 E_0^* c/(8\pi)$ . By following the calculation of Warren(1969), this reduces to:-

$$I = I_0 \frac{e^4}{m^2 c^4 R^2} |F(\underline{Q})|^2 \frac{\sin^2(\frac{1}{2}N_1 q_1 a_1)}{\sin^2(\frac{1}{2}q_1 a_1)} \frac{\sin^2(\frac{1}{2}N_2 q_2 a_2)}{\sin^2(\frac{1}{2}q_2 a_2)} \frac{\sin^2(\frac{1}{2}N_3 q_3 a_3)}{\sin^2(\frac{1}{2}q_3 a_3)} \quad - (2.36)$$

The conditions for I to be a maximum are given by the three Laue conditions:-

$$q_1 a_1 = 2\pi h$$

$$q_2 a_2 = 2\pi k$$

$$q_3 a_3 = 2\pi l$$

with hkl integer, such that when these conditions are satisfied the intensity is sharply peaked at the Bragg points where the intensity is given by:-

$$I = I_0 \frac{e^4}{m^2 c^4 R^2} |F(\underline{g})|^2 N_1^2 N_2^2 N_3^2 \quad - (2.37)$$

which is proportional to the total number of scatterers squared.

### 2.5.3 SURFACE X-RAY DIFFRACTION

In surface X-ray diffraction the Laue condition in the z direction (perpendicular to the surface) is relaxed. The effect of the termination of the bulk lattice by the surface is to extend the Bragg points in the z direction. This is known as the creation of surface streaks (Andrews and Cowley, 1985) and more recently referred to as crystal truncation rods (Robinson, 1986). Although the in-plane Laue conditions still have to be satisfied, the value of l for the perpendicular Laue condition can take any value. There will still be bulk Bragg peaks when l=integer, but for other values of l an average value for  $\sin^2(\frac{1}{2}N_3q_3a_3)$  is taken such that the intensity is given by:-

$$I = I_o \frac{e^4}{m^2 c^4 R^2} |F(\underline{Q})|^2 N_1^2 N_2^2 \frac{1}{2\sin^2(\frac{1}{2}q_3 a_3)} \quad - (2.38)$$

$$\text{where } |F_{CTR}|^2 = \frac{1}{2\sin^2(\frac{1}{2}q_3 a_3)} \quad - (2.39)$$

and  $F_{CTR}$  is the crystal truncation rod. The scattered intensity will be the sum of the surface and bulk components, and this can provide information about the registry of the surface and the bulk (Feidenhans'1 (1986)). If there is a reconstruction on the surface denoted by  $n \times m$  there will be fractional order diffraction rods at positions  $(i/n, i/m)$  ( $i$ =integer) in the reciprocal lattice that are totally due to the surface with no bulk contribution and the inverse of the width of these rods gives information about the size of the reconstructed domain.

### 2.5.4 INTEGRATED INTENSITY

A useful quantity in a surface X-ray diffraction experiment is the

integrated intensity as it accounts for the fact that the sample is not a perfect crystal, the detector resolution function is not uniform and the beam is not from a perfectly monochromatic point source. The following integrated intensity obtained from a surface is based on the derivation of Warren (1969) for the integrated intensity of a bulk reflection. Assuming that the scan is made about an axis perpendicular to the scattering plane and the sample is rotated with an angular velocity  $\omega$  the total diffracted energy striking the detector is given by integrating the intensity  $I$  over time  $t$  and the detector area  $A$  such that:-

$$E = \iint Idt dA = \iiint Idt R^2 d\beta d\gamma \quad - (2.40)$$

where  $\beta$  and  $\gamma$  are the exit angles of the diffracted beam. If  $\alpha$  is the angle of rotation of the sample during the scan, then:-

$$dt = d\alpha/\omega \quad - (2.41)$$

and

$$E = \frac{R^2}{\omega} \iiint Id\alpha d\beta d\gamma \quad - (2.42)$$

Following the calculation of Warren, the above integral can be transformed into reciprocal lattice coordinates:-

$$E = \left[ \frac{\lambda}{2\pi} \right]^3 \frac{a_1 a_2}{A_u \sin 2\theta} \frac{R^2}{\omega} \int I dq_1 dq_2 dq_3 \quad - (2.43)$$

Where  $I$  is given by equation (2.36),  $\theta$  is the scattering angle and  $A_u$  is the surface unit cell area ( $a_1 a_2$ ). By substituting for  $I$  and integrating one arrives at the expression for integrated intensity:-

$$E = \frac{I_0}{\omega} \left[ \frac{e}{m c^4} \right] \frac{|F(Q)|^2 \lambda^3}{A_u \sin 2\theta} N \frac{\Delta Q_3}{2\pi} \quad - (2.44)$$

Where  $N=N_1 N_2$  the number of scatterers in the surface and  $\Delta Q_3$  is the length of the diffraction rod in reciprocal lattice units that is collected by the detector.

## CHAPTER 3

### EXPERIMENTAL DETAILS

#### 3.1 Introduction

#### 3.2 Angle-resolved XPS/AES

##### 3.2.1 UHV System

##### 3.2.2 Sample Manipulator

##### 3.2.3 LEED and Auger Electron Spectroscopy

##### 3.2.4 X-ray and UV Photon Sources

##### 3.2.5 Hemispherical Electron Analyser

##### 3.2.6 Data Acquisition System

##### 3.2.7 Sample Preparation

##### 3.2.8 Vapour Sources

#### 3.3 Polarised Neutron Reflection Measurements

##### 3.3.1 Experimental Arrangement

##### 3.3.2 Sample Preparation

#### 3.4 Surface X-ray Diffraction Measurements

##### 3.4.1 Synchrotron Radiation

##### 3.4.2 Beamline and X-ray Monochromator

##### 3.4.3 Surface X-ray Diffraction UHV Chamber

##### 3.4.4 5-Circle Diffractometer and Sample Alignment

##### 3.4.5 Data Acquisition

##### 3.4.6 Sample Preparation

## CHAPTER 3

### EXPERIMENTAL DETAILS

#### 3.1 INTRODUCTION

This chapter describes the experimental procedures used in this work. The study of clean surfaces necessitates an ultra-high vacuum (UHV) environment. This can easily be demonstrated by using the simple kinetic theory of gases. The rate of arrival of atoms at a surface from a gas can be given by:-

$$r = 3.51 \times 10^{22} P / (TM)^{1/2} \text{ cm}^{-2} \text{ s}^{-1}$$

where P = pressure in Torr

M = molecular weight

T = absolute temperature

Then, assuming 1 monolayer to be  $\sim 10^{15}$  atoms  $\text{cm}^{-2}$ , a single monolayer would be deposited in a time

$$t \sim 10^{-6} \text{ secs}$$

at 1 Torr for Nitrogen at 300K. This rises to  $\sim 4$  hours at  $10^{-10}$  Torr, the typical time required for an experiment. In this work, experiments were carried out at pressures of  $< 10^{-10}$  Torr, enabling measurements of several hours duration to be undertaken.

In order to study surface regions using X-rays and neutrons, highly intense collimated sources are required. In order to fully exploit these intense radiation sources, complex experimental configurations are

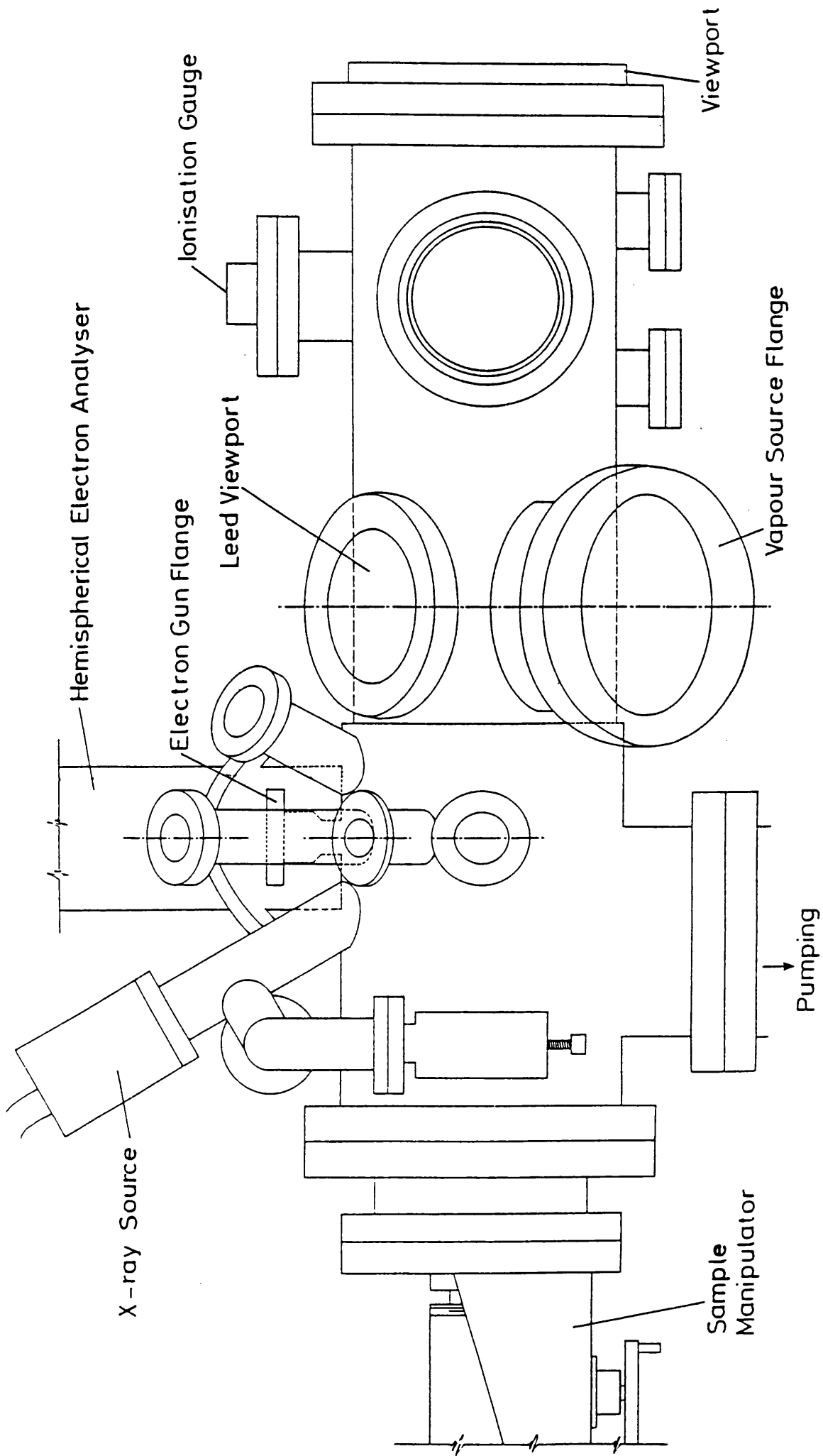
needed. These will be described in this chapter.

## 3.2 ANGLE RESOLVED XPS/AES

### 3.2.1 UHV SYSTEM

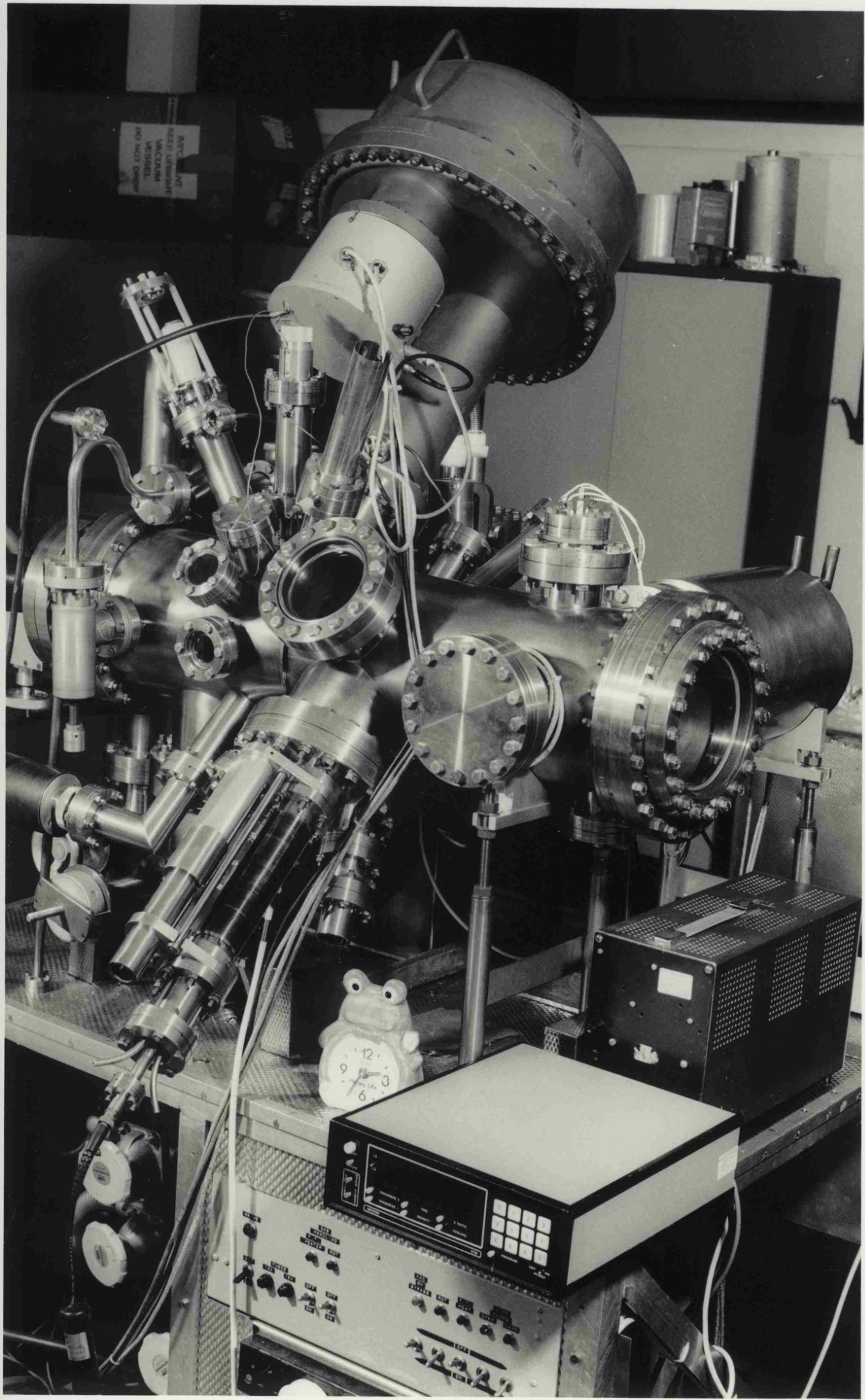
The angle resolved X-ray and Auger electron spectroscopies described in this thesis were carried out in a purpose built ultra-high vacuum (UHV) chamber, shown in figure (3.1) and plate (3.1). The system is based on the design used by Gardiner(1983) to study liquid metals, but has been extensively modified to include surface analysis techniques. Pumping is achieved by two liquid nitrogen trapped diffusion pumps, one 200 litres/sec and the other 32 litres/sec, both values referring to the pumping speed in the chamber. A liquid nitrogen cooled titanium sublimation pump (TSP) provides a further pumping speed of over 1000 litres/sec in the chamber. After baking the system at 200°C for ~15hrs a base pressure of  $2 \times 10^{-11}$  Torr is routinely achieved.

Sample deposition is carried out in the right hand side of the chamber, where a 3-grid LEED optics system, Vacuum Generators LEG31 electron gun, and knudsen cell vapour sources are mounted (see figure (3.2a)). The sample can then be transferred by means of the sample manipulator to the left hand side of the chamber where the UV light source, X-ray source, electron gun and hemispherical electron analyser are positioned (see figure (3.2b)). The inside of the chamber is lined with  $\mu$ -metal to reduce the effect of the earth's magnetic field. A quadrupole mass spectrometer is used for residual gas analysis and leak detection. Argon sputtering for sample cleaning is possible, high purity argon being introduced into the system through a leak valve.

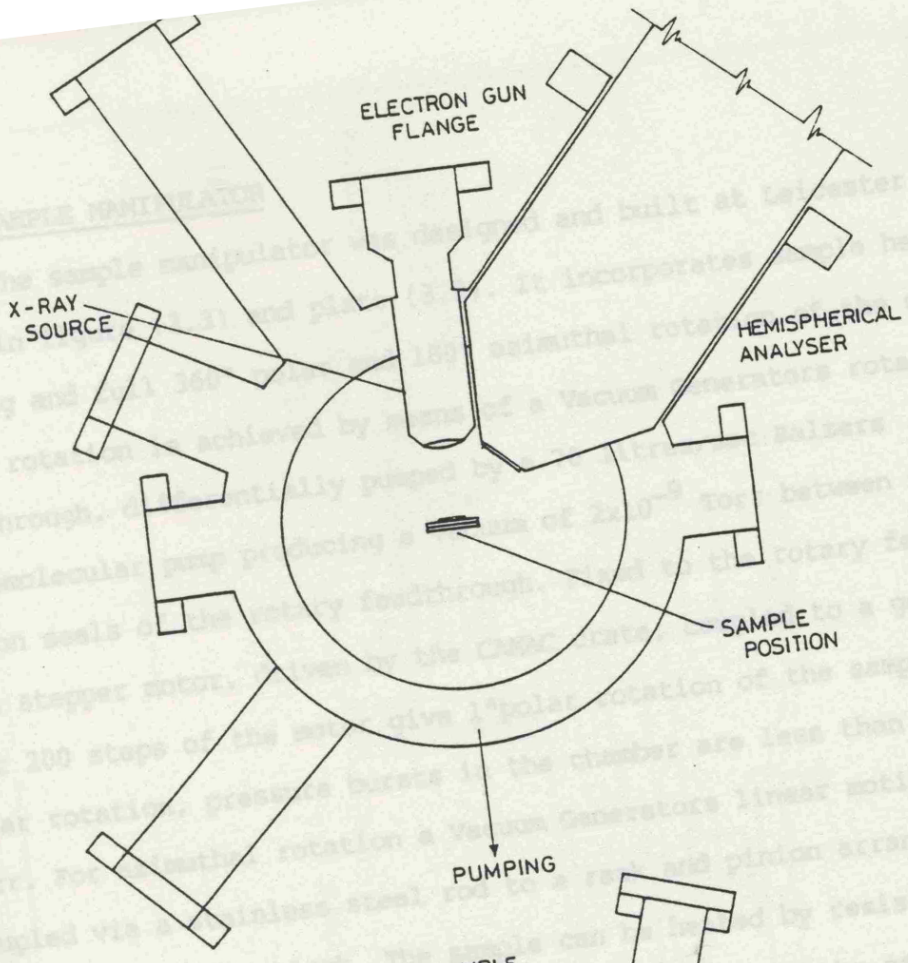


Figure(3.1) Schematic diagram of the Leicester UHV chamber.

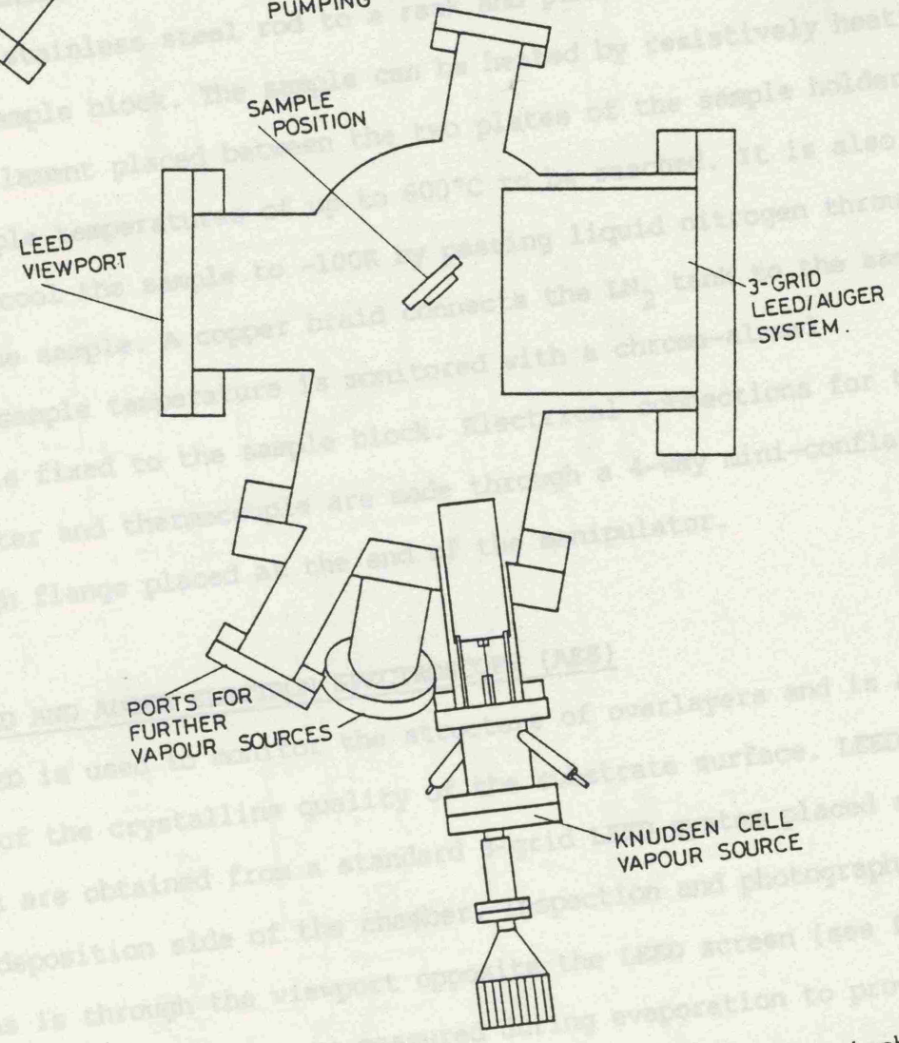
Plate(3.1) The Leicester UHV system.



a



b



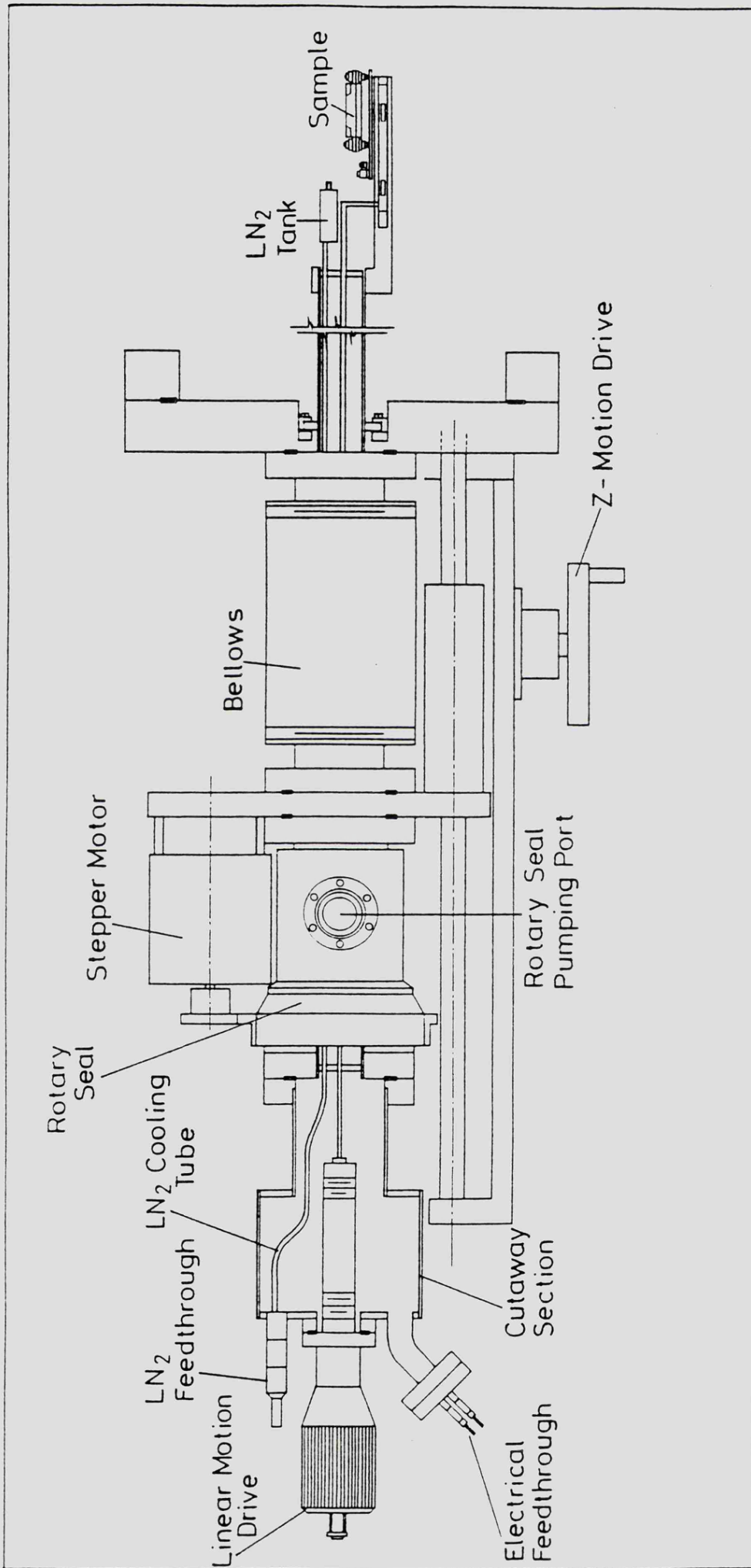
Figure(3.2) Section through UHV chamber at (a)-hemispherical analyser position and (b)-LEED position.

### 3.2.2 SAMPLE MANIPULATOR

The sample manipulator was designed and built at Leicester and is shown in figure (3.3) and plate (3.2). It incorporates sample heating and cooling and full 360° polar and 180° azimuthal rotation of the sample. Polar rotation is achieved by means of a Vacuum Generators rotary feedthrough, differentially pumped by a 70 litres/sec Balzers turbomolecular pump producing a vacuum of  $2 \times 10^{-9}$  Torr between the two teflon seals of the rotary feedthrough. Fixed to the rotary feedthrough is a stepper motor, driven by the CAMAC crate, coupled to a gearbox such that 200 steps of the motor give 1° polar rotation of the sample. During polar rotation, pressure bursts in the chamber are less than  $2 \times 10^{-11}$  Torr. For azimuthal rotation a Vacuum Generators linear motion drive is coupled via a stainless steel rod to a rack and pinion arrangement beneath the sample block. The sample can be heated by resistively heating a tungsten filament placed between the two plates of the sample holder, enabling sample temperatures of up to 600°C to be reached. It is also possible to cool the sample to ~100K by passing liquid nitrogen through a tank near the sample. A copper braid connects the LN<sub>2</sub> tank to the sample block. The sample temperature is monitored with a chrome-alumel thermocouple fixed to the sample block. Electrical connections for the sample heater and thermocouple are made through a 4-way mini-conflat feedthrough flange placed at the end of the manipulator.

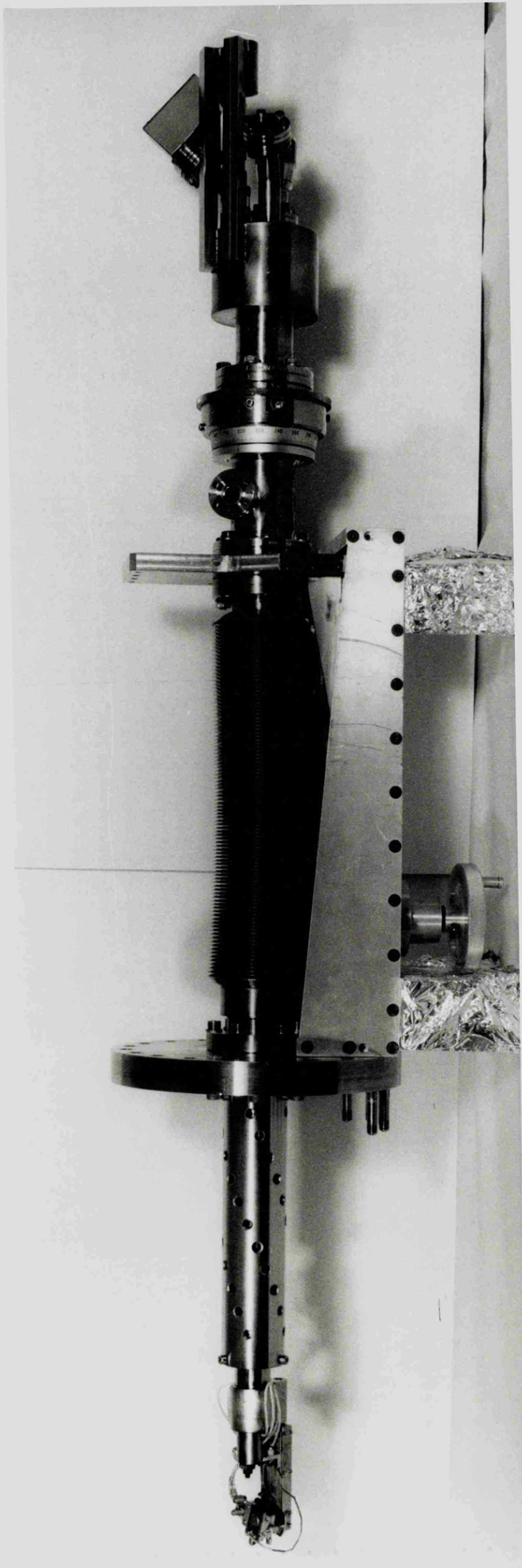
### 3.2.3 LEED AND AUGER ELECTRON SPECTROSCOPY (AES)

LEED is used to monitor the structure of overlayers and is a monitor of the crystalline quality of the substrate surface. LEED patterns are obtained from a standard 3-grid LEED system placed at the sample deposition side of the chamber. Inspection and photography of LEED patterns is through the viewport opposite the LEED screen (see figure (3.4)). Auger electrons were measured during evaporation to provide an



Figure(3.3) Sample manipulator.

Plate(3.2) The Leicester-built sample manipulator.



As-t plot, by using the 3-grid LEED optics as a retarding field analyser (RFA). By setting a negative ramp voltage that is somewhat less than the primary electron energy  $E_p$  on the retarding grids G2 and G3, then all electrons having an energy greater than this potential will reach the screen S, which is used as a current collector. Then, for a given ramp voltage  $V_0$  (corresponding to an energy  $E_0 = eV_0$ ), the current reaching the collector is given by:-

$$I(E) = \int_{E_0}^{\infty} N(E) dE = \int_{E_0}^{E_p} N(E) dE \quad - (3.1)$$

where  $N(E)$  is the energy distribution of the electrons leaving the sample. Thus it is apparent that by differentiating the current from the collector it is possible to obtain  $N(E)$ . The simplest way of doing this is to apply a small modulating voltage to the ramp voltage i.e.  $V_0 + \Delta V \sin \omega t$ . By expanding  $I(E_0)$  as a Taylor series it can be seen that the current is given by a DC term plus a sum of harmonics:-

$$I(E_0) = \int_{E_0}^{E_p} N(E) dE + A_1 \sin \omega t + A_2 \sin 2\omega t + \dots \quad -(3.2)$$

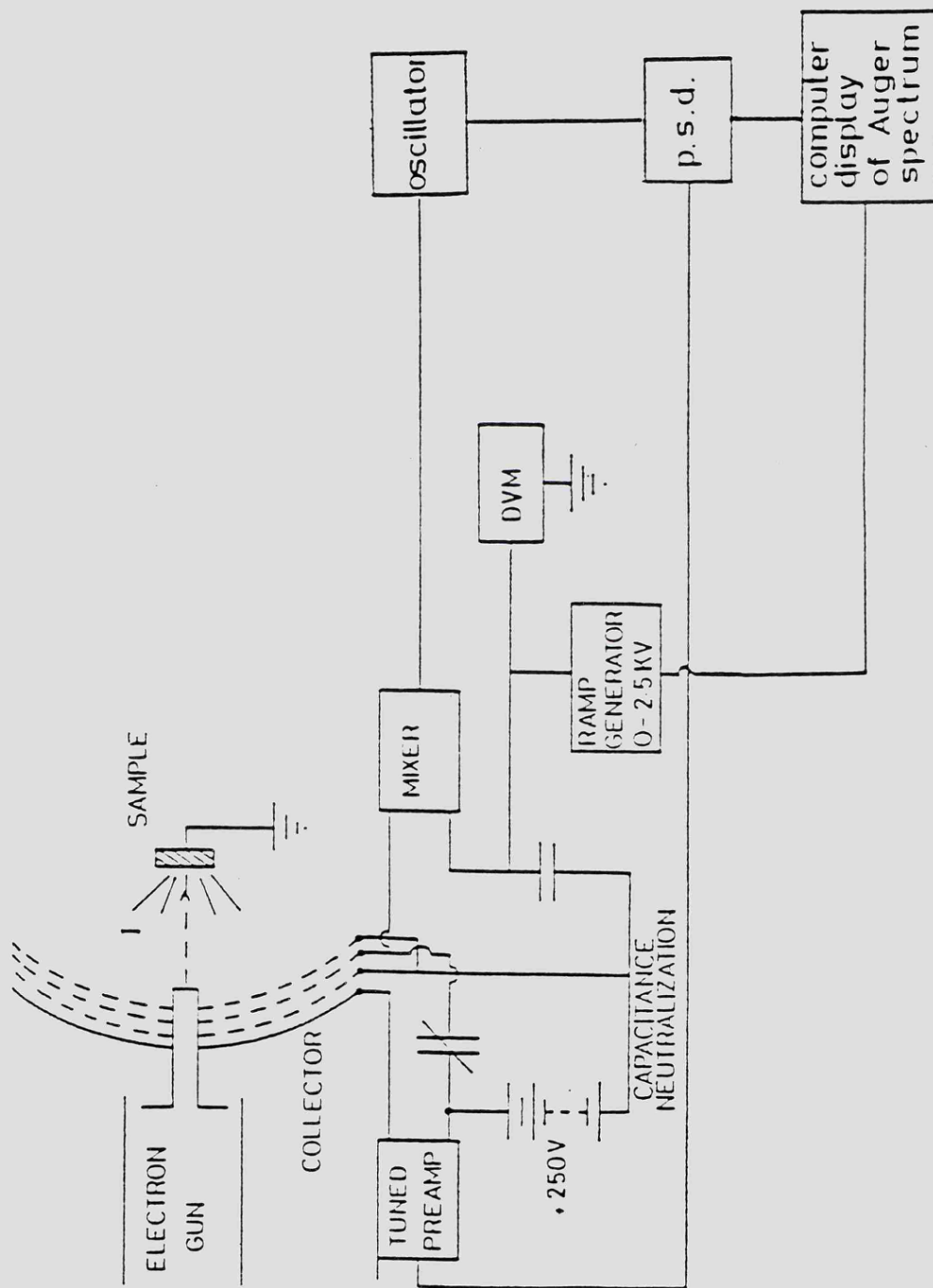
where

$$A_1 = \Delta E N(E_0) + \frac{\Delta E^3 N''(E_0)}{8} + \dots$$

$$A_2 = \frac{\Delta E^2 N'(E_0)}{4} + \frac{\Delta E N'''(E_0)}{48} + \dots$$

Thus by measuring the collector current with frequency  $\omega$  gives a current proportional to  $\Delta E N(E_0)$  to a first order, which provided  $\Delta E$  is small (~a few eV), is a good approximation.

Since the Auger features on  $N(E)$  are often weak peaks on a large



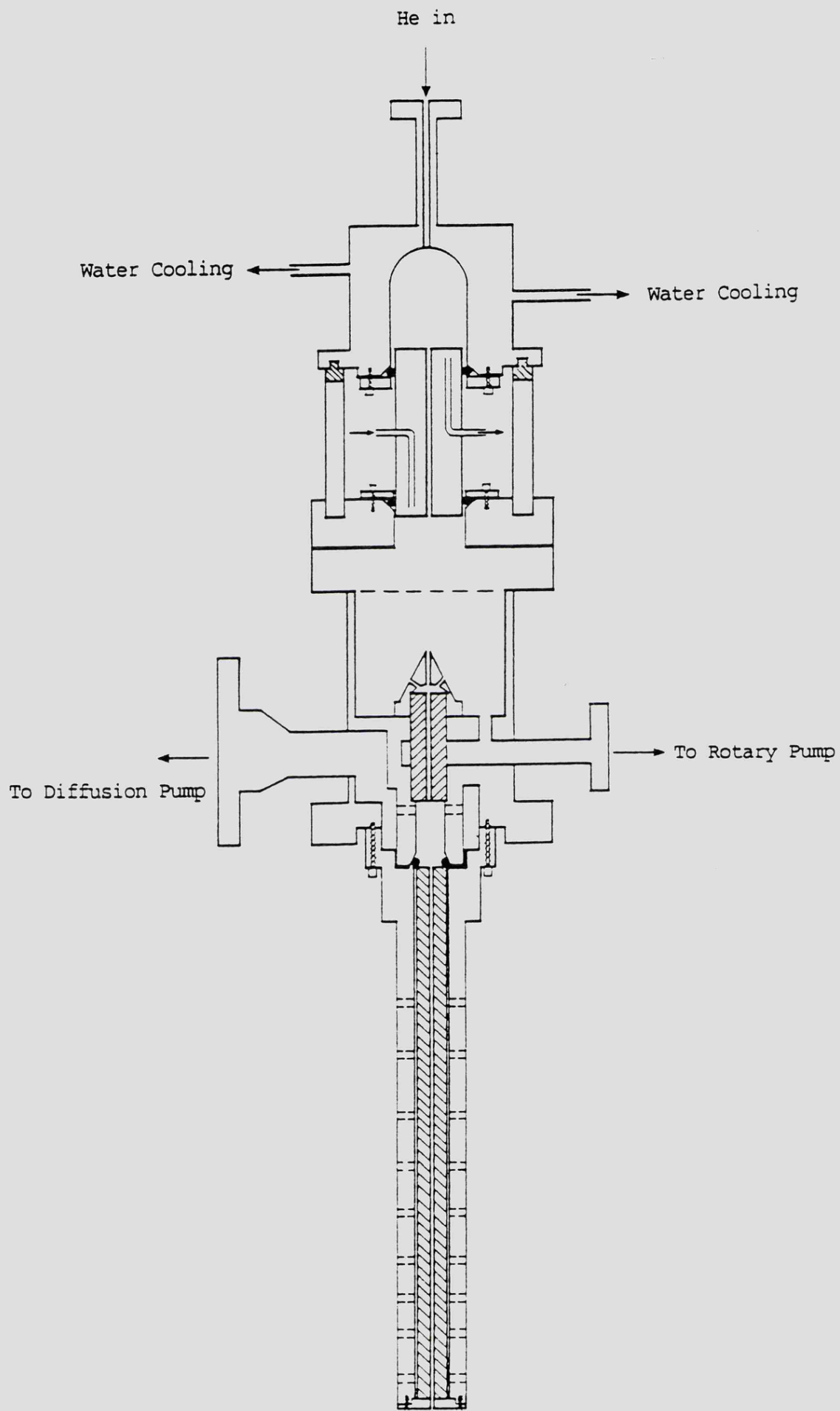
Figure(3.4) 3-Grid LEED/Auger system connected for AES.

background, it is usual to measure the amplitude of the second harmonic  $\sin 2\omega t$ . As can be seen from above this is proportional to the first derivative of  $N(E)$ , which removes the constant background and enhances the Auger peak. The experimental arrangement is shown in figure (3.4). The second harmonic is detected with a lock in amplifier tuned to twice the modulation frequency. The neutralising capacitance circuit is to compensate for any capacitive coupling between the retarding grids and the collector.

#### 3.2.4 X-RAY AND UV PHOTON SOURCES

The UHV chamber is equipped with both X-ray and UV light sources. The X-ray gun is a standard Vacuum Generators twin anode source with Al and Mg anodes. Al  $K_{\alpha}$  radiation (1486.6eV) is produced using 15KV anode potential and 40mA emission from the filament. The Mg  $K_{\alpha}$  radiation (1253.6eV) is produced using 15KV anode potential and 20mA emission current.

The He discharge light source is a modification of a design described earlier by Gardiner (1983), and is shown in figure (3.5). The stainless steel capillaries of the earlier design have been replaced by quartz and the differential pumping tubes altered so as to give improved pumping speed. Differential pumping is via the rotary pump used to pump the Ar gas line, and also the 32 litres/sec diffusion pump. In a test measuring the current from an aluminium plate upon which was incident HeI (22.2eV) radiation, the intensity of the modified lamp has been found to be a factor of 15 times greater than that of the original design, giving a typical current of  $2 \times 10^{-8}$  Amps at lamp operating conditions of 1KV, 100mA. A change in the emphasis of the research program meant that no experiments were performed with the He discharge lamp, but the design is ready to be used in any future study.



Figure(3.5) Ultra-violet photon source.

### 3.2.5 HEMISPHERICAL ELECTRON ANALYSER

The electron analyser used for the angle resolved XPS and AES, and also to check sample cleanliness, was a Leybold Heraeus LHS 10 hemispherical electron analyser. A schematic diagram is shown in figure (3.6). The analyser incorporates a five element pre-retardation electron lens to define acceptance angles and the energy resolution of the system. An axial stop in the lens prevents any unwanted materials reaching the lens and improves the signal to noise ratio by preventing any scattered electrons from entering the hemispheres. The hemisphere and lens arrangement is surrounded by  $\mu$ -metal shields to minimize external magnetic fields. An EMI 9643/4B electron multiplier operated at 3KV is used to detect the electrons which traverse the analyser. The angular resolution used in the present work is  $\pm 2.5^\circ$  in the polar ( $\theta$ ) direction, and  $\pm 15^\circ$  in the azimuthal ( $\phi$ ) direction. Modification of these acceptance angles is a simple matter of exchange of the aperture diaphragm shown in figure (3.6), the aperture dimensions in both polar and azimuthal directions defining the acceptance angle at the sample. Various aperture dimensions were tried in test runs, the above acceptance angles were used as a compromise between signal intensity and angular resolution.

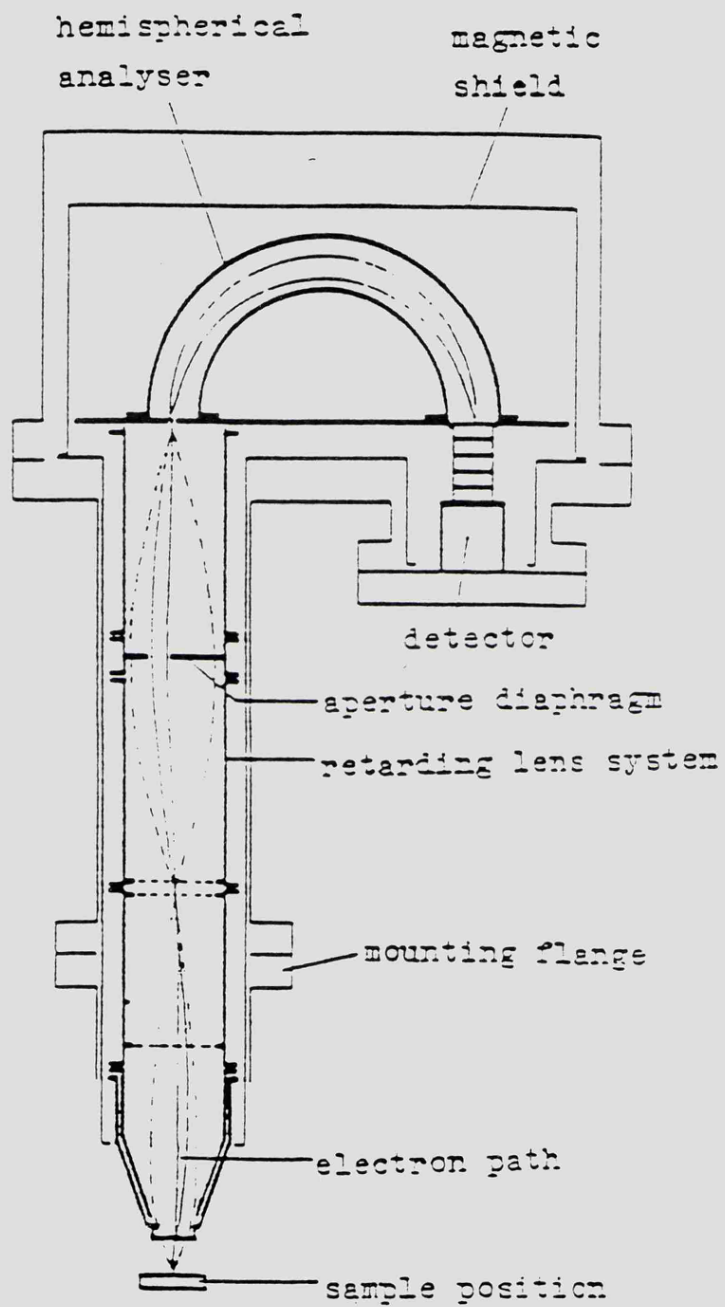
The transmission characteristics of the analyser obey the following equation, based on Louivilles' Theorem.

$$E \times \Omega \times F = \text{constant} \quad \text{---(3.3)}$$

Where E = electron energy

$\Omega$  = acceptance angle

F = analysed area



Figure(3.6) Hemispherical electron analyser.

The analyser is designed so that all emitted electrons from the sample that are selected by the input lens are injected into the hemispheres such that

$$E_{kin} \times F_s \times \Omega_s = E_o \times F_o \times \Omega_o \quad -(3.4)$$

Where  $E_{kin}$  = kinetic energy of emitted electrons

$F_s$  = viewed area of sample

$\Omega_s$  = acceptance angle at sample

$E_o$  = pass energy of hemispheres

$F_o$  = slit area

$\Omega_o$  = solid angle of injection into hemispheres

The five element lens is designed so that the sample area analysed is held constant such that

$$\text{magnification} = \frac{F_s}{F_o} = \text{constant} = 2 \quad -(3.5)$$

All electrons in the lens are injected into the hemispheres such that

$$\Omega_o = \text{constant} \quad -(3.6)$$

For a given slit size the resolution in the hemispheres is given by

$$\Delta E = p \times E_o \quad -(3.7)$$

where  $p$  is the relative resolution and is 1% for the slit size of 1mm x 20mm used.

The analyser can be operated in two modes, constant relative resolution and constant absolute resolution. i.e.  $\Delta E/E = \text{constant}$  and  $\Delta E = \text{constant}$ . For constant relative resolution

$$\frac{\Delta E}{E} = \frac{\Delta E}{E_{\text{kin}}} = \text{constant} \quad -(3.8)$$

$$\therefore \frac{pE_0}{E_{\text{kin}}} = \text{constant} = \frac{p}{B}$$

where  $B = \text{retarding ratio} = \text{constant}$

Since  $\Omega_0$  is constant, substituting into equation(3.4) for  $E_0$  and  $E_{\text{kin}}$  gives

$$\Omega_0 = \frac{F_s}{F_0} \times \frac{p}{B} \times \Omega_s = \frac{2p}{B} \times \Omega_s \quad -(3.9)$$

Therefore, in constant relative resolution mode, angular resolution is constant.

For constant absolute resolution,

$$\Delta E = \text{constant} = p \times E_0 \quad -(3.10)$$

$$\therefore E_0 = \text{pass energy} = \text{constant}$$

Then,

$$\Omega_0 = \text{constant} = 2p \times \Omega_s \times \frac{E_{\text{kin}}}{\Delta E} \quad -(3.11)$$

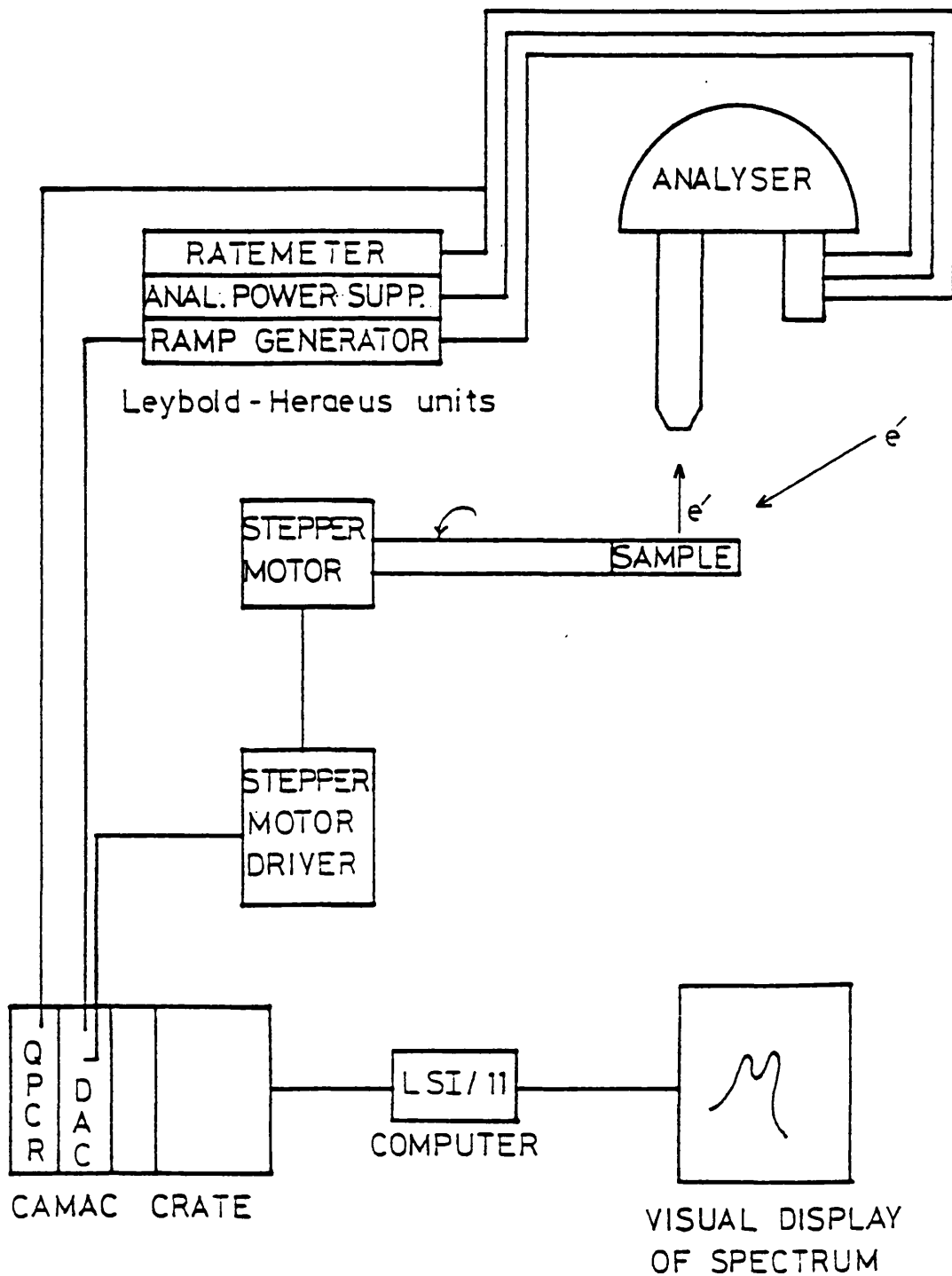
Therefore,  $\Omega_s$  must vary as  $E_{\text{kin}}$  is varied, with the acceptance angle becoming smaller as  $E_{\text{kin}}$  is swept to higher energies. It is important

that for all angle-resolved measurements the analyser must be operated in the constant relative resolution mode so that the acceptance solid angle at the sample is kept constant. For a more detailed description of this analyser and its electron lens, see Nöller et al (1974) and Polaschegg (1974 and 1976).

### 3.2.6 DATA ACQUISITION SYSTEM

Data is collected from both the RFA and the hemispherical electron analyser by means of an LSI/11 microcomputer connected through a CAMAC crate interface. The data collection arrangement for the hemispherical analyser has been designed to automatically collect data whilst rotating the sample through a chosen polar angle range and is shown schematically in figure (3.7). A typical polar angle electron intensity scan is collected as follows; a single pulse from the digital to analogue converter (DAC) in the CAMAC crate produces one step rotation of the stepper motor (200 steps giving  $1^\circ$  polar rotation of the sample) to move the sample to the desired start position. Once the sample is in position the relevant energy range for a given Auger or photoelectron line is scanned, the data being collected by feeding the pulses from the analyser pre-amplifier directly into the CAMAC counting register and automatically plotted on the computer terminal. A background (either integral or polynomial) is then fitted by taking into account the background either side of the measured peak. The area under the background subtracted curve is then calculated using a parallelogram rule, and stored on the LSI/11 Winchester hard disk. The sample is rotated to its next position and the above procedure repeated.

The computer and CAMAC is used to collect Auger spectra from the 3-grid LEED system during deposition, the CAMAC supplying the ramp voltage to the grids through a programmable high voltage power supply,



Q.P.C.R.— QUAD PRESET COUNTING REGISTER  
 D.A.C. — DIGITAL TO ANALOGUE CONVERTER

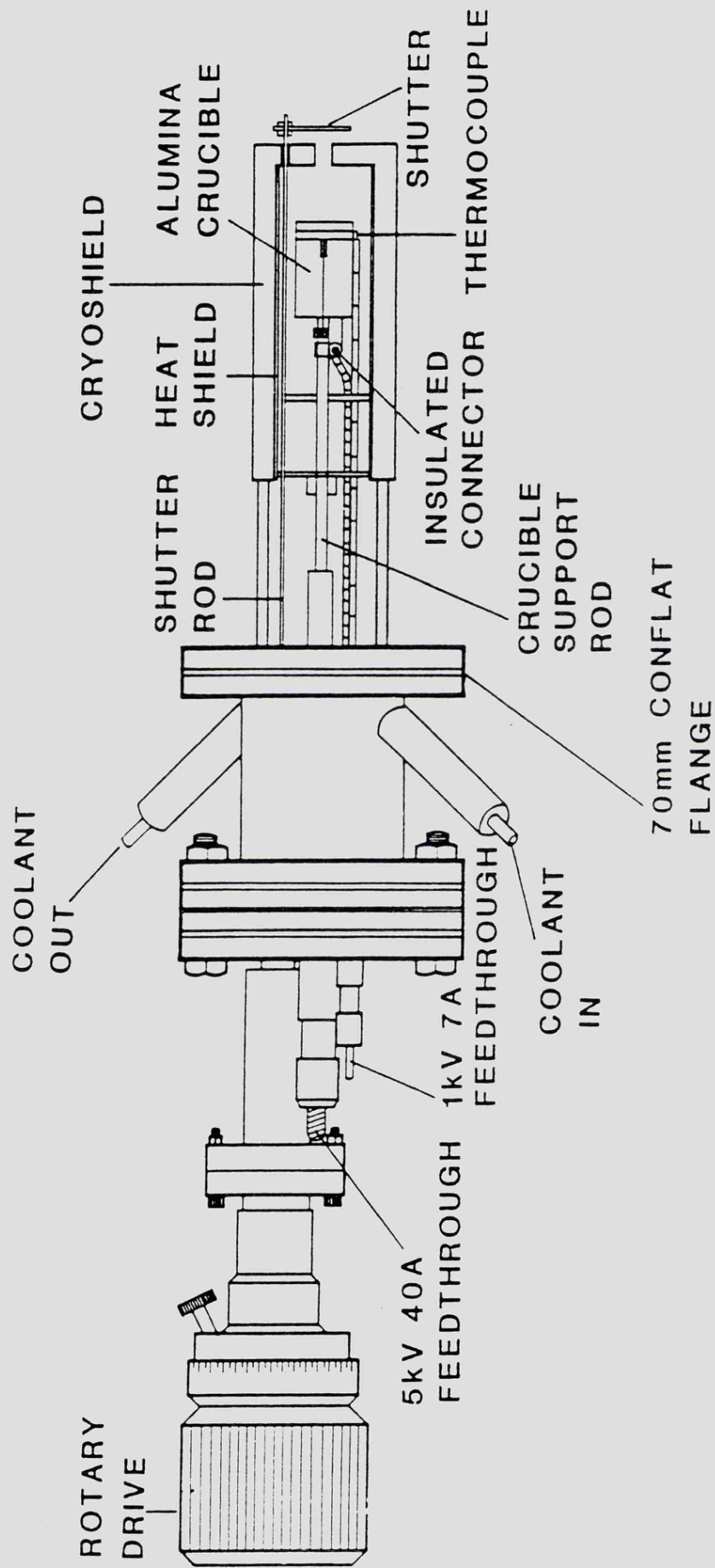
Figure(3.7) Schematic diagram of the data acquisition system.

and the data collected from the output of the lock-in amplifier and fed into the CAMAC for display on the terminal. Transfer of the data to the Leicester University Vax mainframe computer for further data analysis is possible via a Kermit transfer system.

### 3.2.7 SAMPLE PREPARATION

The circular Ag(001) samples of radius 6mm were spark cut to within  $0.1^\circ$  of the (001) plane from a 99.9999% (6N) pure Ag(001) obtained from Metal Crystals and Oxides Ltd. (Cambridge). The cutting was undertaken at the Department of Materials and Metallurgy, University of Birmingham. The 3mm thick discs were first mechanically polished to a  $\frac{1}{2}\mu\text{m}$  using diamond paste and then chemically polished. The chemical polishing solution used was a saturated solution of 200g of  $\text{CrO}_3$  in distilled water to which was added dilute HCl in the ratio 2:1. This mixture was then diluted with distilled water in the ratio 1:8. The samples were rinsed in distilled water before immersion in the polishing solution for ~30secs. After further rinsing in distilled water, the samples were swabbed with cotton wool to remove the white film produced by the action of the polishing solution.

After mounting the sample on a molybdenum sample block and pumping down to UHV, repeated cycles of Argon ion bombardment and annealing at  $500^\circ\text{C}$  were made until a sharp  $p(1 \times 1)$  LEED pattern with minimum diffuse background was observed. This cleaning cycle usually took ~7-10 days before a surface of sufficiently good quality was produced. Following deposition of an overlayer, the substrate was cleaned by Argon ion bombardment at 2KV  $20\mu\text{A}$  at room temperature, until no trace of the overlayer can be seen with either AES or XPS, and subsequent annealing at  $500^\circ\text{C}$ .



Figure(3.8) Knudsen cell vapour source.

### 3.2.8 VAPOUR SOURCES

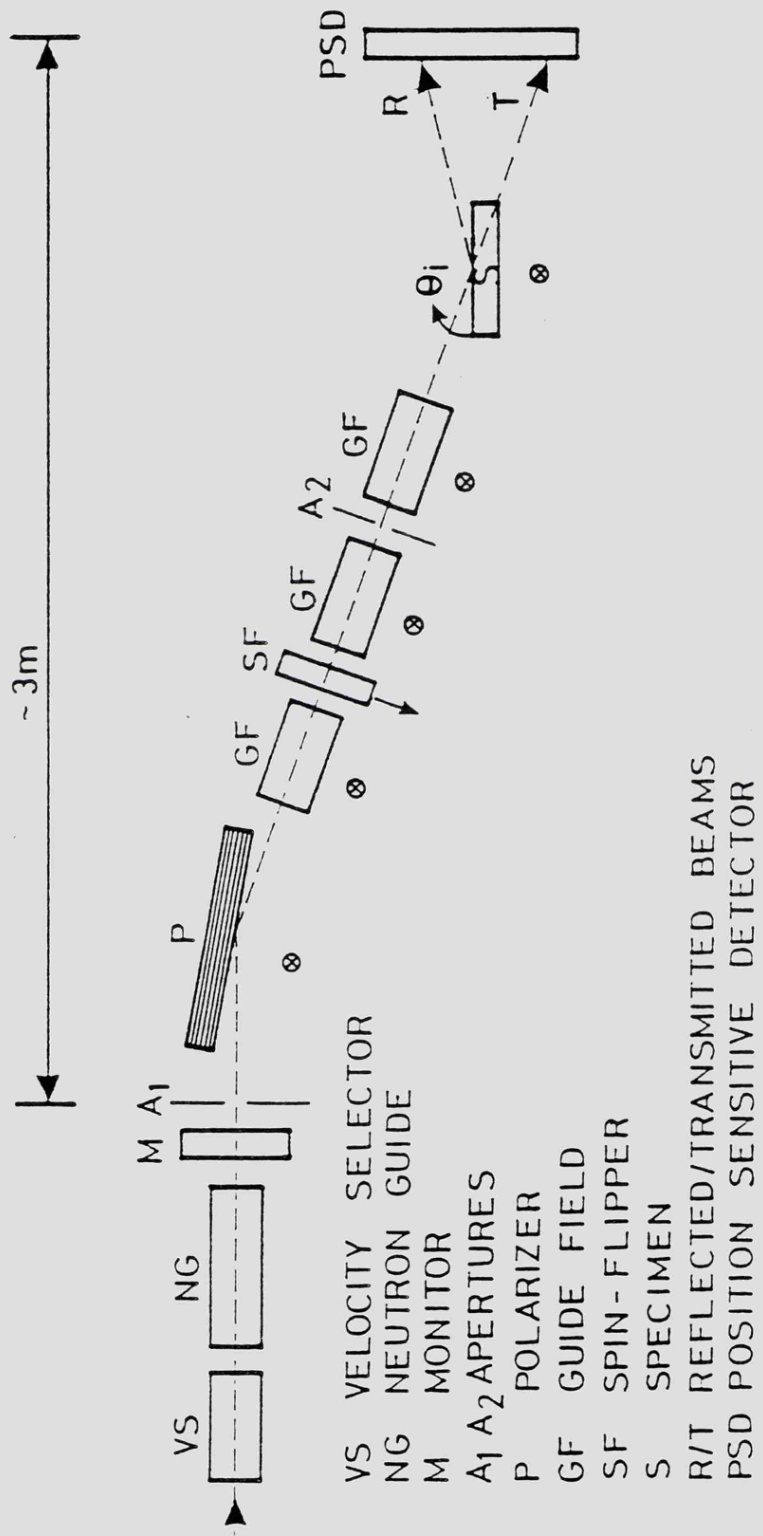
Metal overlayers were deposited from a Knudsen cell vapour source based on the design of Taylor and Newstead(1987) and shown in figure (3.8). It fits onto a standard 70mm conflat UHV flange and incorporates a cooling jacket and shutter mechanism. The evaporant is loaded into a 1cm<sup>3</sup> alumina crucible around which is wound a tungsten filament. The temperature is monitored with a chrome-alumel thermocouple located at the open end of the crucible. The whole crucible arrangement is surrounded by a cooling shroud, through which water or liquid nitrogen can be passed. The shutter is operated manually by a mini rotary motion drive. When powered by a stabilised power supply such as a Farnell TSV70, the vapour source can be held to temperatures within 1°C over many hours, and with careful outgassing the chamber pressure can be held below  $1 \times 10^{-10}$  Torr during deposition. AES scans across the surface of the crystal after deposition showed no sign of contamination and no appreciable difference in overlayer thickness. Typical operating conditions for the evaporation of chromium at a rate of ~2 monolayers per hour are an input of ~55 watts giving a crucible temperature of ~900°C.

## 3.3 POLARISED NEUTRON REFLECTION MEASUREMENTS (PNR)

### 3.3.1 EXPERIMENTAL ARRANGEMENT

As has been explained in section 2.3, PNR measurements require a very intense, highly collimated source of neutrons of long wavelength ( $\lambda \geq 10\text{\AA}$ ), and some means of varying the perpendicular component of the incident neutron wavevector  $q$ .

The PNR measurements were made on the small angle diffractometer D17 at the Institut Laue-Langevin, Grenoble; the experimental arrangement is shown in figure (3.9). The beamline was set up on an optical bench and



Figure(3.9) Schematic layout of Polarised Neutron Reflection beamline, indicating orientation of magnetic fields.

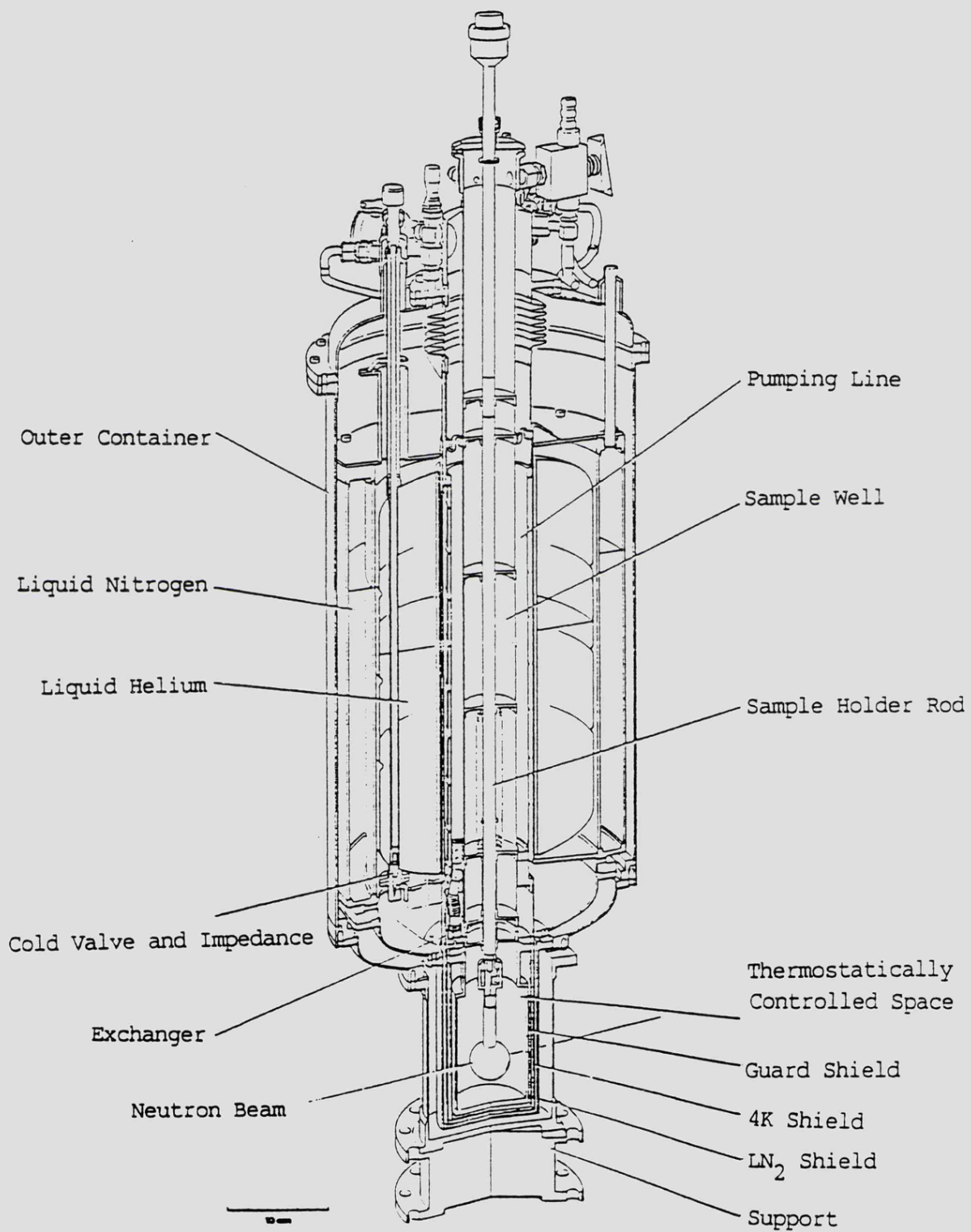
wavevector  $g$  varied by mechanical rotation of the sample about its vertical axis with 10 millidegree step resolution. An incident cold neutron beam of wavelength  $\lambda=12\text{\AA}$  was collimated by means of two cadmium apertures giving a beam divergence at the sample of  $10^{-3}$  rad. A mechanical velocity selector was used to define the wavelength to within  $\Delta\lambda=10\%$ . The beam was polarised by reflection from a Co-Ti supermirror (Schaerpf 1975 and Hayter et al 1978). The polarisation was retained by passing the beam through a series of guide fields made up of permanent magnets which gave a homogeneous magnetic field ( $H\sim 100$  Oe).

The beam polarisation could be inverted by a Mezei flipper (Mezei 1972), consisting of two orthogonally wound aluminium coils which cause a  $\pi/2$  Larmor precession of the neutron spin. The beam line was aligned optically by placing a laser in the beam position before the first cadmium aperture. The degree of polarisation was measured by placing a second Co-Ti supermirror in the sample position and measuring its flipping ratio.

The sample was mounted in a purpose built cell which had two Sm-Co permanent magnets located behind the sample to provide an applied magnetic field of 0.1T aligned in the plane of the sample surface. The cell was placed in a liquid helium cryostat with sapphire windows (to allow laser alignment of the sample), which is shown in figure (3.10). A large position-sensitive detector comprising a  $128\times 128$  array of  $5\text{mm}^2$   $\text{BF}_3$  detectors was positioned 2.83m from the sample to record the intensities of both the transmitted and reflected beams. Data was collected and processed by the D17 station Vax computer.

### 3.3.2 SAMPLE PREPARATION

The samples were prepared in the UHV system described in section



Figure(3.10) 'Orange-type' liquid helium cryostat.

3.2.1. The thin magnetic layers were deposited from the effusion cell described, the thickness being monitored using Auger electron spectroscopy (As-t plot). The thickness of the non-magnetic Ag overlayer was determined with a water cooled Leybold Heraeus XTM quartz oscillator film thickness monitor. The monitor was mounted on the vapour source flange and could be moved into the sample position (with the sample manipulator retracted) by a bellows drive mechanism. After calibrating the Ag flux, the thickness monitor was withdrawn and the sample manipulator moved in so that the sample was in the same position, and the Ag overlayer deposited. The thickness of the Ag overlayer has been independently fitted using the PNR data, and the calculated value has been found to be in agreement with the thickness monitor to within ~10%.

### 3.4 SURFACE X-RAY DIFFRACTION MEASUREMENTS

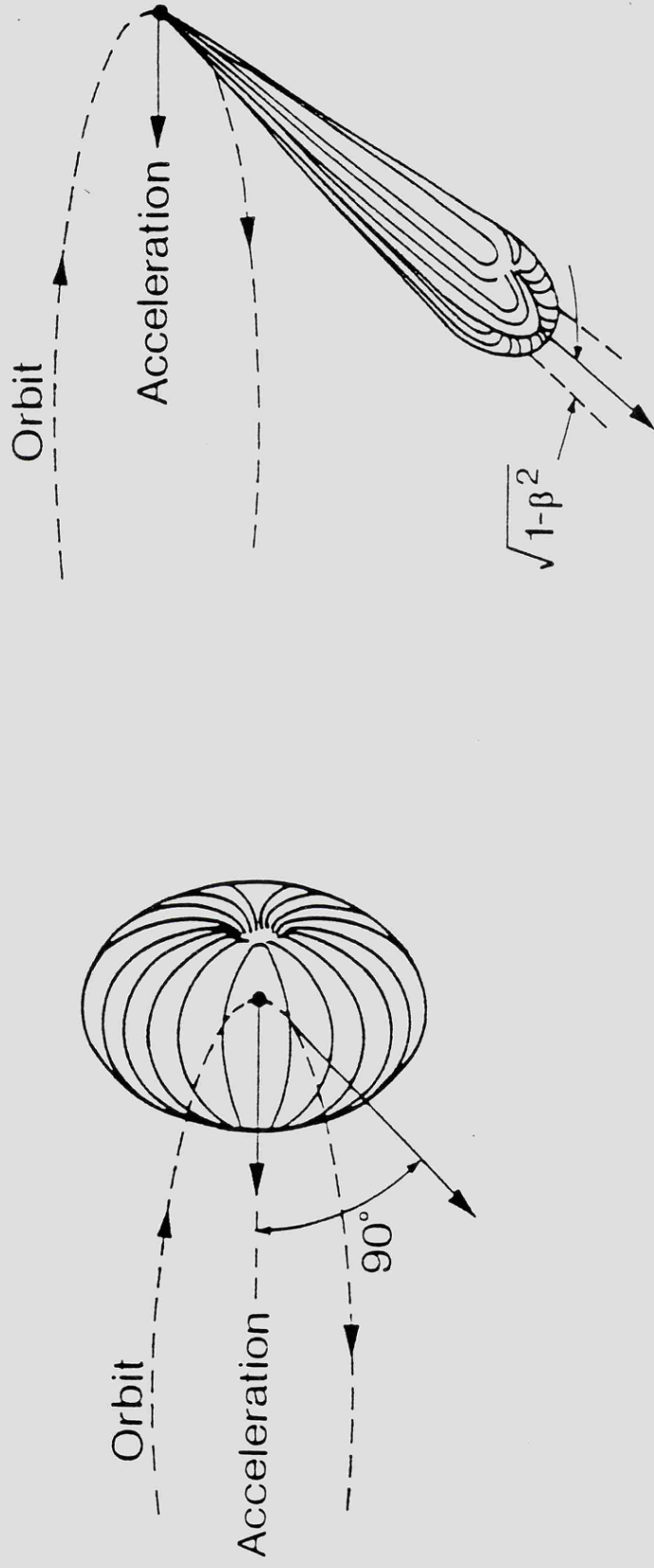
#### 3.4.1 SYNCHROTRON RADIATION

The X-ray diffraction measurements in this work were carried out using the unfocussed beam on station 4 of the wiggler beamline 9 at the Synchrotron Radiation Source (SRS) at Daresbury Laboratory.

Synchrotron radiation is produced by passing electrons around a circular orbit, causing them to be radially accelerated (see figure (3.11)). When the velocity of the electrons approaches the velocity of light, this radiation is limited to a very highly collimated beam in the instantaneous direction of flight at the bending magnet. The radiation has other useful properties, apart from its collimation: it is very intense and white, and so, using a suitable monochromator, is tunable. Also, the radiation is almost completely polarised in the orbit plane. The critical wavelength for synchrotron radiation is given by:-

$$\lambda_c = \frac{4\pi}{3} \frac{mc^2}{e} \beta \frac{1}{B\gamma^2} \quad - (3.12)$$

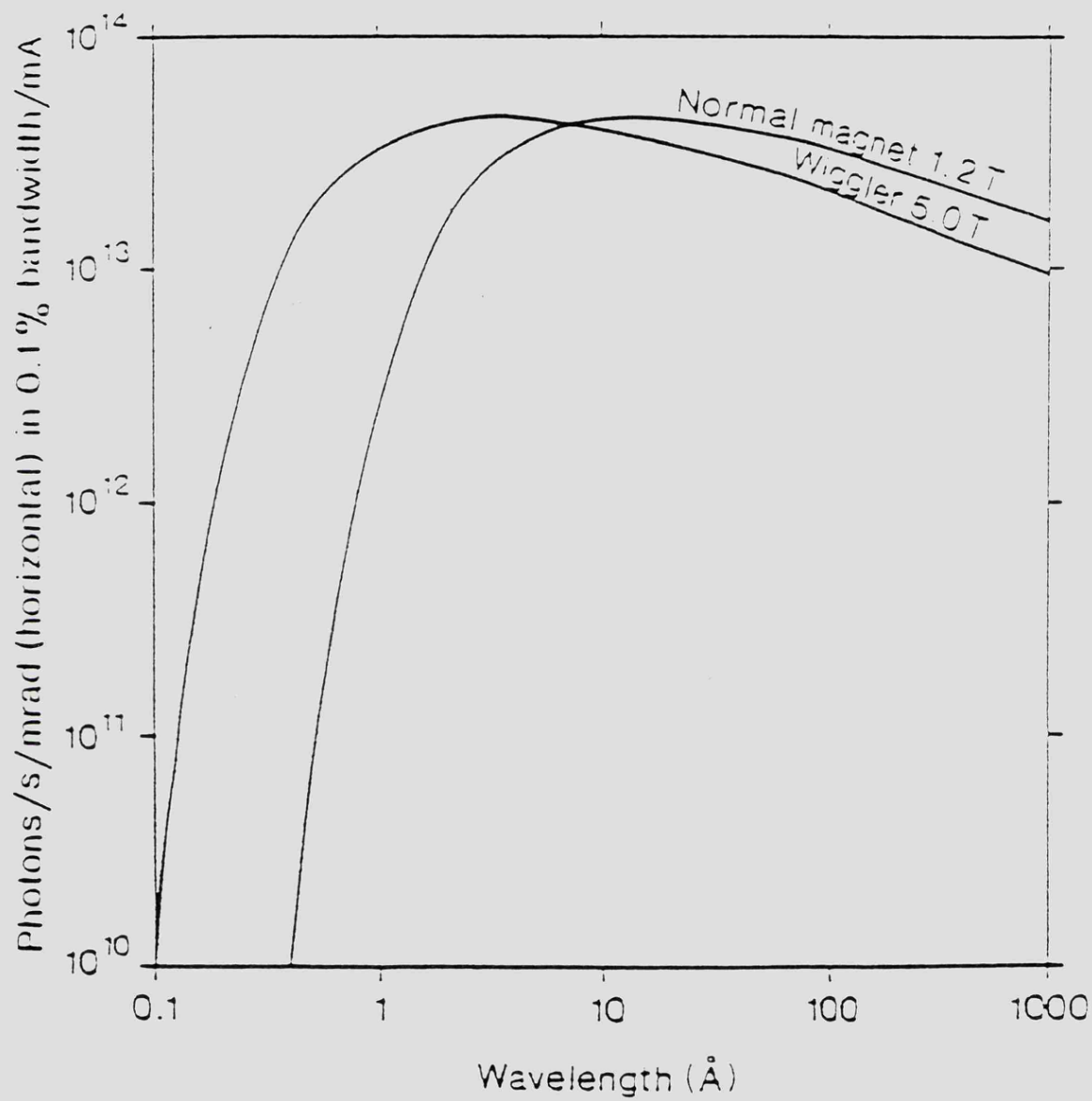
# Radiation Distribution Patterns From Orbiting Electrons



(a) Non-Relativistic Case ( $\beta \ll 1$ )

(b) Relativistic Case ( $\beta = 1$ )

Figure(3.11) Angular distribution of synchrotron radiation



Figure(3.12) Spectral curve of intensity vs. wavelength  $\lambda$  for both bending magnets and wiggler radiation at the SRS.

where  $m$  is electron mass,  $c$  is the velocity of light,  $e$  is the electron charge,  $\beta$  is the ratio of the electron velocity and the velocity of light,  $B$  is the magnetic field and  $\gamma$  is given by:-

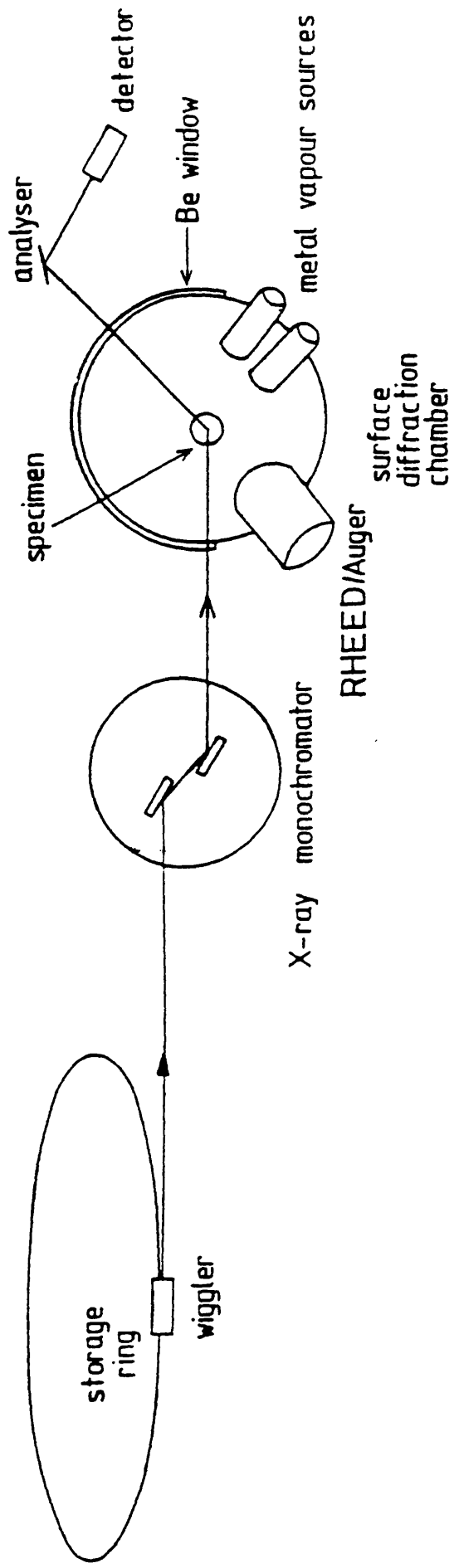
$$\gamma = \frac{eB\rho}{m\beta c^2} \quad - (3.13)$$

where  $\rho$  is the radius of curvature of the orbit

A wiggler is a series of magnets located in a straight section of the storage ring arranged so that the electrons are caused to traverse a sinusoidal path. The effect of the larger magnetic field of the wiggler is to shift the critical wavelength  $\lambda_c$  to a lower wavelength than that produced by the bending magnets. A spectral curve for the SRS is given in figure (3.12) for both the bending magnets and the wiggler on beamline 9. It can be seen that the wiggler intensity peaks for  $\lambda_c \approx 1\text{\AA}$ , which is ideal for (surface) X-ray diffraction experiments. At the SRS, a stored beam of around 250mA with a lifetime of ~25hrs is achieved after ramping the stored beam to 2GeV and the wiggler to 5 Tesla.

#### 3.4.2 STATION 9.4 BEAMLINE AND X-RAY MONOCHROMATOR

Station 9.4 at the SRS uses unfocussed beam from the wiggler, the beamline being shown schematically in figure (3.13). The beam is defined by a set of four-jaw slits mounted immediately before the position where the beamline enters the station hutch. The wavelength is defined by a channel cut Si(111) monochromator mounted on a rotary table inside a stainless steel vacuum vessel. The beam dimension is defined by a set of four-jaw slits immediately before the monochromator crystals and a second set of slits situated at the exit of the monochromator vessel, and the beamline then ends just before the sample UHV chamber with a small



Figure(3.13) Schematic diagram of beamline 9.4 at the SRS.

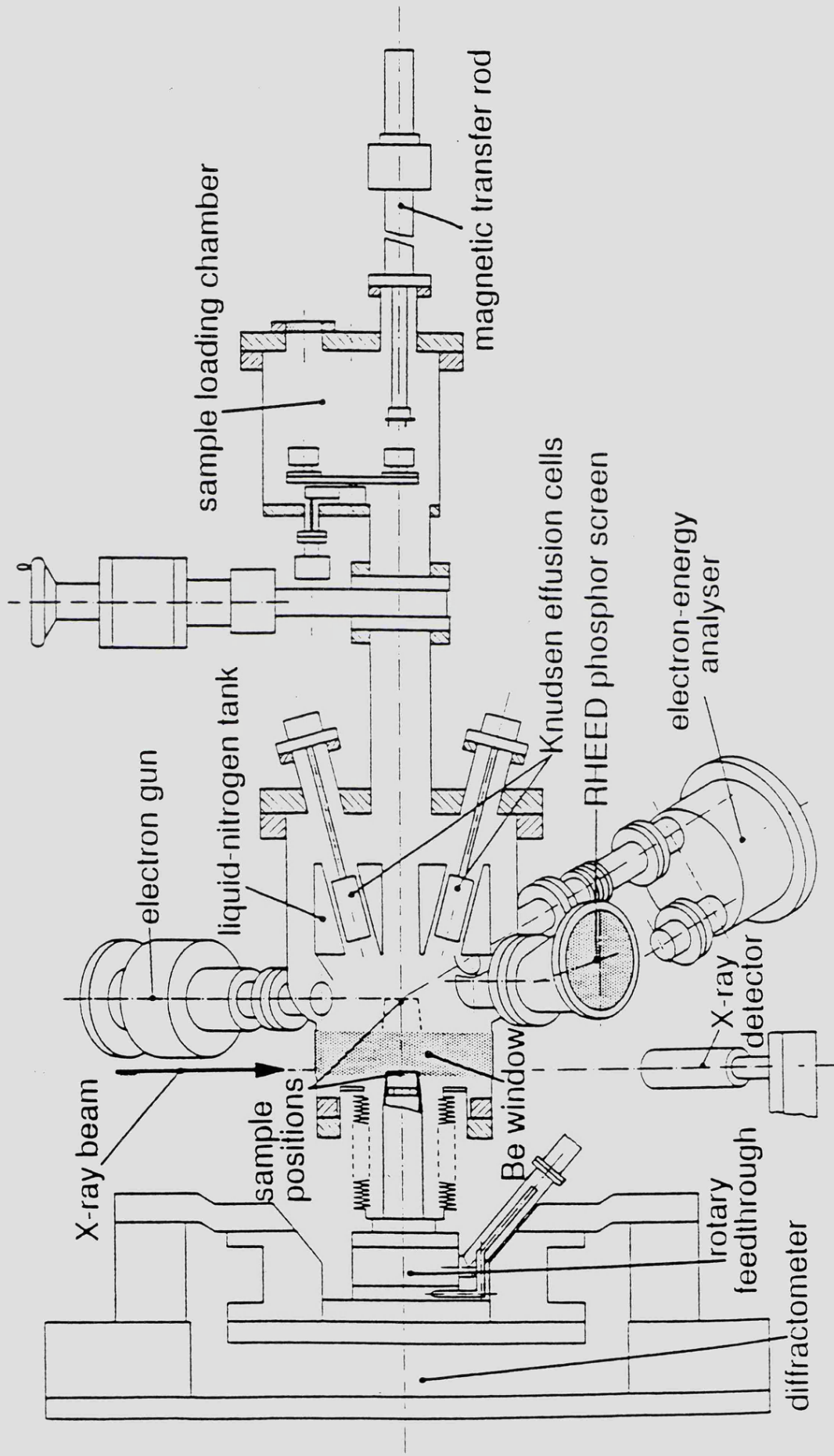
beryllium window. Between the set of slits at the exit aperture of the monochromator and the end of beamline is a NaI scintillation beam monitor, used to normalise all measured intensities. After setting the wavelength and slits in the beamline, the monochromator vessel and accompanying beam pipe is evacuated and filled to 1 atmosphere of He to reduce air scattering. It is then possible to finally set the beam dimensions by adjustment of a set of slits fixed to the end of the beamline after the Be window.

### 3.4.3 SURFACE X-RAY DIFFRACTION UHV CHAMBER

The purpose built UHV system used at Daresbury for this experiment was designed and manufactured at the F.O.M. Institute, Amsterdam and has been described in more detail elsewhere (Vlieg et al 1987<sup>1</sup>).

The system (figure 3.14) incorporates a UHV chamber and a sample transfer system to enable exchange of samples without breaking vacuum. The UHV chamber is pumped by a 300litre/sec turbomolecular pump, a 200litre/sec ion pump and a liquid nitrogen cooled TSP. After bakeout at 160°C for 24 hours, the base pressure is  $2 \times 10^{-11}$  mbar. The sample transfer chamber is pumped by a 300 litres/sec turbomolecular pump which achieves a pressure of  $< 10^{-6}$  mbar in minutes to enable quick sample transfer if necessary. The samples are moved from the preparation chamber into the UHV chamber by a magnetic drive arrangement.

The X-ray beam is incident on the sample and diffracted through a beryllium window which subtends an arc of 200° about the sample position and allows angles of incidence of up to 20° relative to the sample surface. To enable substrate and adsorbate characterisation by RHEED and AES the chamber can be repositioned by means of a linear sliding table. The sample holder is connected to the chamber by a bellows to enable this



Figure(3.14) Schematic diagram of surface X-ray diffraction UHV system, as viewed from above.

linear movement.

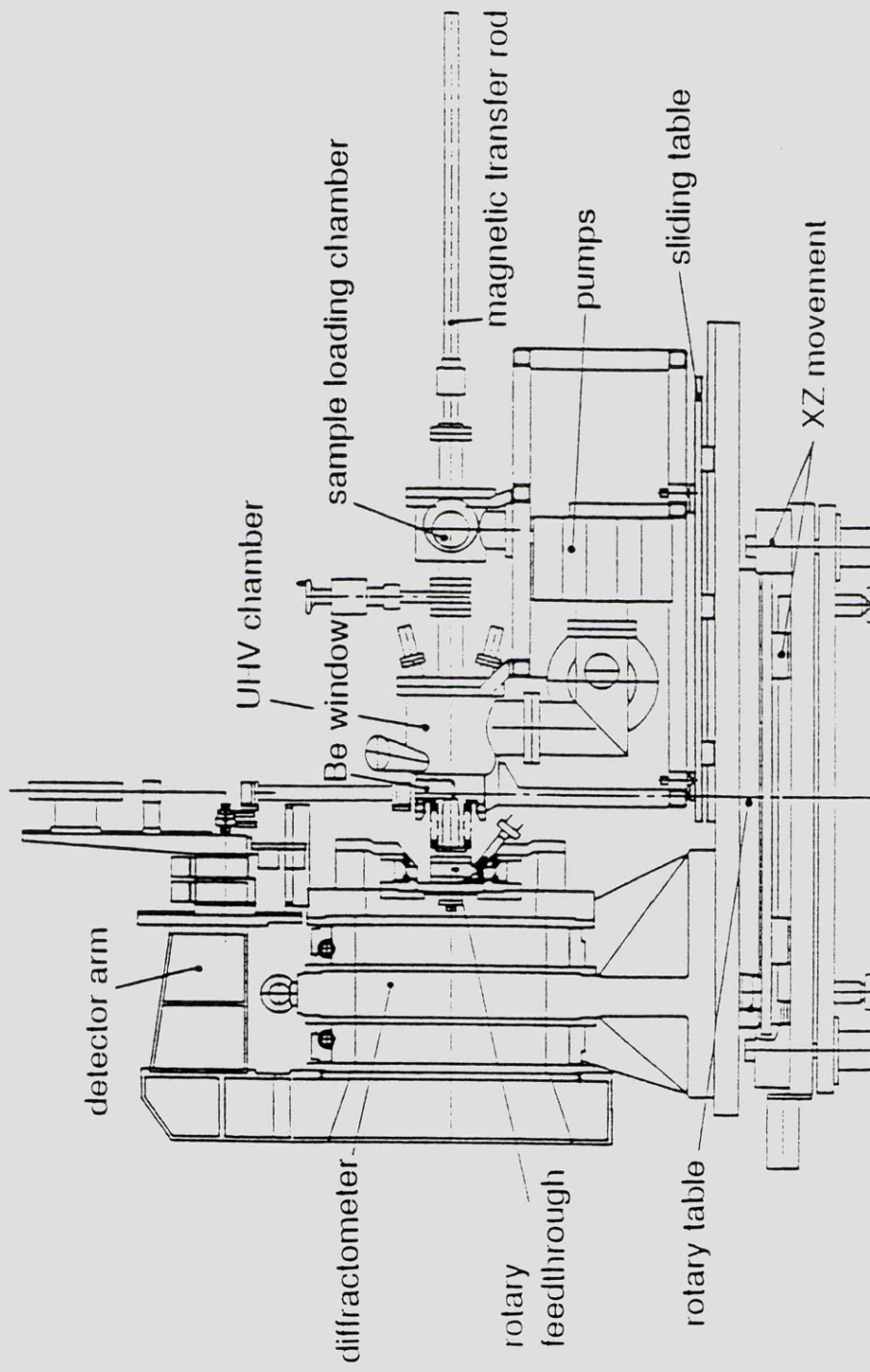
The sample is mounted in a sample holder (Vlieg et al 1987<sup>1</sup>) equipped with electron beam bombardment heating, to give sample temperatures in excess of 1000°C. The sample holder arrangement is coupled to the five circle diffractometer (Norris et al to be published), figure (3.15), through a two stage differentially pumped rotary feedthrough and bellows. The bellows unit also allows for a  $\chi$  rotation of  $\pm 18^\circ$  of the sample relative to the chamber.

Molecular Beam Epitaxy (MBE) deposition of adsorbates is possible as the system can be equipped with Knudsen cell vapour sources. these cells have shutters which are operated with compressed air enabling growth to be monitored using X-rays (see Vlieg et al 1988). the cells are water cooled and surrounded with a liquid nitrogen cooling tank and are based on the design of Marée et al (1987).

#### 3.4.4 5-CIRCLE DIFFRACTOMETER AND SAMPLE ALIGNMENT

The purpose built surface X-ray diffractometer is based on the design of Gibbs and also the later design of Fuoss and Robinson (1984) and comprises an ordinary 4-circle diffractometer on a rotary table with a vertical scattering plane. The vertical scattering plane is necessary as the polarisation of synchrotron radiation can lead to near zero polarisation factors for scattering angles of  $\sim 90^\circ$ . Figure (3.15) is a schematic diagram of the diffractometer with all angles set to zero. The diffractometer is completely computer controlled, with all diffractometer angles being calculated using the method described by Vlieg et al (1987<sup>2</sup>), and all circles being moved by DC motors. Encoders on the motors mean that circles can be moved with 0.125 millidegree step resolution.





Figure(3.16) X-ray diffraction chamber coupled to the 5-circle diffractometer via the rotary feedthrough.

The azimuthal crystal orientation relative to the X-ray beam is determined by RHEED and then the physical surface normal is set perpendicular to the plane of the diffractometer circles by the reflection of a low divergence laser beam from the sample. The  $\chi$  and  $\phi$  circles are set so that there is less than 1mm movement in the laser reflection at a distance of ~4m from the sample during full rotation of the  $\omega$  circle. Using these values of  $\chi$  and  $\phi$  and the lattice spacings of the crystal, a set of trial values for the circles for given reflections can be obtained using the method described by Vlieg et al (1987<sup>2</sup>). By then optimizing in  $\phi$  for these reflections and then re-inputting the optimized values into the computer program, the program parameters are usually sufficiently accurate to allow the taking of data to begin. Normally during alignment four or five in-plane and one or two out-of-plane reflections are used. By optimizing the  $\delta$  circle for a few reflections, one can obtain an independent calibration of the wavelength. Scans in reciprocal space can be made by varying all circles, but the most usual type of scan is a  $\phi$  scan where only the  $\phi$  circle is rotated across a diffraction rod.

#### 3.4.5 DATA ACQUISITION

The diffracted X-rays are recorded by a Ge solid state detector mounted on the  $\delta$  arm ~700mm from the sample. A set of adjustable slits allows for the desired resolution to be set both in the horizontal and vertical directions. Between the detector and the sample a tube with mylar windows at each end is rigidly fixed and filled with He to reduce air scattering.

The detector and monitor counts are fed to the station  $\mu$ -Vax computer via a CAMAC crate and together with the circle settings, stored on data files. These data files can be analysed in situ or transferred to

the Leicester University mainframe computer for further analysis.

#### 3.4.6 SAMPLE PREPARATION

The Ge samples used in this work were kindly lent by the F.O.M Institute, Amsterdam and had been cut and polished to within  $0.05^\circ$  of the (001) surface plane (One sample was deliberately miscut as explained in chapter 6 of this thesis) at Philips Research Laboratories Eindhoven, The Netherlands. Once in UHV each sample was cleaned by an initial pre-anneal of  $480^\circ\text{C}$  for 15 minutes followed by argon ion bombardment at 800V  $1\mu\text{A}$  for 10 minutes before finally annealing at  $710^\circ\text{C}$  for 15 minutes followed by a slow cool ( $\sim 1^\circ\text{C}/\text{sec}$ ).

After alignment and checking with RHEED, the above procedure was repeated until there was no improvement in the fractional order signal of say, the  $(0, 3/2, 0.03)$  rod; that is, no further decrease in half width and no further increase in integrated intensity.

## CHAPTER 4

### THE INITIAL STAGES OF THE GROWTH OF Cr AND Co ON Ag(001) STUDIED USING FORWARD FOCUSING OF MEDIUM ENERGY ELECTRONS

#### 4.1 Introduction

#### 4.2 Epitaxial Growth Of Cr On Ag(001)

##### 4.2.1 Introduction

##### 4.2.2 LEED And As-t Results

##### 4.2.3 Polar Angle Auger Electron Intensity Results

##### 4.2.4 Discussion

#### 4.3 Epitaxial Growth of Co On Ag(001)

##### 4.3.1 Introduction

##### 4.3.2 LEED and As-t Results

##### 4.3.3 Polar Angle Auger Electron Intensity Results

##### 4.3.4 Discussion

#### 4.4 Summary

## CHAPTER 4

### THE INITIAL STAGES OF THE GROWTH OF Cr AND Co ON Ag(001) STUDIED USING FORWARD FOCUSSED MEDIUM ENERGY ELECTRONS

#### 4.1 INTRODUCTION

The correlation between the structure and properties of ultrathin metal overlayers on single crystal substrates has been the focus of much interest (see for example Chambers et al, 1984 and Egelhoff, 1984). Particular attention has been paid to the effects of lattice mismatch and strain on the electronic and magnetic properties of the overlayer (Miranda et al, 1983 and Dürr et al, 1989).

LEED, As-t and polar angle dependent Auger electron intensity measurements are presented here for both Cr/Ag(001) and Co/Ag(001). The main interest of this work is to try and understand the initial growth mode and structure of the overlayers prior to further studies on their magnetic properties (see chapter 5). Ag makes a good substrate for 3d transition metal overlayers since it is relatively inert and tends not to form alloy structures. Measurements of the initial growth modes of Fe (Smith et al, 1982), Mn (Newstead et al, 1988) and Cr (Newstead et al, 1987) on Ag(001) have already been performed.

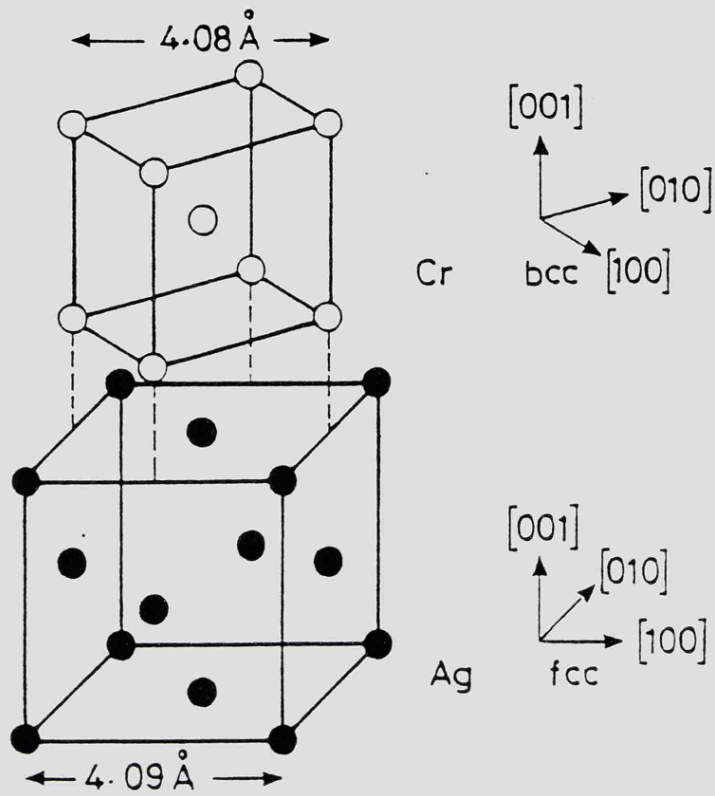
Forward scattering measurements using electrons of medium kinetic energy have been shown to indicate the structure of overlayers, and the growth mode of the first few epitaxial layers (see chapter 2). By careful measurement of the position of polar angles at which peaks in electron intensity occur, information about strain and relaxation of the adsorbed layers may also be obtained.

## 4.2 EPITAXIAL GROWTH OF Cr ON Ag(001)

### 4.2.1 INTRODUCTION

There is much current interest in ultrathin Cr overlayers due to predictions of novel magnetic properties in such structures (see for example Fu et al, 1985 and Chapter 5 of this thesis). Ag makes an ideal substrate for Cr since its nearest neighbour distance of 2.89Å matches the bulk Cr BCC lattice parameter of 2.88Å to within 0.4%. One would expect that Cr would grow epitaxially on Ag(001) in the bulk BCC phase with little strain, and with its lattice rotated 45° with respect to the FCC Ag bulk lattice (see figure (4.1)).

Structurally, Au is very similar to Ag, having an FCC structure with nearest neighbour distance of 4.08Å (compared with 4.09Å for Ag). Therefore, using the same argument one would expect Cr to grow in a similar manner to that on Ag(001). However, this is not the case, as a number of workers have proposed conflicting growth modes for the Cr/Au(001) system. Zajac et al (1985) first showed that Cr adatoms occupy the fourfold hollow sites and stabilise in a (1x1) registry, indicating a sharp interface between the Cr and Au, with the Cr overlayer in the BCC phase as expected. Angle resolved photoemission experiments undertaken by O'Neill and Weaver (1988) on Cr/Au(001) have supported the basic model of Zajac et al for a sharp interface by annealing the interface at -100-120°C, but make no comment on the phase of the Cr layers. In earlier work, Brodsky (1981,1983) and Brodsky et al (1982) observed superconductivity in Au/Cr/Au(001) sandwiches and proposed that an FCC phase of Cr was formed at the interface involving an unprecedented 41% expansion of the Cr lattice. This has been supported by X-ray diffraction measurements undertaken by Durbin et al (1988), and band structure calculations made for FCC Cr by Xu et al (1984) have supported the claim of superconductivity. Extended x-ray absorption fine structure



Forward scattering from substrate and overlayer.

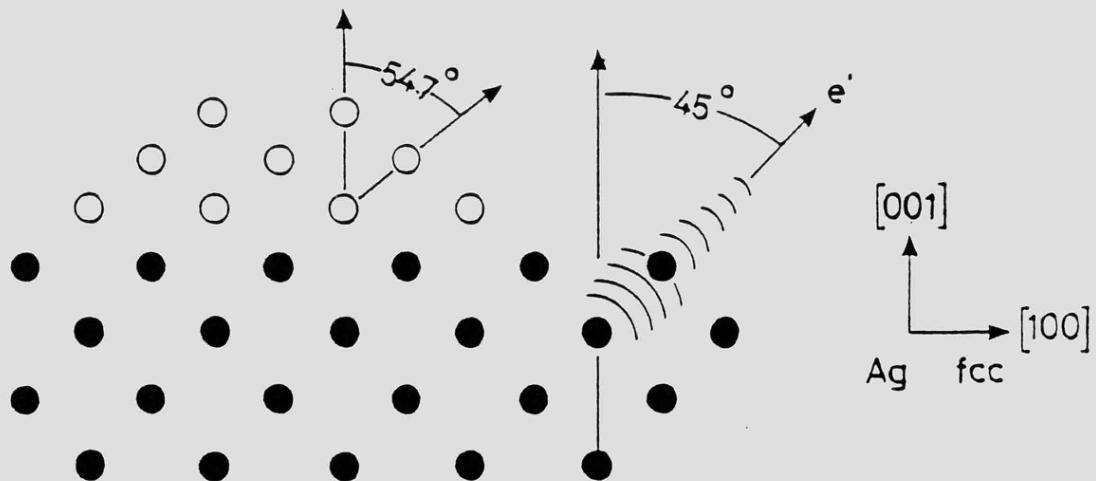


Figure (4.1) Schematic diagram showing the matching of the FCC Ag(001) lattice with the 45° rotation of the BCC Cr lattice. The bottom diagram shows the expected polar angles that electron intensity peaks should be observed due to forward scattering.

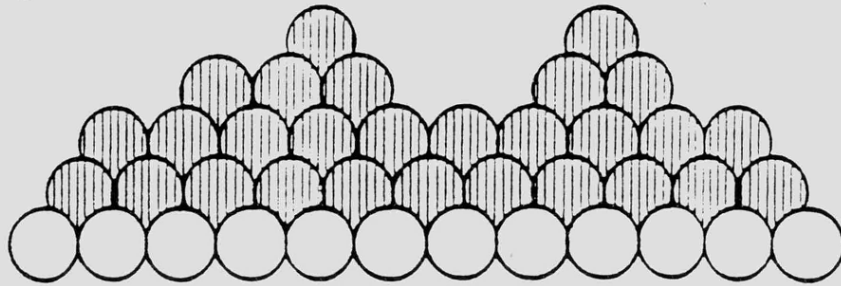
measurements in the same paper by Durbin et al (1988) tend, however, to favour the BCC structure.

Recent work by Hanf et al (1987, 1988) using LEED, core-level and angle-resolved photoemission have proposed the formation of a diffuse interface between Cr and Au(001) characterised by an epitaxial random substitutional  $Au_{1-x}Cr_x$  FCC alloy. For Cr deposited at room temperature (RT) the interface extends to 2-3layers and more at higher temperatures. At coverages exceeding ~5ML, epitaxial BCC Cr was produced. This may explain the conflicting previous results for Cr/Au(001), as Zajac et al (1985) pointed out that Cr entering substitutionally into the FCC Au lattice may give an FCC Cr signature.

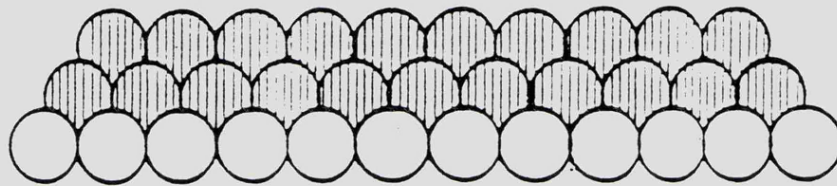
There has been only one previous study of the formation of the Cr/Ag(001) interface, by Newstead et al (1987). Unlike Au, Ag is immiscible with Cr. The bulk Ag-Cr alloy phase diagram shows a wide miscibility gap above the melting point, precluding significant solubility at low temperatures. By measuring an As-t plot along with LEED and secondary-electron-emission crystal current it was proposed that the Cr initially adsorbs in the fourfold hollow sites to a coverage of 0.33ML after which the overlayer continues to grow in the form of bilayers until the completion of the second monolayer. Above 2ML it was proposed that island formation occurs (see figure (4.2)), this growth behaviour having been predicted for a general system when monolayer platelets reach a critical size (Stoyanov and Markov, 1982). A similar growth mechanism is believed to occur for Fe/Pd(111), (Binns et al (1986)). Newstead et al proposed that the overlayers were BCC, but could not justify it experimentally.

Presented here are LEED, As-t and polar angle auger electron

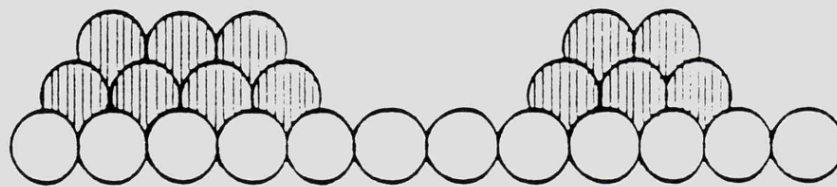
$$\theta > 2.0$$



$$\theta = 2.0$$



$$0.33 < \theta < 2.0$$



$$\theta < 0.33$$



Figure (4.2) Proposed growth mode for Cr/Ag(001) at room temperature, from Newstead et al (1987).

intensity measurements on the initial stages of epitaxy of Cr/Ag(001). The results are consistent with those of Newstead et al for the interface formation and it is confirmed that the Cr grows in the BCC phase.

#### 4.2.2 LEED AND As-t RESULTS

The As-t plot obtained by Newstead et al for Cr/Ag(001) showed two breaks at evaporation times  $t_1$  and  $t_2$ , separated by straight lines. The ratio of  $t_1:t_2$  was found to be (0.17:1). By using the expression for signal intensities given by:-

$$I = I_0 \exp(-x/\lambda) \quad - (4.1)$$

where  $I$  is the intensity,  $I_0$  the initial intensity,  $x$  the coverage in ML and  $\lambda$  the mean free path for the electrons in ML and using the empirical expression given by Seah and Dench (1979) for electron mean free path:-

$$\lambda(E) = 538E^{-2} + 0.41(aE)^{1/2} \quad - (4.2)$$

where  $a$  is the monolayer thickness in nM,  $E$  is the electron energy in eV, and  $\lambda$  is given in ML, Newstead et al were able to estimate the break at  $t_2$  to be at a coverage of 2.0ML, and thus the break at  $t_1$  to 0.33ML. Also it was found that throughout growth the LEED pattern remained  $p(1 \times 1)$  which faded rapidly after  $t_2$ .

The Cr layers in this work were deposited onto Ag(001) substrates held at room temperature from the Knudsen cell vapour source described in chapter 3. Room temperature deposition was used as the work of Newstead et al indicated that at higher temperatures the initial break in the As-t plot occurred at lower coverages. At lower temperatures, the problem of keeping the Cr clean becomes more difficult and so such temperatures were

not attempted. The Ag samples were mechanically and chemically polished as described in section 3.2.7, and then  $\text{Ar}^+$  bombarded and annealed at  $500^\circ\text{C}$  so that the LEED yielded a sharp  $p(1 \times 1)$  pattern with minimal diffuse background and there was no sign of impurities using either AES or XPS.

During deposition the chamber pressure rose from a base value of  $2 \times 10^{-11}$  Torr to  $\sim 8 \times 10^{-11}$  Torr. A low vacuum is required as Cr is an efficient getter. Cr growth was monitored by measuring the peak-to-peak height of the differentiated Ag  $M_{4,5}N_{4,5}N_{4,5}$  (356eV) Auger intensity as a function of deposition time. The resulting As-t plot is shown in figure (4.3). As can be seen the As-t plot has two well defined breaks at deposition times of  $t_1$  and  $t_2$ , in agreement with the work of Newstead et al. The first break, at  $t_1$ , was found to occur consistently at an intensity of  $I/I_0 = 0.80$  but the position of the second break, at  $t_2$ , varied. The ratio of the times  $t_1:t_2$  was within the range  $4.5 < R < 7.5$  with an average value of 6, in agreement with the result of Newstead et al. The variation in intensity at  $t_2$  gave an uncertainty in the coverage, as described by equations (4.1) and (4.2) of  $1.82 < \theta < 2.25$ . The coverage calibration of Newstead et al was thus taken to be correct. That is, the initial break in the As-t plot corresponds to a coverage of 0.33ML, and the break at  $t_2$  to 2.0ML.

The LEED pattern remained  $p(1 \times 1)$  throughout the deposition. It faded after the second break at  $t_2$ , in agreement with Newstead et al, indicative of disordering, which is proposed to be due to island formation.

#### 4.2.3 POLAR ANGLE AUGER ELECTRON INTENSITY MEASUREMENTS

For polar angle electron intensity measurements made on the clean

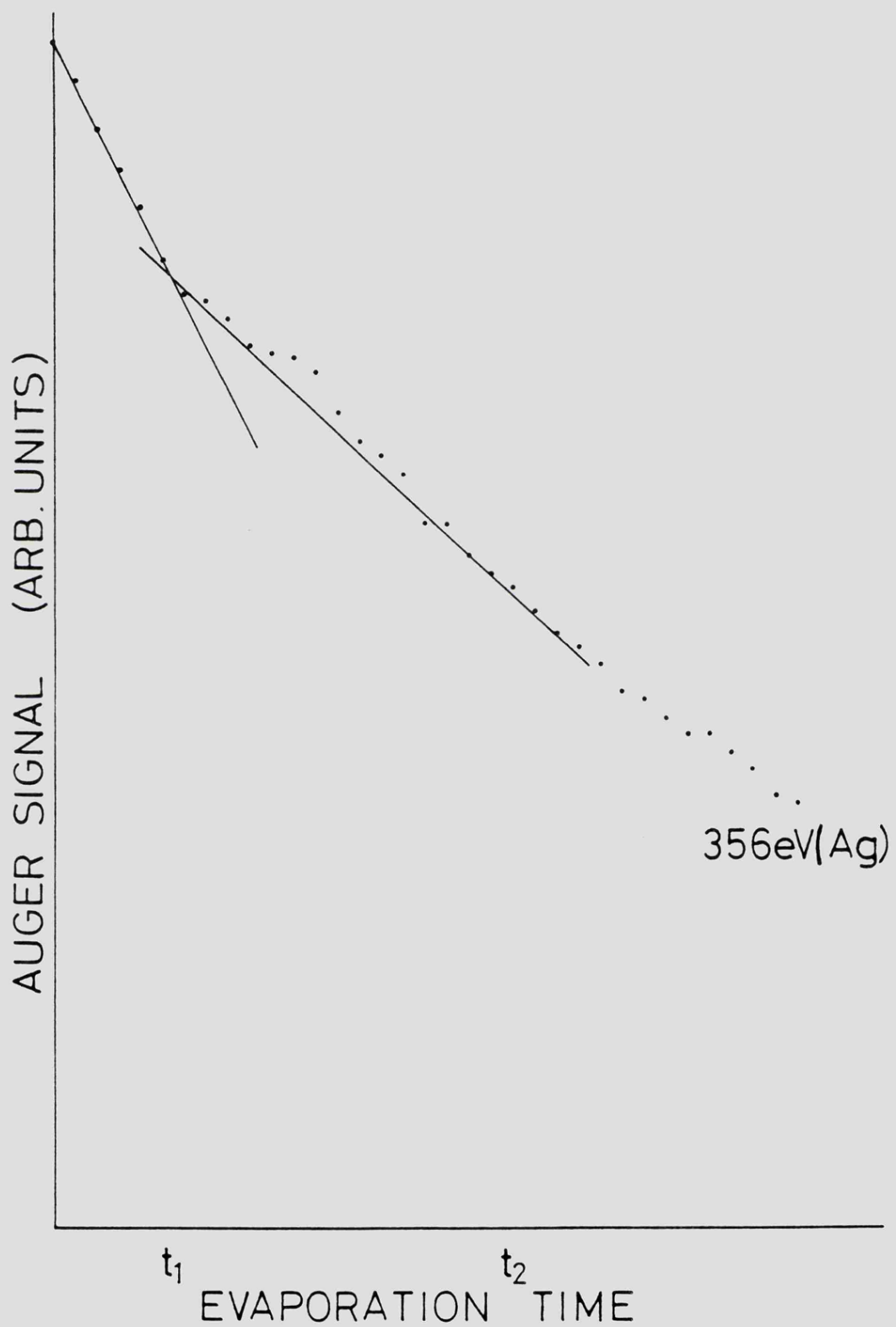


Figure (4.3) Curve showing variation of the Ag MNN (356eV) Auger electron intensity with Cr deposition.

Ag(001) substrate, the most intense Ag Auger electron emission line, the Ag  $M_{4,5}N_{4,5}N_{4,5}$  (356eV), was used. It was excited by an incident electron beam of energy 2.8KV. Alternative emission lines with kinetic energy in the correct region were the Ag  $3d_{3/2}$  and  $3d_{5/2}$  core level photoemission lines excited by the laboratory X-ray source. They were not used because of their lower intensity.

For the Cr overlayers, the Cr  $L_{3M_{2,3}M_{2,3}}$  (489eV) Auger emission line was used, excited by an incident electron beam. The most intense Cr core level photoemission lines of the correct kinetic energy were the Cr  $2p_{1/2}$  and  $2p_{3/2}$ . Overlap of these lines with the Ag  $3p_{1/2}$  and Ag  $3p_{3/2}$  core levels meant that in any polar angle scans it would be impossible to separate the substrate and overlayer contributions, and so the Cr LMM Auger line was the only possible choice.

Figure (4.4) shows polar angle Auger electron intensity curves for Ag(001) both clean and with various Cr coverages, in the [100] Ag FCC azimuth. The curves were taken by measuring the relevant peak-to-peak heights of the differentiated Auger lines as a function of polar angle  $\theta$  in  $1^\circ$  steps with  $0.25^\circ$  resolution. The clean Ag curve shows dominant intensity peaks at  $\theta = 0^\circ$  and  $45^\circ$  with the surface normal, corresponding to forward scattering of electrons along the [001] and [101] axes of the bulk FCC Ag lattice, as expected (see figure (4.1)). The weaker features at  $\theta = 20-30^\circ$  are due to first order diffraction and interference effects as well as forward scattering and cannot be attributed as being due to simple forward scattering from nearest- or next-nearest-neighbour atoms (Bullock and Fadley, 1985 and Poon and Tong, 1984).

For the 5.0ML Cr layer, intensity peaks are found at  $\theta = 0^\circ$  and  $54^\circ$ , with no peak at  $45^\circ$  as would be expected for an FCC structure. The

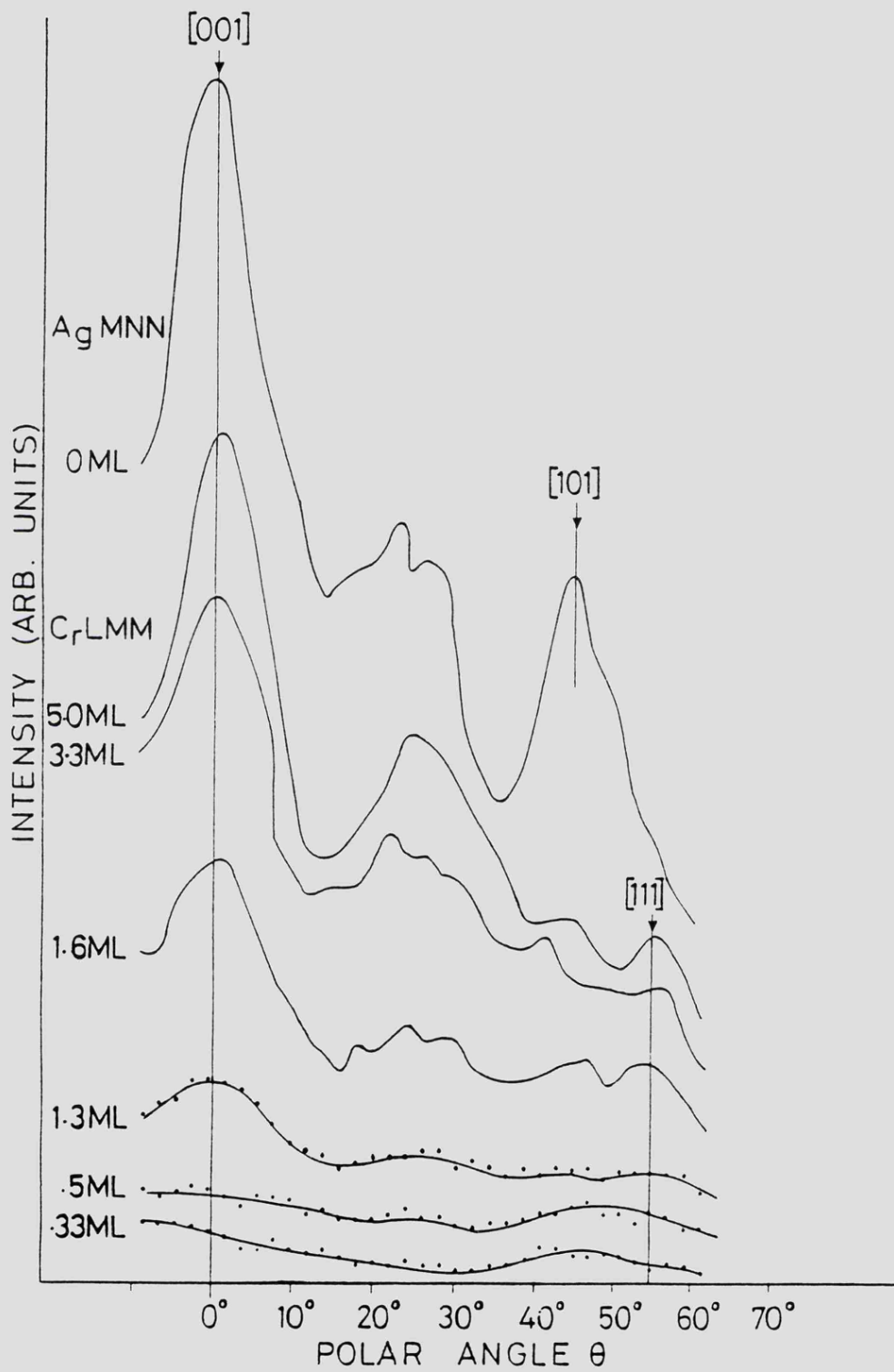


Figure (4.4) Polar angle Auger electron intensity variation for clear Ag(001), and various Cr coverages in the Ag [100] azimuth

54° feature can be attributed to forward scattering along the [111] axis of the BCC Cr lattice which implies that the BCC lattice is rotated by 45° with respect to the FCC Ag substrate lattice. The absence of any distinct features in the 0.33ML Cr spectrum indicates single layer coverage and offers no indication of any interdiffusion of Cr into the Ag, as has been reported for Cr/Au(001). The 0.5ML curve however, shows significant strengthening of the emission near the  $\theta = 54^\circ$  position, indicative of second-layer growth as proposed by Newstead and co-workers.

At 1.3ML there is strong emission along  $\theta = 0^\circ$ , suggesting that there is significant development of the third Cr layer occurring. With increasing Cr thickness this feature develops rapidly. The feature at  $\theta = 54^\circ$  also develops rapidly with Cr coverage but does not become as intense as the 45° feature in the clean Ag curve; this can be explained by the fact that the interatomic distances involved in each forward scattering process are different with the Cr-Cr 54° distance being longer than the Ag-Ag 45° interatomic distance. As in the clean Ag curve, the features at  $\theta = 20-30^\circ$  in the Cr spectra are due to first order diffraction effects and cannot be solely attributed to forward scattering between Cr atoms.

Figure (4.5) shows polar angle Auger electron intensity distribution curves for both clean Ag(001) and various Cr coverages taken in the [110] azimuth of the Ag(001) substrate. The Auger lines and coverages in the figure are the same as those used in figure (4.4), the only difference between the spectra being that the Ag substrate has been rotated azimuthally by 45°. For the clean Ag(001) curve, intensity peaks are located at  $\theta = 0^\circ$  and  $35^\circ$  as would be expected from forward scattering of electrons between alternate layers of the FCC Ag lattice, along the [001] and [112] axes respectively.

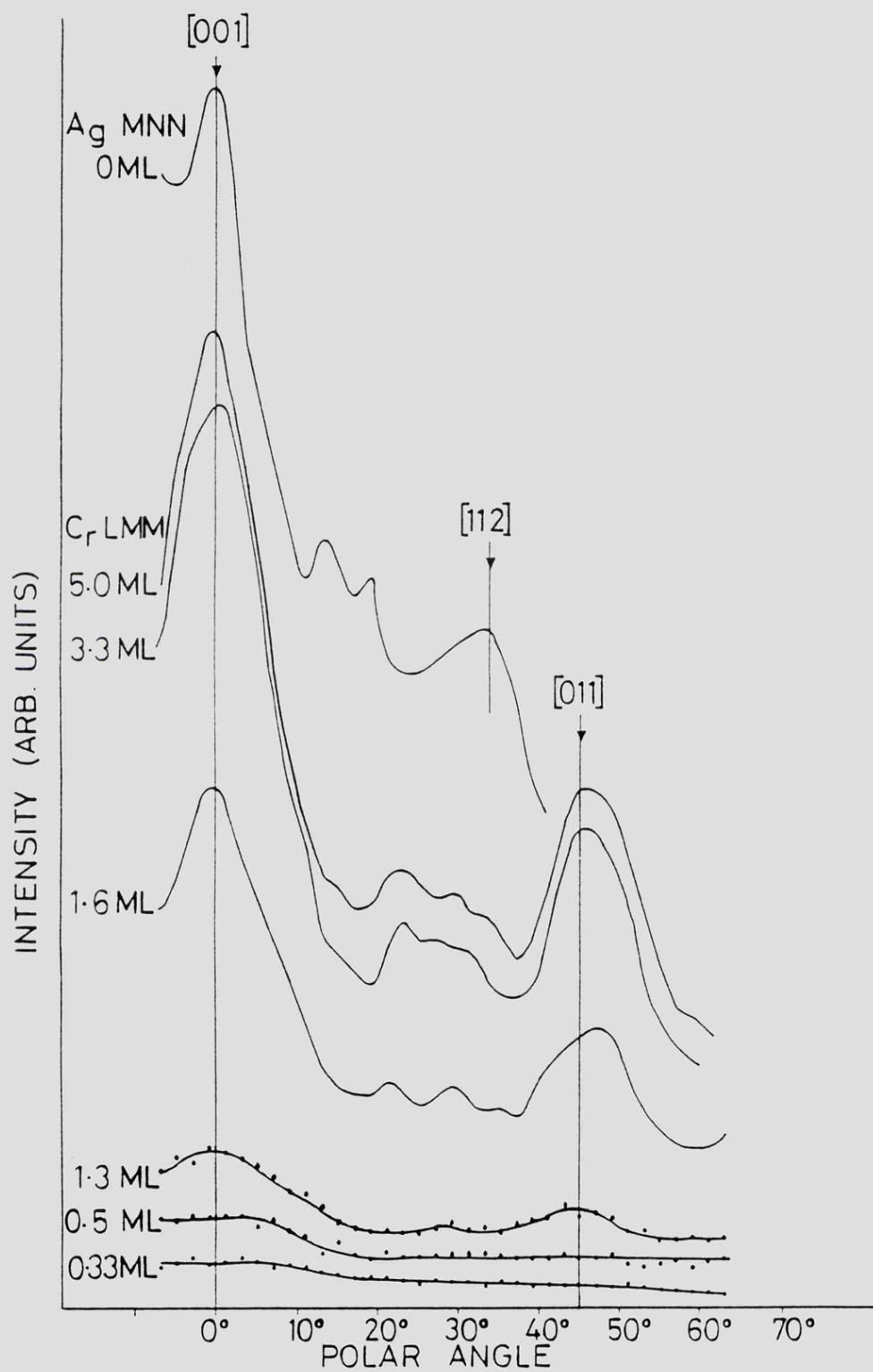


Figure (4.5) Polar angle Auger electron intensity variation for clean Ag(001), and various Cr coverages in the Ag [110] azimuth

As previously, there are first order diffraction and interference features in the curve at  $\theta = 20^\circ$ ; if the Cr overlayer was in the FCC phase, as reported by Durbin et al (1988) for Cr/Au(001), one would expect the Cr curves to replicate that of the clean Ag spectrum. However, as in figure (4.4), this is not the case. For the 5ML Cr curve, peaks are present at  $\theta = 0^\circ$  and  $45^\circ$  corresponding to emission along the [001] and [011] axes of the rotated BCC lattice. The Cr curves for 0.33 and 0.5ML are completely featureless, indicating that there is no formation of a third layer at these coverages, whilst by 1.3ML there is an appearance of features at  $0^\circ$  and  $45^\circ$  indicative of third layer formation at that coverage. These features become more intense with increasing Cr coverage, with the evolution of diffraction features at  $\theta = 20-30^\circ$ .

#### 4.2.4 DISCUSSION

Cr overlayers have been adsorbed onto Ag(001) substrates held at room temperature, with no indication of contamination using either XPS or AES over many hours. Similar As-t and LEED results have been obtained to those achieved by Newstead and co-workers, and so their coverage calibration has been used to describe the thickness of the Cr adlayers. The polar angle Auger electron intensity measurements made on both [100] and [110] azimuths of the Ag(001) substrate indicate that the Cr overlayers are not of the same structure as the FCC substrate.

The measurements on the clean Ag(001) substrate are consistent, in each azimuth, with its bulk FCC structure and in agreement with previous results on FCC crystals. The Cr polar angle curves can only be described in terms of a BCC lattice, which when compared with the clean Ag data, must be rotated by  $45^\circ$  with respect to the Ag FCC lattice as described by Zajac et al (1985) for Cr/Au(001).

The data can be also addressed in terms of the model of Newstead et al, for the growth mechanism of the Cr. The absence of any features in figures (4.4) and (4.5) for Cr coverages of 0.33ML supports the view that the Cr sits on the substrate in single layer platelets at these coverages. Also, this rules out the possibility of interdiffusion of Cr into the substrate as reported for Cr/Au(001) by Hanf et al (1987 & 1989). For the [100] Ag azimuth, the presence of an intensity peak in the 0.5ML Cr curve at  $\theta \approx 54^\circ$  indicates that bilayer formation is taking place and that complete Cr monolayers are not, in fact, occurring. For Cr coverages of 1.3ML and above, peaks at  $\theta = 0^\circ$  indicate forward scattering by alternate Cr layers, and thus show that third Cr layer formation has already occurred. This is in conflict with the findings of Newstead et al who proposed that complete bilayers formed before the creation of a third Cr layer.

By including the fact that the  $p(1 \times 1)$  LEED pattern fades rapidly after 2.0ML, and that the As-t curve curves away after 2.0ML to a saturation value, it can be assumed that above this coverage Cr island formation occurs. Since the polar angle Auger electron data shows that third layer formation is occurring at 1.3ML, it may be possible that island formation is already beginning at that coverage. It is also true that the island formation continues in the BCC phase of Cr as supported by the thicker Cr coverage curves in figures (4.4) and (4.5).

### 4.3 EPITAXIAL GROWTH OF Co ON Ag(001)

#### 4.3.1 INTRODUCTION

Novel structural, electronic and magnetic properties may be induced in ultrathin metal overlayers by such effects as lattice mismatch and strain with the substrate lattice. As a result, Co is of much current interest; in the bulk it orders in the HCP phase and is ferromagnetic

with a magnetic moment of  $1.7\mu_B$  per atom, but above  $425^\circ\text{C}$  Co forms an FCC phase with lattice constant  $3.56\text{\AA}$ .

Previous work with Co overlayers has been largely restricted by the very low vacuum required to produce clean overlayers for long enough to allow experiments to take place. Work by Gonzalez et al (1981) on Co/Cu(001) showed that the Co overlayers grow in the layer-by-layer (Frank-Van Der Merwe) mode in the FCC phase on the substrate held at room temperature. As-t and LEED measurements were made, with the Auger data showing well defined breaks corresponding to the layer by layer growth. According to the LEED, the deposited monolayer was well ordered with the same periodicity as the Cu substrate. Since Cu is FCC with a lattice constant of  $3.61\text{\AA}$ , the FCC phase was proposed with a 2% lateral increase of the Co interatomic distance.

This work has been repeated by Miranda et al (1983), who found good agreement with the results of Gonzalez and co-workers, who also determined the two-dimensional band structure of the Co monolayer using angle resolved photoemission. They were also able to show that the energy position and linewidth of the Cu photoemission features remained unchanged after Co deposition, suggesting weak interaction between the d-bands of the Co and Cu. Further studies of the Co/Cu(001) system have been undertaken by Clarke et al (1987), who made LEED I-V measurements on a single Co monolayer and an 8ML coverage. It was found that the single monolayer had an interlayer spacing contracted by  $6\pm 1\%$  compared with the bulk Cu lattice spacing, with the top substrate layer also contracted by  $6\pm 2\%$ . For the 8ML sample, it was shown that the top Co layer was contracted by  $6\pm 1\%$  with a  $3\pm 2\%$  contraction throughout the rest of the Co film. This behaviour was in agreement with a previous LEED study made on FCC Co(001) by Maglietta and Zannazzi (1978), thus lending much credence

to the argument that the Co is in the FCC phase.

Prinz (1985) has proposed that Co deposited on GaAs(110) grows in a new metastable phase, BCC, that is not present on the known equilibrium phase diagram. This is similar to the growth of Fe/GaAs(110) which has also been shown to grow in the BCC phase (Prinz and Krebs, 1981). The Co layers on GaAs were characterised using RHEED and a lattice constant for the BCC phase of Co obtained by extrapolation of the lattice constant for the BCC phase of the alloy  $\text{Fe}_x\text{Co}_{1-x}$  obtained by Ellis and Greiner (1941). In this way Prinz was able to obtain an estimate for the BCC lattice constant of  $2.819\text{\AA}$ , which is only 0.2% less than that of a  $2 \times 2$  reconstruction upon GaAs(110) with a 1.35% mismatch. More recent work by Idzerda et al (1989) have made comparisons of the conversion-electron X-ray-absorption fine structure of Co grown epitaxially on GaAs(110) with similar measurements made on HCP Co, FCC Cu and BCC Fe. In this way they were able to show unequivocally that the Co deposited on GaAs was indeed BCC with a lattice constant of  $2.82 \pm 0.01\text{\AA}$ , in good agreement with the earlier proposal of Prinz.

As the lattice constant of FCC Co is  $3.56\text{\AA}$ , one would expect that Ni, which has a lattice constant of  $3.52\text{\AA}$ , would provide an ideal for the growth of Co. This has indeed been shown to be the case by Chambers et al (1987). By depositing Co onto Ni(001) held at room temperature, they were able to show that the Co was in the FCC phase by using the same medium energy electron forward scattering technique as used in this chapter. The Co was shown to form bilayer platelets up to two monolayers and then coalesce into a continuous FCC film with no detectable strain up to 30ML.

This section describes a similar experiment carried out on Co/Ag(001), as there is no previous work on this system the growth mode

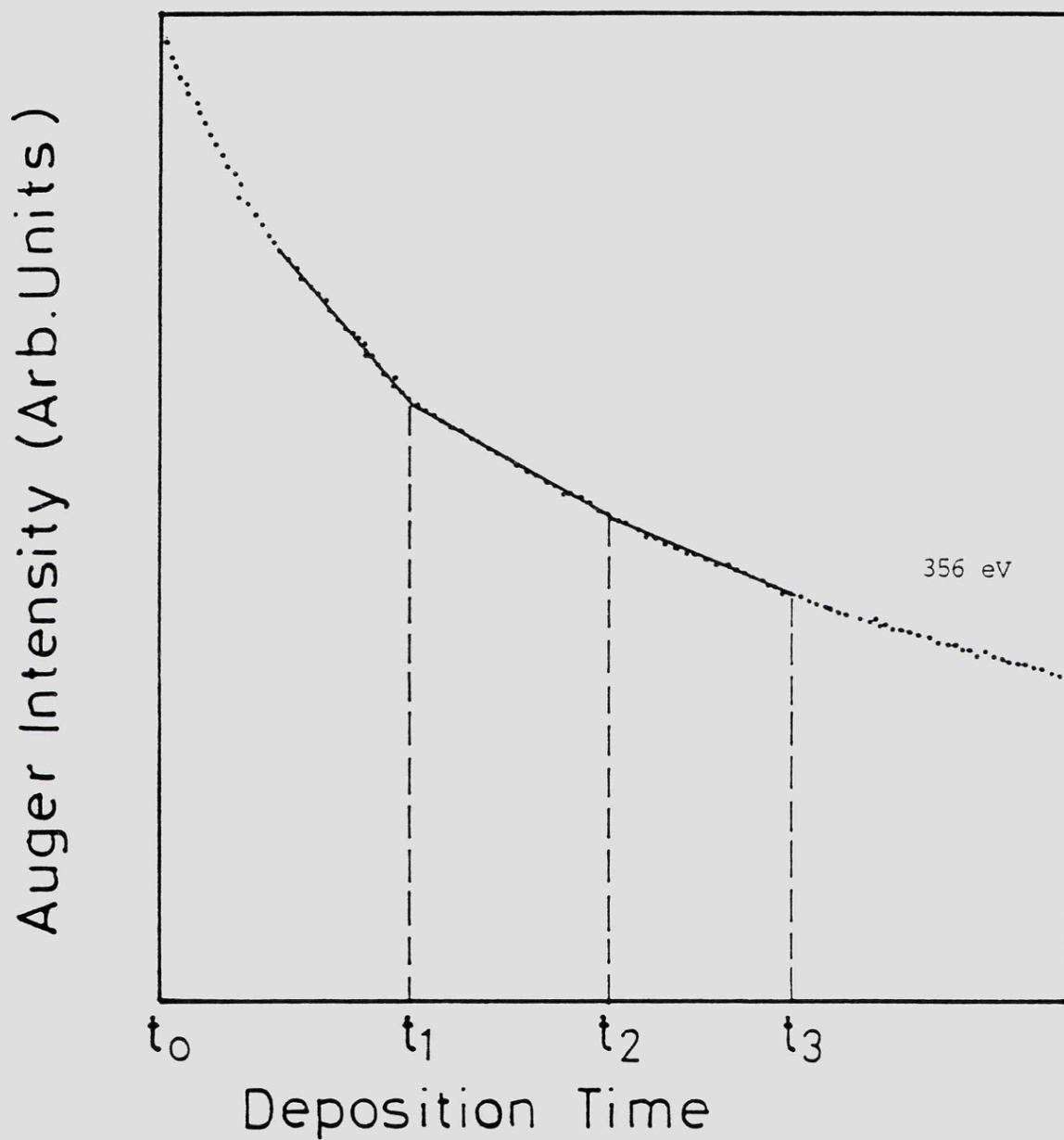


Figure (4.6) As-t plot showing the variation of the Ag MNN (356eV) Auger intensity with Co deposition.  $t_0$  corresponds to the opening of the shutter, and  $t_1$ ,  $t_2$  and  $t_3$  to the completion of each monolayer.

is completely unknown. As the BCC lattice constant for Co has been shown to be  $2.82 \pm 0.01\text{\AA}$ , it was thought that the Co may grow epitaxially on Ag(001) in the BCC phase but with the BCC lattice rotated by  $45^\circ$  relative to the FCC Ag lattice as is the case for Cr/Ag(001) and Fe/Ag(001). This was found not to be the case however, as will be described in the following sections.

#### 4.3.2 LEED AND As-t RESULTS

The Ag substrate was prepared in the fashion described previously, and Co evaporated from a Knudsen cell with the chamber pressure less than  $9 \times 10^{-11}$  Torr during deposition. Growth was monitored by measuring the Ag  $M_{4,5}N_{4,5}N_{4,5}$  (356eV) signal and the resulting As-t plot is shown in figure (4.6).

Reference to the figure shows that after the shutter was opened at  $t_0$  the curve follows an exponential decay until  $I/I_0 = 0.77$  after which the curve forms a series of straight sections interrupted by breaks at  $t_1$ ,  $t_2$  and  $t_3$ . The times between the breaks at  $t_1$  and  $t_2$  and between  $t_2$  and  $t_3$  are approximately equal indicating monolayer growth between each break but the evaporation time between  $t_0$  and  $t_1$  is greater. This means that up until  $t_1$  more than a single monolayer is deposited, assuming one monolayer to mean that all the fourfold sites on the Ag surface are occupied by one Co atom.

LEED showed a sharp  $p(1 \times 1)$  pattern for the clean Ag surface which deteriorated slightly as the Co was deposited until the change in the As-t curve at  $I/I_0 = 0.77$ . It remained as a sharp  $p(1 \times 1)$  pattern until  $t_3$  (3ML), after which it began to fade. However, the LEED pattern was still very clear  $p(1 \times 1)$  even at 6ML which is the highest coverage studied here. The exponential part of the As-t plot at low coverage could be taken to

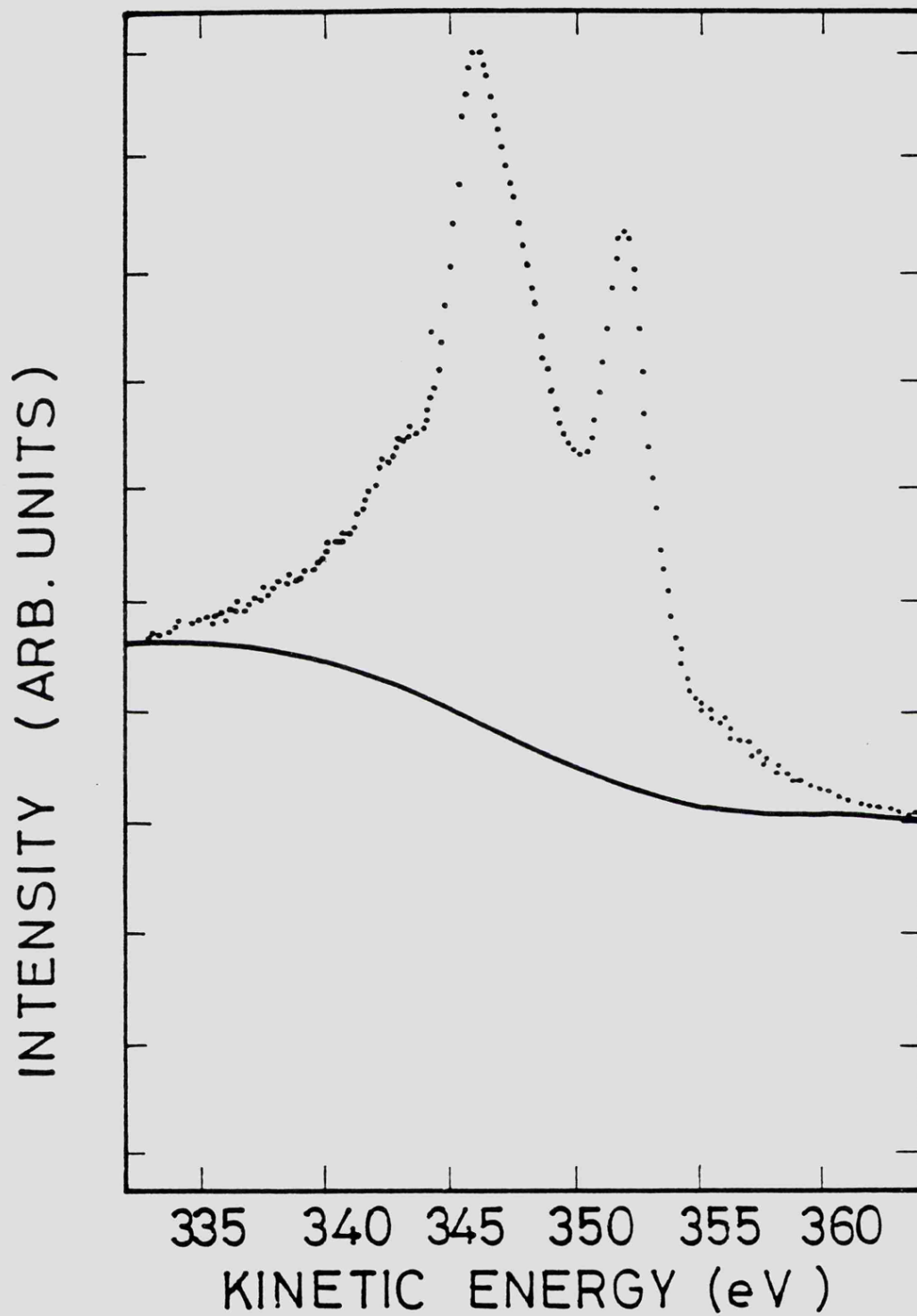


Figure (4.7) Spectrum showing undifferentiated Ag MNN Auger peaks with integral background to be subtracted shown by solid line.

mean simultaneous multilayer growth immediately after opening the shutter. This would not, however, easily explain the breaks that occur later in the curve which tend to suggest layer-by-layer growth. Since the evaporation time to  $t_1$  is just larger than that between  $t_1$  and  $t_2$  and  $t_2$  and  $t_3$ , it is proposed that there is some diffusion of Co into the Ag substrate to form an interfacial alloy structure. Reference to the Ag-Co phase diagram shows no intermixing at all, but interdiffusion of Co into one or two Ag layers may be small enough to have been overlooked. Also it was found when cleaning Co off the Ag substrate, that small traces of Co remained and took four or five  $\text{Ar}^+$  bombardments to remove completely whereas most of the Co could be removed very quickly with one short  $\text{Ar}^+$  sputter.

There is no way of saying which phase the Co arranges itself on Ag(001) using the As-t plot and LEED alone. All that can be said is that the Co does not form a superstructure as the LEED pattern remains sharp  $p(1 \times 1)$  up until 3ML, and fades very slowly above that coverage. It cannot be predicted whether the Co is in the BCC phase with its lattice rotated by  $45^\circ$ , or whether it grows in the FCC phase as a continuation of the Ag bulk lattice. To this end, polar angle electron intensity measurements have been made at various Co coverages to give some indication of the phase of the Co overlayers.

#### 4.3.3 POLAR ANGLE ELECTRON INTENSITY MEASUREMENTS

The choice of electron emission lines to use was easily made; the Ag  $M_{4,5}N_{4,5}N_{4,5}$  (356eV) Auger line was again used as for the Cr/Ag(001) work described earlier as it is the most intense Ag electron emission line of a suitable kinetic energy. The choice of series for the Co overlayers is also straightforward. Using the twin anode laboratory X-ray source would mean measuring the Co  $2p_{1/2}$  and  $2p_{3/2}$  series as they have

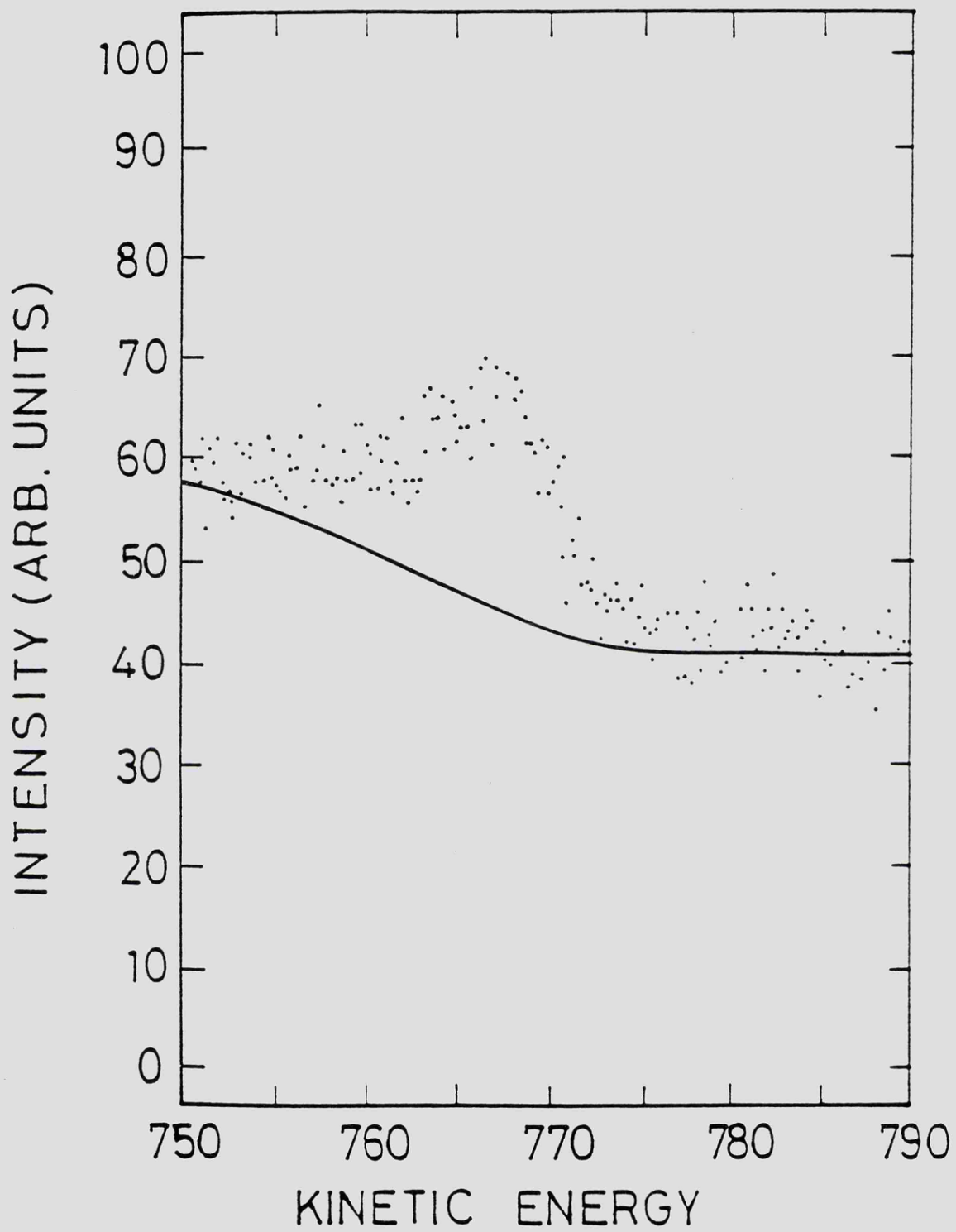


Figure (4.8) Co LMM Auger peak obtained from a 0.5ML Co layer on Ag(001), the solid line is the integral background to be subtracted.

the highest photoionisation cross sections at that photon energy. These emission lines have binding energies of 793.3 and 778.1 eV respectively which do not overlap with any Ag emission lines and thus are usable. It was however decided to use the Co  $L_{2,3}M_{4,5}M_{4,5}$  (775eV) Auger line as it would be much more intense than the Co 2p electrons when excited with an electron beam.

Instead of measuring the peak-to-peak heights of the differentiated Auger lines, as was the case for the Cr data, undifferentiated spectra were taken and the area under each background subtracted peak automatically calculated as described in section 3.2.6. This was done in order to make a more accurate measurement of the emitted electron intensity. Figure (4.7) shows a spectrum showing the Ag  $M_{4,5}N_{4,5}N_{4,5}$  Auger line obtained from clean Ag and the integral background ready to be subtracted. Similarly, figure (4.8) shows the Co  $L_{2,3}M_{4,5}M_{4,5}$  Auger line from a 0.5ML thick layer on the Ag(001) with its integral background.

Figure (4.9) shows polar angle Auger electron intensity scans for clean Ag and various coverages of Co up to 6ML in the [100] azimuth of the Ag substrate. The vertical scale is normalised,  $100(I_{\max} - I)/I_{\max}$ , so that even though the absolute intensities are small, the variation with polar angle  $\theta$  is large. For the clean Ag scan, dominant peaks are found at  $\theta = 0^\circ$  and  $45^\circ$  with respect to the surface normal, as expected from forward scattering of electrons by layers of the FCC lattice along the [001] and [101] axes, and in agreement with the clean Ag scan in figure (4.4). As before, the feature at  $\theta = 20-30^\circ$  cannot be assumed to be totally due to forward scattering and can be ignored.

The 6ML Co spectrum closely resembles the clean Ag peak with peaks at  $0^\circ$  and  $45^\circ$ , with another feature at  $20-30^\circ$ . If the Co was growing in

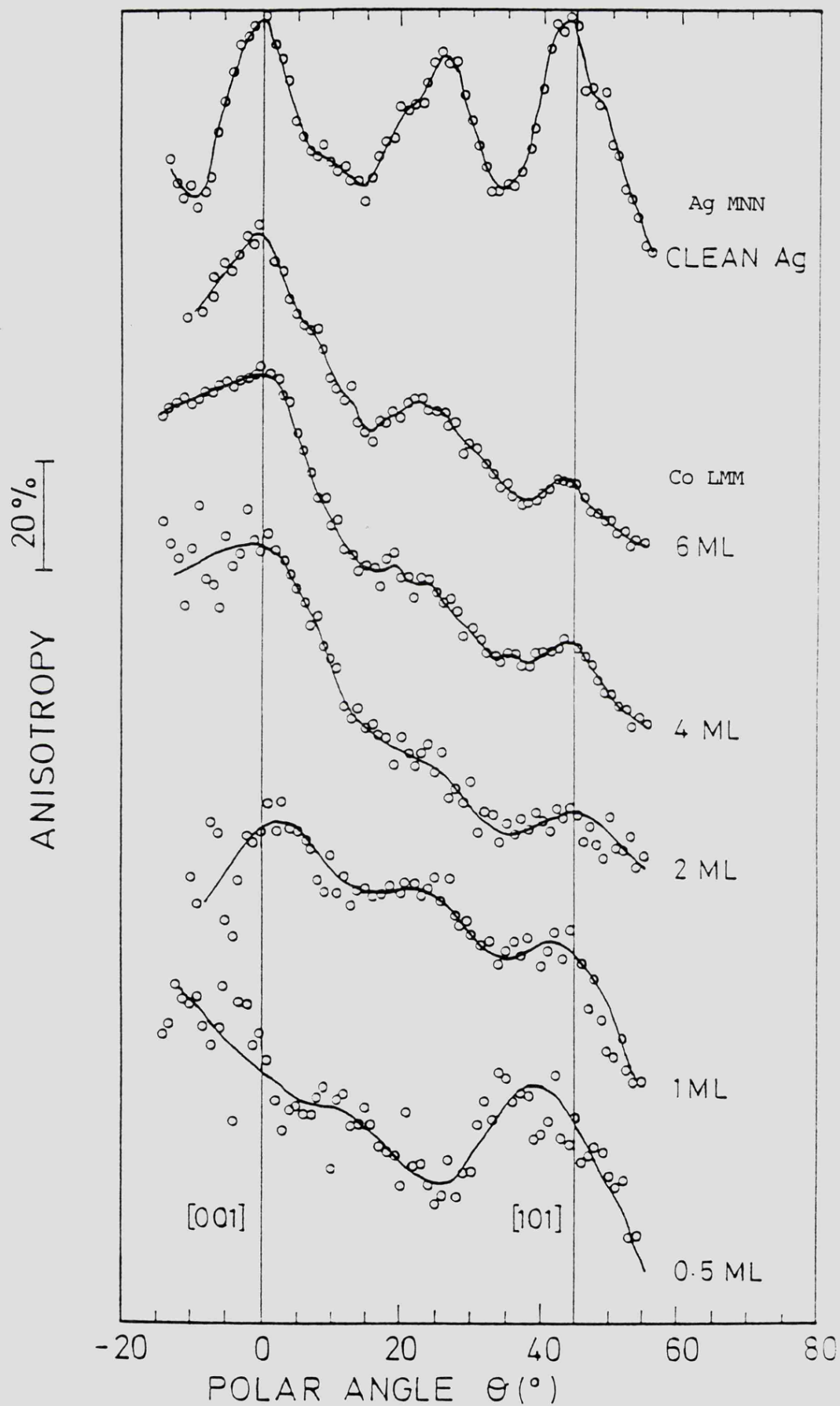


Figure (4.9) Polar angle Auger electron intensity variation for clean Ag(001) and with various Co coverages in the [100] Ag azimuth.

the BCC phase with its lattice rotated by  $45^\circ$  with respect to the Ag lattice, one would expect similar behaviour as for Cr in figure (4.4). That is, no feature at  $45^\circ$  with a weaker feature at  $54^\circ$  (the scans were found to be featureless above  $45^\circ$ , and so the scans shown in the figure were only taken as far as  $45^\circ$  to reduce the possibility of contamination). This suggests that the Co is indeed in the FCC phase and not BCC. The 0.5ML curve has one large feature near  $45^\circ$ , indicating that there is some second layer growth occurring but no third layer. This could also be explained in terms of Co atoms diffusing into the bulk with forward scattering by overlying Ag atoms, as indicated by the As-t plot.

The 1ML scan has a second feature at  $\theta = 0^\circ$ , due to forward scattering along the [001] axis, again including Co atoms that have diffused into the substrate. The features at  $0^\circ$  and  $45^\circ$  then develop rapidly with Co coverage, and there is also another feature at  $20-30^\circ$  due to first order diffraction and interference.

Figure (4.10) shows polar angle Auger electron intensity spectra for clean Ag and various Co coverages in the [110] Ag surface azimuth. As in figure (4.5) the clean Ag spectrum shows peaks at  $\theta = 0^\circ$  and  $35^\circ$  due to forward scattering by alternate Ag layers along the [001] and [112] axes of the FCC lattice. Again the 6ML Co curve closely resembles the clean Ag spectrum, with dominant peaks at  $0^\circ$  and  $35^\circ$ , indicating FCC growth. The 0.5ML scan is completely featureless, as would be expected if no third layer of Co existed and this would agree with the 0.5ML curve in figure (4.9) which shows only a feature at  $45^\circ$ . The 1ML scan is also featureless however, in contrast to the 1ML scan from the [100] azimuth which indicates third layer growth. By 2ML the  $35^\circ$  peak has appeared in the Co curve indicating third layer growth, but the apparent absence of a feature at  $0^\circ$  contradicts this. This absence of the  $0^\circ$  peak may just be

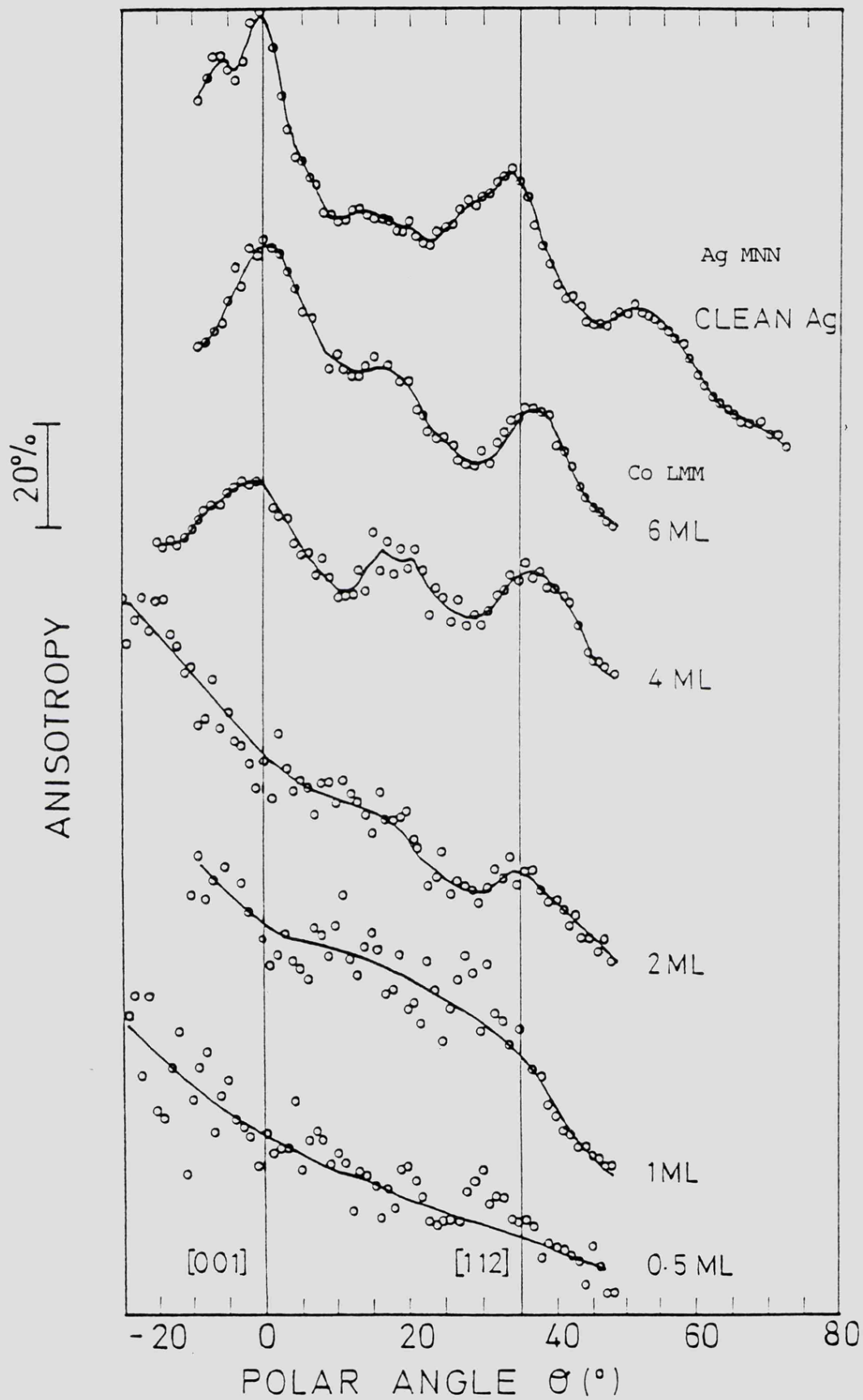


Figure (4.10) Polar angle Auger electron intensity variation for clean Ag(001) and with various Co coverages in the Ag [110] azimuth.

due to the large scatter in the data points, or possibly to a misalignment of the sample or incident electron beam during the scan. However the peak at  $35^\circ$  is clearly real, giving strong evidence of third layer formation at that coverage. By 4ML, both peaks at  $0^\circ$  and  $35^\circ$  have appeared and with increasing thickness develop rapidly. The feature at  $20^\circ$  again cannot be explained solely by forward scattering and is due to first order diffraction and interference effects.

#### 4.3.4 DISCUSSION

The As-t and LEED data indicate that at low coverages ( $< 0.5\text{ML}$ ) there is some interdiffusion of the Co into the Ag substrate, but that this quickly stops and is followed by a layer-by-layer growth mode up to 3ML. The sharp  $p(1 \times 1)$  LEED pattern remained until the third monolayer, after which it slowly fades but was still clearly visible at 6ML, the thickest coverage studied.

The phase of the Co overlayers has been resolved by the polar angle Auger electron intensity scans. The similarity of the clean Ag and Co polar angle spectra can only mean that the Co grows in the FCC phase. This is in contradiction with the growth mode of other transition metals on the Ag(001) surface such as Fe and Cr and could suggest a large lateral strain of 14%. The argument that the Co diffuses into the first two layers of the Ag substrate at low coverages is supported by the 0.5ML Co polar angle scans. The [100] azimuth scan has a single peak near  $45^\circ$ , indicating diffusion of no more than two layers into the Ag, and the [110] azimuth scan is featureless indicating no third layer forward scattering.

At 1ML, the [100] scan shows a further peak at  $0^\circ$  has appeared indicating third layer formation, but the [110] azimuth scan at 1ML is

again featureless indicating no third layer formation. This may be explained by the fact that the amount of interdiffusion may vary with different depositions and may depend on the initial state of the Ag surface before deposition. Therefore the number of apparent layers seen in the polar angle electron intensity scans may change from scan to scan as has been seen here. The peaks in both azimuths then rapidly strengthen with Co coverage and at 6ML closely resemble the clean Ag(001) scans indicating FCC growth as previously explained. There is no way of estimating the lattice constant of the FCC Co but there are two possibilities; the interdiffusion of the Co into the top few layers of the Ag may cause some relaxation of the Ag(001) surface with the growth of FCC Co with a lattice constant close to the bulk FCC Co value of 3.56Å. Conversely, the Co FCC lattice may be expanded by 14% so that its lattice constant closely matches the Ag bulk value of 4.09Å. In this case one would expect the Co lattice to be compressed in the vertical direction due to the large lateral stress in the plane of the surface. Chambers et al (1986) have shown that by measuring the relative shifts of forward scattered electron intensity peaks with the surface normal, the elastic strain and surface relaxation of Cu/Ni(001) could be measured.

The position of the 0° peaks in both azimuths will remain fixed in  $\theta$  even if there were any vertical compression of the Co lattice. However by measuring shifts of the 45° peak in the [100] azimuth and the 35° in the [110] azimuth, it may be possible to measure any compression. Reference to figure (4.9) shows that the 45° Co peak does not seem shifted to higher  $\theta$  relative to the 0° peak, as would be expected for vertical compression. The Co 35° peak in figure (4.10) however does seem to be shifted to higher  $\theta$  by  $2^\circ \pm 1^\circ$ . Assuming that the in-plane lattice constant was the same as that of bulk Ag (4.09Å), an estimate can be made of the compressed vertical Co lattice spacing to be  $3.84 \pm 0.14$ Å. The lack

of any noticeable shift in the 45° peak in the [100] azimuth scan could be attributed to the fact that the peak is due to forward scattering by successive Co layers, whereas the 35° peak in the [110] azimuth curves is due to forward scattering from alternate Co layers. Therefore any shift in the 45° peak would be much smaller than the shift in the 35° peak and may be more difficult to measure. More accurate scans over both the 0° peaks and the 45° and 35° peaks need to be made before any accurate estimate of the compressive strain, if any, can be measured.

#### 4.4 SUMMARY

LEED, As-t and polar angle Auger electron intensity measurements have been made on both Cr/Ag(001) and Co/Ag(001). The As-t and LEED measurements made on Cr/Ag are in fairly good agreement with the results of Newstead and co-workers on the same system. Subsequently, it was decided to use the coverage calibration of Newstead et al, such that the first break in the As-t plot corresponds to 0.33ML, with further coverages being made as multiples of the evaporation time to 0.33ML.

Polar angle electron intensity measurements made on the Cr/Ag system have indeed shown that the Cr overlayers arrange in the BCC phase as proposed for Cr/Au(001) and Cr/Ag(001). Study of the polar angle curves for the first few monolayers of Cr growth indicate that up to 0.33ML the growth proceeds as single layer platelets followed by bilayer platelets up to at least 0.5ML. By 1.3ML, third layer growth has occurred, in contrast to the model of Newstead et al who predicted formation of a complete bilayer before island growth. The results are consistent with the basic picture of epitaxial growth described by Newstead and co-workers although there is some development of the third layer before the second is complete.

As-t and LEED results from the Co/Ag(001) system indicate that layer-by-layer growth occurs up to 3ML with some interdiffusion of Co into the Ag substrate below 0.5ML. Above 3ML, the p(1x1) LEED pattern slowly fades, indicating disordering of the overlayer, but a the LEED pattern can still be clearly seen even at 6ML. In order to study the structure of the Co overlayers, polar angle electron intensity measurements have been made in the [100] and [110] azimuths of the Ag(001) substrate. In contrast to the Cr/Ag results, the Co orders in the FCC phase at least up to 6ML. Low Co coverage polar scans support the view that interdiffusion occurs at such coverages, with no more than two layer interdiffusion seen. Differences in the scans for each azimuth suggest that the amount of interdiffusion is not even and may depend on the initial Ag surface quality. It is not possible to say whether the interdiffusion causes a relaxation of the topmost Ag layers with subsequent growth of bulk-like FCC Co, or if the Co FCC lattice is expanded to match the Ag substrate. The second growth mechanism may be supported by the fact that there appears to be some shift of the Co 35° peak in the [110] scans to higher  $\theta$ , suggesting vertical compression of the Co lattice.

## CHAPTER 5

### POLARISED NEUTRON REFLECTION STUDIES OF THE MAGNETIC ORDERING OF Ag/Cr/Ag(001) AND Ag/Fe/Ag(001) SANDWICH STRUCTURES

- 5.1 Introduction
  
- 5.2 Magnetic Ordering Of Cr in Ag/Cr/Ag(001) Structures
  - 5.2.1 Introduction
  - 5.2.2 PNR Results
  - 5.2.3 Discussion
  
- 5.3 Magnetic Ordering Of Fe In An Ag/Fe/Ag(001) Structure
  - 5.3.1 Introduction
  - 5.3.2 Results
  - 5.3.3 Discussion
  
- 5.4 Summary

## CHAPTER 5

### POLARISED NEUTRON REFLECTION STUDIES OF THE MAGNETIC ORDERING OF Ag/Cr/Ag(001) AND Ag/Fe/Ag(001) SANDWICH STRUCTURES

#### 5.1 INTRODUCTION

Ultrathin epitaxial metallic films have recently received much attention because of the striking departure of their magnetic properties from those of bulk materials. Moreover new phases of materials such as FCC Fe and Co, which can be grown epitaxially on Cu(001), can be studied and have been shown to have unique magnetic properties (for example, Liu et al, 1988).

The proposal of enhanced ferromagnetic moments in monolayers of 3d transition metal monolayers adsorbed onto noble metal substrates (Fu et al, 1985 and Blügel et al, 1988) has stimulated much experimental study of such structures. Techniques such as angle-resolved and spin-polarised photoemission, spin polarised LEED, Kerr effect measurements and Mössbauer spectroscopy have all become widely used in the study of epitaxial thin films. The accurate measurement of magnetic moments of such films remains difficult. Rough estimates can be made using photoelectron spectroscopy but there is some dispute as to the quantitative reliability of the technique.

Polarised neutron reflection provides a direct means of determining the absolute value of the magnetic moment per atom of ultrathin metallic sandwich structures (Bland et al, 1987). By measuring the specularly reflected neutron beam close to the critical angle for total external reflection it is possible to overcome the large penetration depth of neutrons into matter and enhance surface sensitivity.

This chapter describes polarised neutron reflection measurements made on sandwich structures composed of ultrathin layers of Cr and Fe adsorbed onto Ag(001) with thick overlayers of Ag deposited on top. Fe is characteristic of the 3d ferromagnetic transition metal series displaying a localised moment but has been predicted theoretically to have an enhanced magnetic moment when adsorbed on noble metal substrates. Cr has been predicted to have a ferromagnetic surface layer on its (001) face with a greatly enhanced moment, and like Fe has also been predicted to having giant ferromagnetic moments when adsorbed onto Au. The PNR studies in the following chapter attempt to show the magnetic ordering of such structures and make an estimate of the magnitude of any ferromagnetic moments.

## 5.2 MAGNETIC ORDERING OF Cr IN Ag/Cr/Ag(001) STRUCTURES

### 5.2.1 INTRODUCTION

The possibility of ferromagnetism occurring at the surface of a bulk antiferromagnet or paramagnet has attracted attention since it represents an extreme case of the influence of the surface (Fu et al, 1985). Cr is of particular interest in view of its half-filled 3d electron shell and because, in its bulk BCC phase, it is an itinerant antiferromagnet with a small magnetic moment per atom of  $0.59\mu_B$  (Bacon, 1961 and Shirane and Takei, 1962). The antiferromagnetic ordering in the ground state results from an incommensurate spin-density wave along the [001] direction (Fawcett, 1988).

The possibility of ferromagnetism occurring at the surface of antiferromagnetic crystals was first considered by Pendrey and Gurman (1975) and Teraoka and Kajamori (1977). Experimental verification of this was achieved on Cr(001) by Ferguson (1978) by detecting surface

magnetoplasma waves via a method of attenuated total reflection. Angle resolved photoelectron spectroscopy measurements by Klebanoff et al (1984) further confirmed the theoretical predictions of surface ferromagnetism on the Cr(001) surface and estimated the ferromagnetic moment to be  $2.4 \pm 0.3\mu_B$ .

Self consistent all-electron local spin density functional calculations by Fu and Freeman (1986) on the electronic structure of a seven layer Cr(001) film predicted ferromagnetic ordering on the surface with an enhanced magnetic moment per Cr atom of  $2.4\mu_B$ , in agreement with the result of Klebanoff et al. This behaviour was attributed to the sharp surface density-of-states peak near the Fermi level for the paramagnetic state producing a large enhancement of the local spin susceptibility.

More recently, self consistent total energy calculations on the Cr(001) surface by Blügel et al (1989) showed that ferromagnetism is energetically more favourable than the c(2x2) antiferromagnetic ordering. In order to explain spin resolved photoemission results by Meier et al (1982), in which no surface magnetisation was found, and the results of Klebanoff et al (1984), Blügel et al proposed that the Cr surface was made up of a series of ferromagnetic terraces antiferromagnetically coupled to each other via single layer steps, and showed that a clean Cr surface gave a p(1x1) LEED pattern and not c(2x2) as had previously been claimed. Spin polarised LEED measurements made by Carbonne and Alvarado (1987) on the Cr(001) surface also failed to detect the presence of any magnetisation in the first few layers.

Further calculations using a full-potential linearised augmented plane-wave (FLAPW) approach by Fu et al (1985) predicted large magnetic moments for several ultrathin metallic layers supported on single crystal

substrates. Table (5.1) gives the calculated layer-by-layer magnetic moments (in Bohr magnetons,  $\mu_B$ ) and spin-polarisation energy (in eV) proposed by Fu et al. Reference to the table shows that for a Cr monolayer deposited on Au(001) a ferromagnetic layer is predicted with a greatly enhanced moment of  $3.7\mu_B$  per atom, confirming the general view that reducing the atomic coordination causes a 'Stoner' enhancement of the magnetic moment. Furthermore, table (5.1) shows that the magnetic moment is only slightly reduced to  $3.1\mu_B$  when the layer is sandwiched in a Au/Cr/Au(001) structure. This result was related to a narrowing of the d band due to the reduced coordination number and lower symmetry of the monolayer, relative to the bulk. This behaviour contrasts with earlier work by Brodsky et al (1982) that reported superconducting Au/Cr/Au sandwich structures with the Cr layers in the FCC phase.

In contrast to their earlier work, further calculations by Freeman and Fu (1987) suggested that in-plane antiferromagnetism was energetically more favourable than in-plane ferromagnetism for a monolayer of Cr adsorbed on Au(001) but again with a strongly enhanced magnetic moment per atom of  $3.48\mu_B$ , as occurs for the Cr(001) surface. In their study of the growth of Cr layers on Ag(001), Newstead et al made photoemission measurements as a function of Cr coverage. By measuring the Cr 3s multiplet splitting they were able to estimate the magnetic moment per atom of the Cr layers. In this way it was predicted that at 0.06ML, there was an enhanced moment of  $4\mu_B$ /atom, but that it rapidly decreased to the bulk value at 1ML, and the moment of the single layer platelets at 0.33ML was  $1.5\mu_B$ , much less than that reported theoretically by Freeman and Fu. Moreover, no conclusions could be made about the magnetic ordering of the Cr layers.

Blügel et al (1988) have made calculations considering the whole of

	Cr	Nearest Au	$E(\text{para.})$ $- E(\text{spin-pol.})$
Cr monolayer	4.12	...	1.69
1 Cr/Au(001) overlayer	3.70	0.14	0.78
2 Cr/Au(001)	2.90 (S), -2.30 (S-1)	-0.08	0.60
Au/Cr/Au(001) sandwich	3.10	0.14 (S), 0.13(S-2)	0.38
(1x1) Au/Cr CMS	2.95	0.10	0.25
	Fe	Nearest Cu, Ag, Au	
Fe monolayer	3.20	...	1.34
1 Fe/Cu(001)	2.85	0.04	0.70
1 Fe/Ag(001)	2.96	0	1.14
2 Fe/Ag(001)	2.94 (S), 2.63 (S-1)	0.05	1.15
Ag/Fe/Ag	2.80	0	0.38
Au/Fe/Au	2.92	0.08	0.97
	V	Nearest Ag, Au	
1 V/Au(001)	1.75	0.04	0.10
1 V/Ag(001)	1.98	0.06	0.14
2 V/Ag(001)	1.15 (S), < 0.05 (S-1)	0	0.08
Ag/V/Ag	0	0	...
Cr/Fe/Au(001)	3.10 (Cr), -1.90 (Fe)	-0.04 (Au)	0.68
Fe/Cr/Ag(001)	2.30 (Fe), -2.40 (Cr)	-0.09 (Ag)	0.52

Table (5.1) Calculated layer magnetic moments in  $\mu_B$  by Fu et al (1985); S and S-n indicate surface and subsurface layers.

the transition metal series as overlayers on Pd(001) using full-potential linearised augmented-plane-wave (FLAPW) approach. They concluded that Fe, Co and Ni overlayers favoured the p(1x1) ferromagnetic configuration whilst V, Cr and Mn favoured the c(2x2) antiferromagnetic superstructure. In addition, it was postulated that this result could be a general one that could also be found on the (001) surfaces of Pt and the noble metals Ag, Au and Cu.

Presented here are polarised neutron reflection (PNR) measurements of Ag/Cr/Ag(001) structures for three different Cr coverages. Cr has already been shown to be epitaxial on Ag(001), growing in its bulk BCC phase (Johnson et al, 1988). PNR can show if the magnetic layers are indeed ferromagnetic or not and can also give an accurate measurement of the ferromagnetic moment per atom of that magnetic layer (see chapter 2 of this thesis).

### 5.2.2 PNR RESULTS

In order to study the magnetic behaviour of Cr layers adsorbed on Ag, three coverages were considered. Firstly, Newstead et al have shown that Cr grows in single layer platelets on Ag up to 0.33ML. Therefore 0.33ML of Cr was chosen as a coverage to be studied as it is the highest coverage of Cr that is made up of a single atomic layer. Secondly, Newstead and co-workers proposed that Cr completed a complete bilayer on the Ag substrate before continuing its growth in the formation of islands. Reference to chapter 4 of this thesis shows that third layer formation of Cr does actually occur at 1.3ML, but at the time of the choice of Cr coverages to be studied with PNR it was still assumed that the Cr completed a bilayer and so the 2.0ML coverage was chosen as it was assumed to correspond to a perfect double layer of Cr. Finally, 3.3ML of Cr was chosen as a nominal thicker layer to study as it corresponded to

the bulk Cr moment, as proposed by Newstead and co-workers with their electron spectroscopy study.

Two separate 0.33ML samples were prepared in exactly the same way and PNR measurements were carried out on each, as well as the single samples of 2.0 and 3.3ML. The samples were prepared in the UHV system described in section 3.2.1 of this thesis, the chamber pressure remaining at less than  $1 \times 10^{-10}$  Torr during deposition. The low chamber pressure is extremely important as it has previously been demonstrated that small amounts of N, C and O can significantly influence the surface magnetic behaviour (Meier et al, 1982 and Blügel et al, 1988). After deposition of the Cr layers, a thick Ag overlayer of 200Å was deposited as described in section 3.3.2 of this thesis.

By measuring the spin dependent neutron reflectivity from each sample, a flipping ratio  $F(q)$  curve was produced versus reduced wavevector  $q/q_c$ . The incident polarisation was determined to be 84% by using a Co-Ti supermirror in the sample position and all the spin dependent reflectivity data was corrected for this partial polarisation using:-

$$P^* = \frac{(F - 1)}{(F + 1)} \cdot \frac{(R + 1)}{(R - 1)} = \frac{(F' - 1)}{(F' + 1)} \quad - (5.1)$$

Where  $F$  is the measured flipping ratio from the sample,  $R$  is the measured flipping ratio from the Co-Ti supermirror, and  $F'$  is the polarisation corrected flipping ratio. Depolarisation of the reflected beam emergent from the sample cell is unimportant since only the reflected intensity is measured and polarisation analysis of the reflected beam is not performed.

The magnetic field applied in the plane of the Cr layers was 8300e

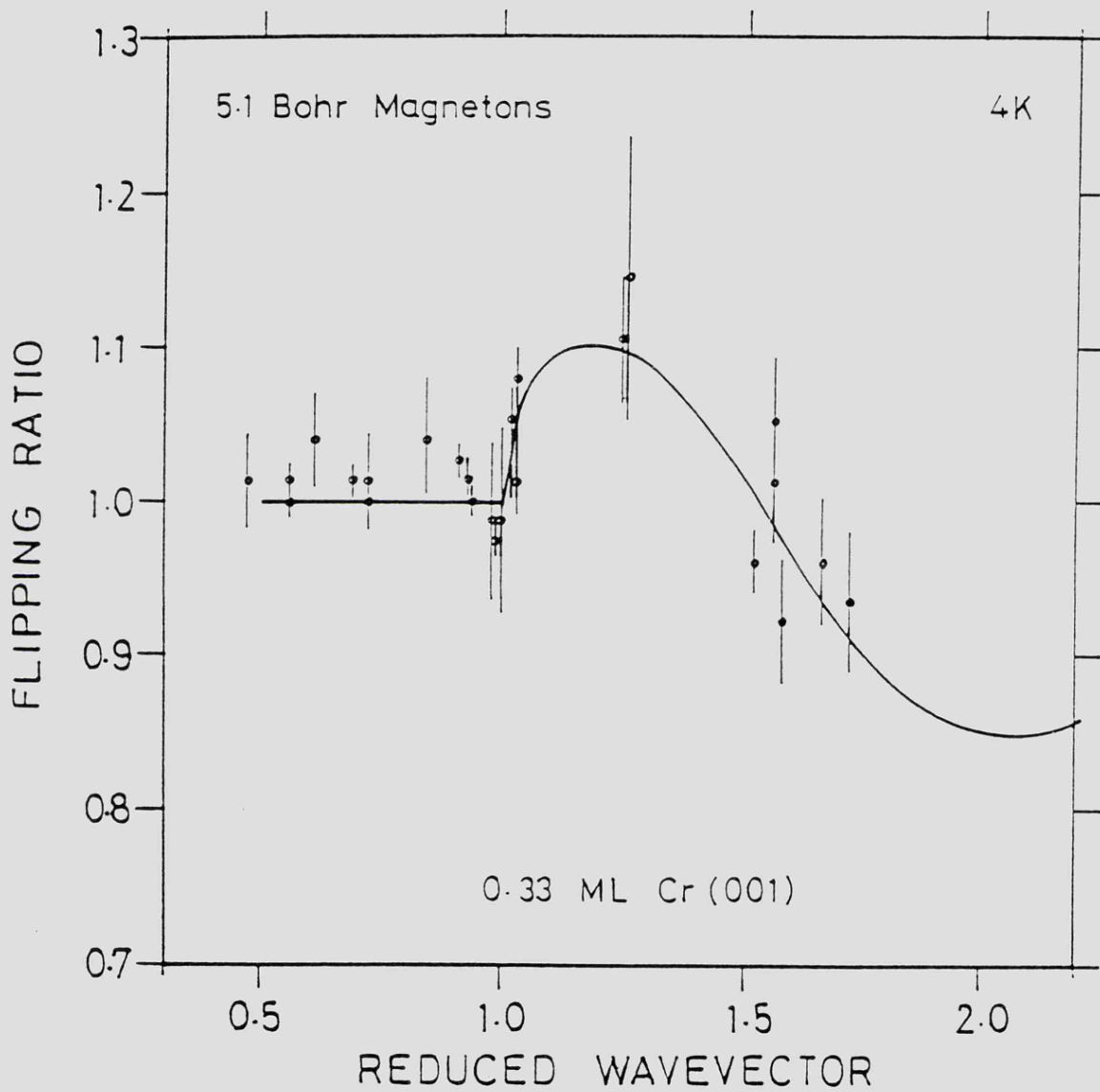


Figure (5.1) Variation in flipping ratio  $F(q)$  with the reduced wavevector for the 0.33ML Cr samples. The solid line is a prediction for a ferromagnetic layer with magnetic moment  $5.1\mu_B/\text{atom}$ .

using Sm-Co magnets. All measurements were carried out at 4K to ensure that all results obtained would be below any possible Curie temperature for the system.

Figure (5.1) shows the variation of flipping ratio  $F(q)$  with reduced wavevector  $q/q_c$  for the 0.33ML samples. The data points include results from both samples of the same thickness that were taken on two separate occasions. It can be seen that there is significant deviation of  $F(q)$  from unity above  $q/q_c=1.0$ , with a peak occurring in the vicinity of  $1.3q/q_c$ . The position of the peak is determined principally by the thickness of the Ag overlayer and is consistent to within 10% of the value of 200Å determined experimentally during the growth of the sandwich structure.

The statistical uncertainty in the data is due to the finite counting time used for each point, (typically 1hr at  $1.5q_c$ ). The solid line through the data shows the calculated response of the flipping ratio with a thickness of 200Å for the Ag overlayer, 1.44Å for the Cr thickness (with the number of Cr atoms per unit area 1/3 of the number of Ag atoms per unit area), and with a magnetic moment of  $5.1\mu_B$ /atom in the Cr layer. Thus the data shows that the buried Cr layer may well be ferromagnetically ordered in the plane of the surface, in agreement with the original calculation of Fu and Freeman (1986) but in contradiction to more recent theoretical studies by Freeman and Fu (1987) and Blügel et al (1988).

The flipping ratio observed for the 2.0ML Cr layer thickness is shown in figure (5.2). There is no significant departure from unity of  $F(q)$  through the whole range of  $q$ , indicating the absence of any in-plane ferromagnetic ordering. The large scatter of the data points is a result

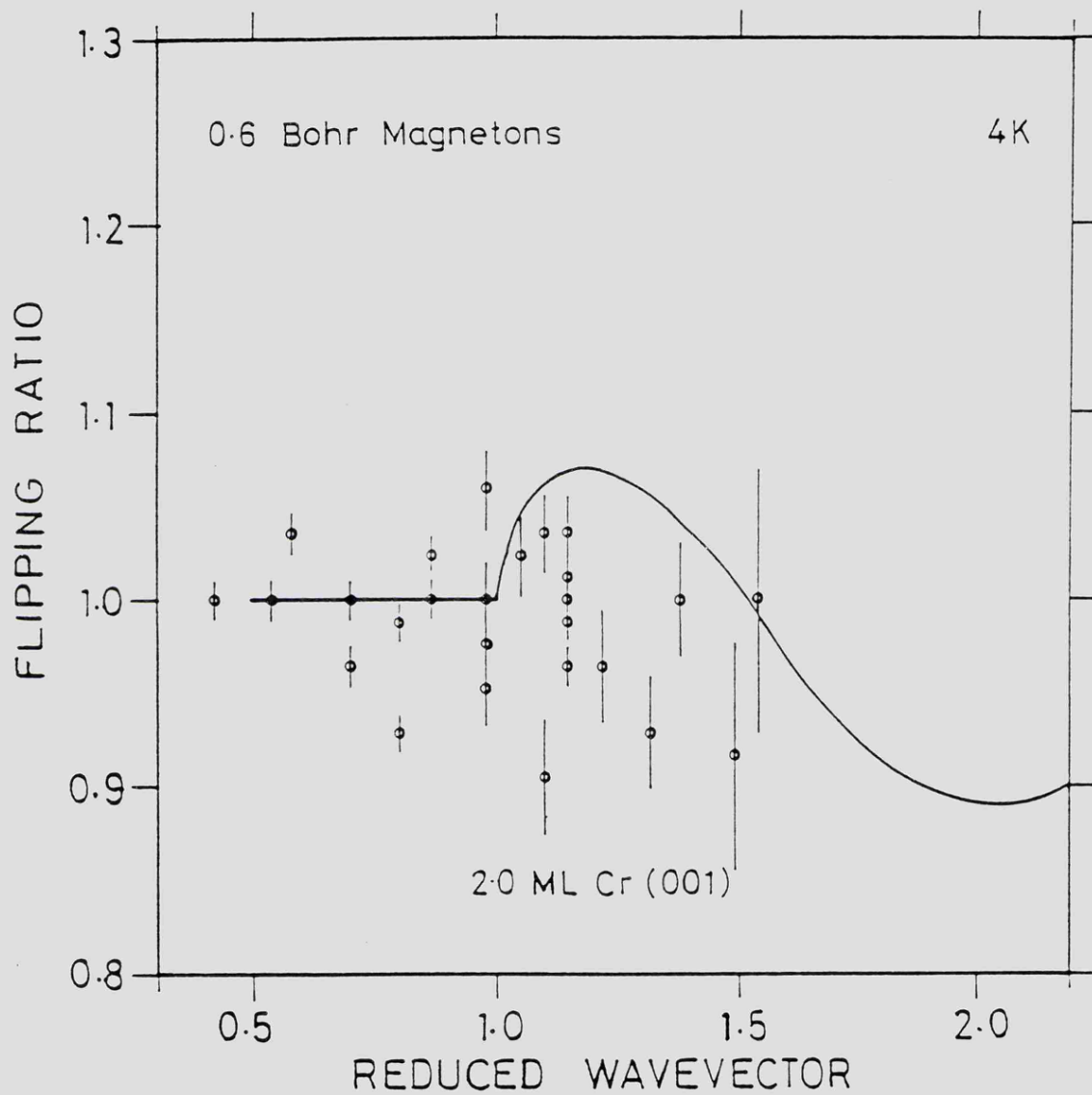


Figure (5.2) Variation in flipping ratio  $F(q)$  with the reduced wavevector for the 2.0ML Cr sample. The solid line is a prediction for a ferromagnetic layer with magnetic moment  $0.6\mu_B/\text{atom}$ .

of a rapid drop in the reflected intensity above  $q_c$ , attributed to a long-range roughness of the sample which could not be detected during sample preparation with LEED because of the short coherence lengthscales inherent with that technique. The solid line through the plot is the calculated flipping ratio expected from a 2ML thick Cr layer with a ferromagnetic moment of  $0.6\mu_B$ , the bulk moment of BCC Cr. As previously described, the data could in no way be said to fit the theoretical curve, indicating the absence of ferromagnetic ordering.

Figure (5.3) shows the variation in flipping ratio with  $q$  obtained for the 3.3ML thick Cr layer sample. As with the 2.0ML data, there is no significant deviance of  $F(q)$  from unity over the whole range of  $q$ , consistent with the absence of any in-plane ferromagnetism. The solid line is again the theoretical response of a ferromagnetic Cr layer of  $4.80\text{\AA}$  thickness and magnetic moment of  $0.6\mu_B$  covered with a Ag layer of  $200\text{\AA}$  thickness. Thus it is proposed that there is no in-plane ferromagnetic ordering for either the 2.0ML or the 3.3ML Cr samples.

### 5.2.3 DISCUSSION

An interesting comparison can be made of the data to the theoretical calculations of Fu and Freeman (1986), and also Hirashita et al (1981). Both studies are calculations of layer dependent magnetic moments per atom of Cr(001), Fu and Freeman taking a 7 layer slab and Hirashita et al a 5 layer slab. In both cases, the calculations show that for an odd number of layers, the outermost layers have substantially enhanced parallel magnetic moments,  $2.49\mu_B$  for the 7 layer slab and  $2.57\mu_B$  for the 5 layer slab. Each layer is proposed to be ferromagnetic in-plane with adjacent layers coupling antiferromagnetically. Each central layer has a magnetic moment close to the bulk value for Cr, with the 5 layer slab having its central layer moment parallel to the moments

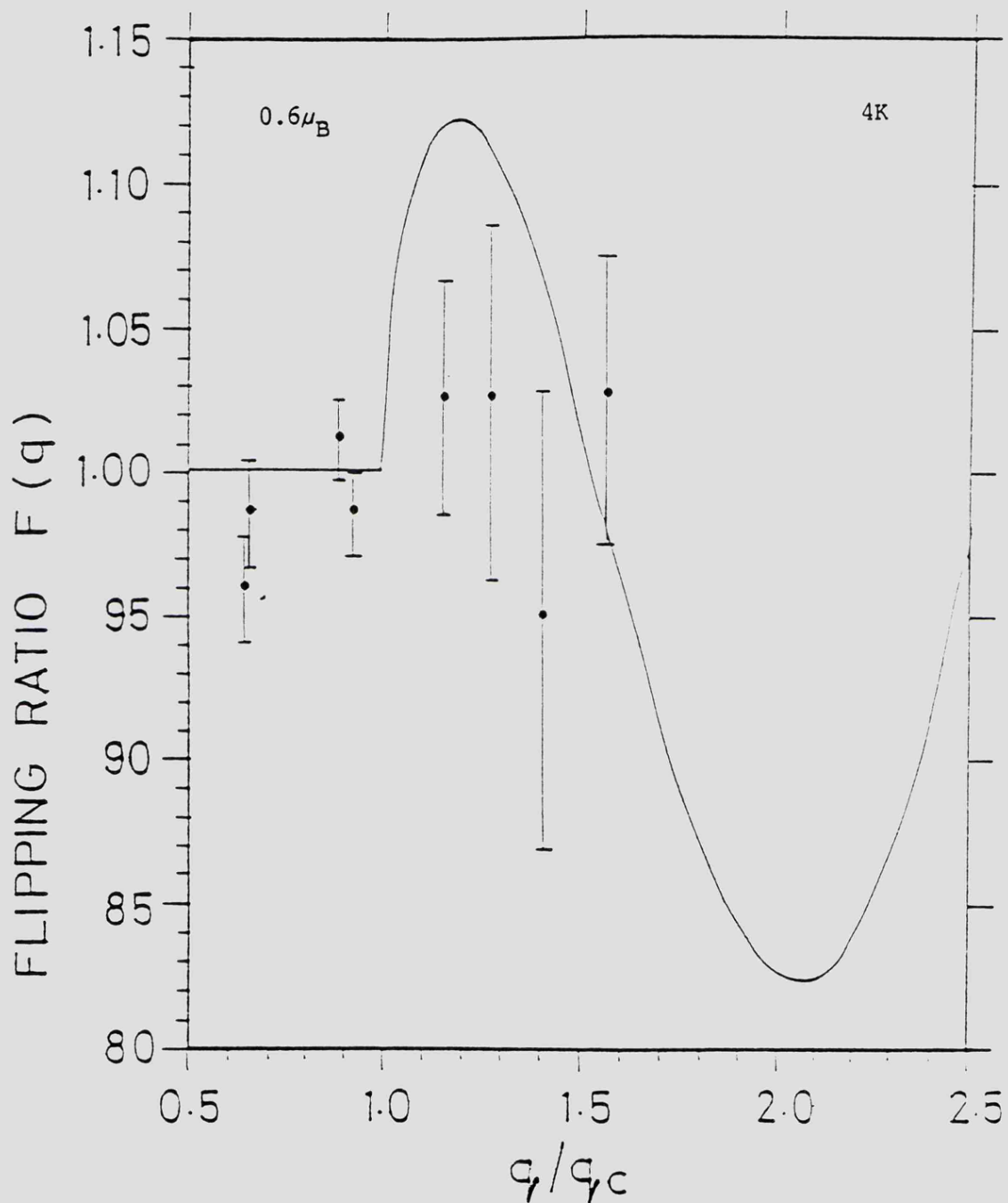


Figure (5.3) Variation in flipping ratio  $F(q)$  with the reduced wavevector for the 3.3ML Cr sample. The solid line is a prediction for a ferromagnetic layer with magnetic moment  $0.6\mu_B$ /atom.

of the outermost layers.

By analogy to these theoretical results it might be concluded that for a 3 layer thick Cr film a net in-plane magnetisation might be expected since the contribution of the central Cr layer would be dominated by the outermost layers. However, reference to figure (5.3) for the 3.3ML Cr sample shows that in fact no in-plane magnetisation is in fact seen. This would tend to suggest that the spins in the Cr layer are oriented normal to the surface as in that case a net magnetisation would not induce a spin-dependent neutron reflectivity. The spins could also be ordered antiferromagnetically normal to the surface in the  $c(2 \times 2)$  arrangement described by Blügel et al (1988). For the 2.0ML Cr sample, antiferromagnetic coupling might be anticipated in view of the theoretical calculations, but therefore no comment can be made on the orientation of the magnetic moments of the Cr layer as they may be antiferromagnetically coupled normal or parallel to the surface plane.

The 0.33ML samples of single atom thickness yield results that are consistent, although not conclusive, with in-plane ferromagnetism. The solid line fit to the data in figure (5.1) indicates that the magnetic moment per atom of the Cr layer is also indeed greatly enhanced, in agreement with the theoretical calculations of Fu et al (1985) for a Cr monolayer on Au(001). The large error bars in figure (5.1) precludes an accurate estimate of the moment per atom of the Cr layer but the deviation of the flipping ratio curve from unity above  $q_c$  can only be explained in terms of a greatly enhanced moment in comparison to the bulk moment as the deviation of  $F(q)$  from unity for a layer with the bulk moment of  $0.59\mu_B$  would be so small as to be immeasurable.

Surface magneto-optic Kerr effect (SMOKE) measurements like those

described in the next section for the Ag/Fe/Ag(001) sample were not possible on the 0.33ML Cr sample. The 200Å Ag overlayer was too thick for any ferromagnetic ordering in the Cr to be probed with the incident laser beam.

### 5.3 THE MAGNETIC ORDERING OF Fe IN A Ag/Fe/Ag(001) STRUCTURE

#### 5.3.1 INTRODUCTION

In the bulk Fe crystallises in the BCC phase with a large magnetic moment of  $2.22\mu_B$  per atom. Enhanced ferromagnetic moments for monolayer thick layers of Fe on Cu and Ag have been predicted by Fu et al (1985) (see table (5.1)) and Richter et al (1985), as well as for Ag/Fe/Ag sandwich structures. Calculations by Wang et al (1985) indicated that antiferromagnetic ordering was energetically more favourable in FCC Fe but that BCC Fe favoured ferromagnetic ordering.

The growth mode of Fe/Cu(001) has been shown to be layer-by-layer in the FCC phase by Newstead (1987) with AES and LEED, and by Hezaveh (1986) using LEED. Some discussion has been focussed on the Fe/Cu(001) system because of conflicting results of various authors. Mössbauer spectroscopy on 18Å thick Fe layers adsorbed onto Cu(001) by Keune et al (1977) indicated antiferromagnetic ordering of the Fe layers, but angle-resolved photoemission results from a Fe monolayer on Cu(001) obtained by Newstead (1987) indicated ferromagnetic ordering. Further studies by Newstead on a 7ML Fe film, however, suggested antiferromagnetism. Recently, Liu et al (1988) used polar Kerr-effect measurements on Fe layers of between 1.5 and 5.7ML on Cu(001) to show that the Fe was ferromagnetic with its magnetisation axis perpendicular to the plane of the surface. This is in agreement with the PNR results of Bland et al (1987) who could find no in-plane ferromagnetism for thin Fe layers grown epitaxially on Cu(001).

The initial growth of Fe/Ag(001) was first studied by Smith et al (1982) using LEED and AES. They concluded that the Fe grew layer-by-layer in the FCC phase up to 3ML after which island growth occurred. This deduction has since been shown to be incorrect by Jonker and Prinz (1986) who, by considering the in-plane lattice spacings showed that a 45° rotation of the BCC Fe lattice relative to the Ag lattice produces a lattice mismatch of less than 1%, compared to the 12% expansion for the FCC lattice proposed by Smith et al. More recent experiments by Jonker et al (1986) using angle resolved photoemission and LEED further confirmed the layer-by-layer growth of BCC Fe on Ag(001) up to 3ML and further agree on the formation of islands above this coverage. Further electron spectroscopy studies of an Fe monolayer on Ag(001) by Smith (1982) found that the Fe 3s multiplet splitting corresponded to a local magnetic moment of  $2.1\mu_B$ , close to the bulk value of  $2.22\mu_B$ , although no comment could be made on the magnetic ordering.

For the Fe/Ag(001) system, it is now widely accepted that the Fe is in the bulk BCC phase and is ferromagnetically ordered, as proposed by theoretical calculations by Blügel et al (1988). Calculations of the spin anisotropy of ferromagnetic monolayers of Fe, Ni and V by Gay and Richter (1986) showed that the easy direction of magnetisation of an Fe monolayer was perpendicular to the plane of the monolayer. This was explained as being due to the spin-orbit interaction and the perpendicular spin anisotropy was used to explain the spin-polarised photoemission results obtained by Jonker et al (1986) for the Fe/Ag(001) system, who could find no spin polarisation in the Fe up to 2.5ML coverage. Thus it was proposed that the Fe had perpendicular spin anisotropy up until 2.5ML coverage, after which the easy axis of magnetisation reverted to being in the plane of the layers.

Araya-Pochet et al (1988) used the surface magneto-optic Kerr effect (SMOKE) to study the thickness and temperature dependence of the spin anisotropy of ultrathin Fe layers on Ag(001). It was shown that Fe layers of one or two monolayers preferred spin orientation normal to the surface with a temperature dependent coercive force, whilst thicker Fe films exhibited in-plane spin orientation and thickness dependent coercive forces. These proposals are in conflict with spin-polarised photoemission results performed on Fe/Ag(001) by Stampanoni et al (1987), who proposed that at a temperature of 30K 3-4ML Fe films had perpendicular magnetisation but that thinner and thicker coverages were magnetised in-plane. Furthermore, the results also suggested that there was no perpendicular spin anisotropy for any coverage above a temperature of 100K, and temperature dependent measurements indicated that above 5ML, the Fe had a Curie temperature equal to that of bulk Fe. For coverages below 5ML the Fe layers had reduced Curie temperatures with  $T_c$  for 1 ML of Fe given as 400K.

In view of the previous results, a polarised neutron reflection study has been undertaken on an Ag/Fe/Ag(001) sandwich structure with an Fe thickness of 8ML to try and accurately determine the average magnetic moment per atom of the Fe layer. 8ML was chosen because, as stated above, there is some dispute as to whether 1ML of Fe has perpendicular or in-plane spin anisotropy and PNR can only measure in-plane ferromagnetism. There is agreement that Fe layers in the range 2-4ML have perpendicular magnetisation and so cannot be studied with PNR. It was therefore decided to use an 8ML sample as it would easily magnetise in-plane and there was uncertainty as to the effect of the Ag overlayer. It was not known whether the second Ag/Fe interface would cause the Fe film to behave as two separate slabs of 4ML or as a single slab of 8ML.

### 5.3.2 PNR RESULTS

The sample was grown in a vacuum of  $<1 \times 10^{-10}$  Torr with the substrate held at room temperature. The coverage was measured by monitoring the Ag  $M_{4,5}N_{4,5}N_{4,5}$  (356eV) differentiated Auger signal with Fe deposition. A resulting As-t plot can be seen in figure (5.4). The opening of the Fe vapour source shutter is denoted by  $t_1$  on the plot and it can be seen that the Auger intensity then decays linearly with time until  $t_2$ , at which point there is a break in the plot at  $I/I_0=0.58$ , indicating monolayer formation. After deposition of 8ML the p(1x1) LEED pattern was still sharp, but had slightly deteriorated from the pattern obtained from the clean substrate, indicating some disordering. A thick Ag layer of 100Å was then deposited on top of the Fe film, after which a p(1x1) LEED pattern was still observed.

The PNR measurements were initially made with the sample held at a temperature of 4K, and an applied field of 800Oe. This was done to prevent any reduction in the observed flipping ratio which could be observed due to a reduced Curie temperature, as was observed by Stampanoni et al (1987) for thinner Fe films adsorbed onto Ag(001). The beam was measured to be 87% polarised in the same way as before and the data corrected for this partial polarisation using equation (5.1)

The resulting variation in polarisation corrected flipping ratio  $F(q)$  with reduced wavevector is shown in figure (5.5). It can be seen that there is significant deviation of  $F(q)$  from unity for values of  $q$  above  $q_c$ , indicating in-plane ferromagnetic ordering. The solid line is the calculated flipping ratio response from an 8ML BCC Fe film covered with 95Å of Ag, and having a magnetic moment of  $1.0\mu_B$ /atom. This is in fact a large reduction compared to the bulk Fe moment of  $2.22\mu_B$  in total

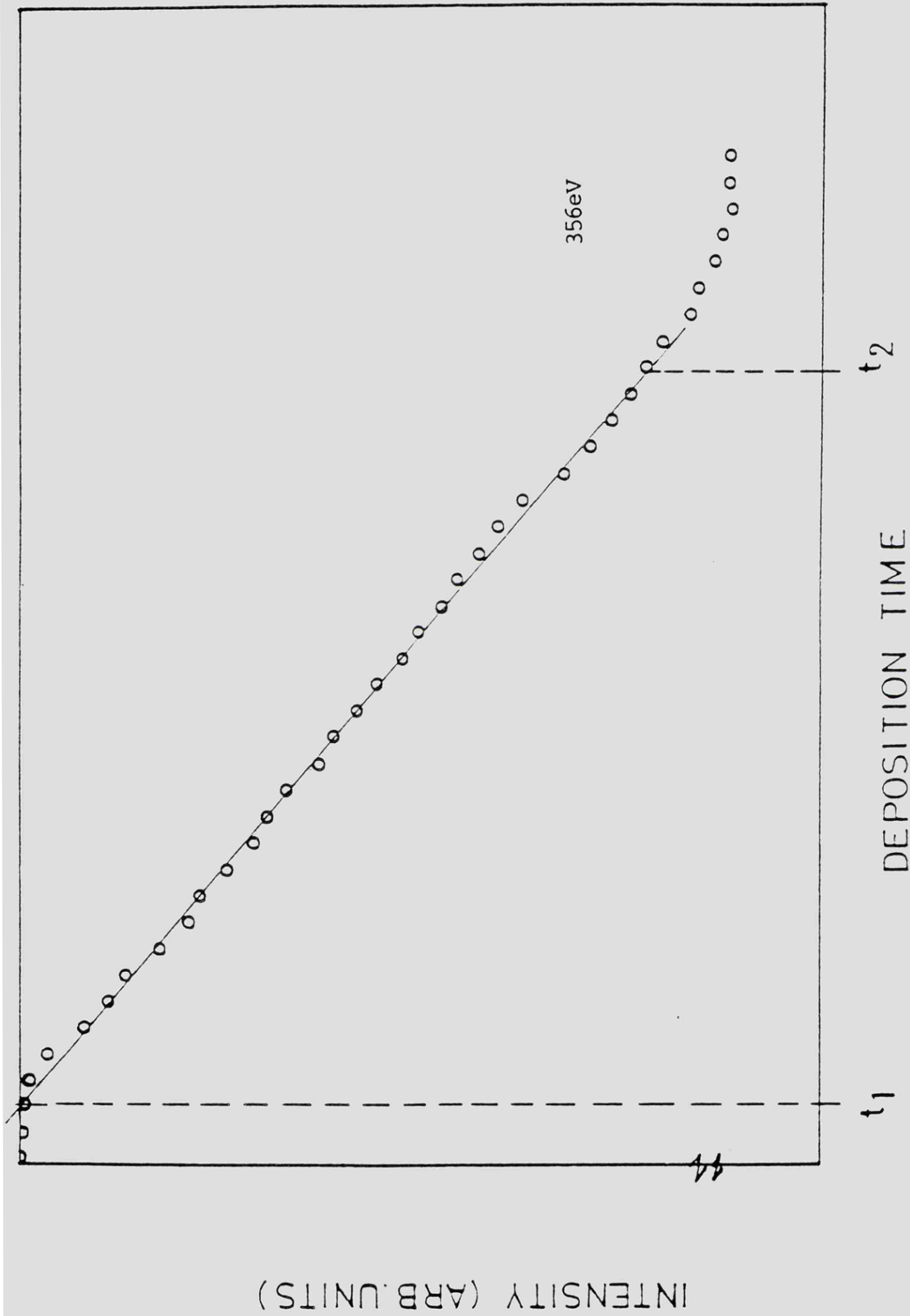


Figure (5.4) As-t plot showing the variation of the Ag MNN (356eV) Auger intensity with Fe deposition on Ag(001). Time  $t_1$  corresponds to opening the shutter and  $t_2$  to the completion of one Fe monolayer. The intensity ratio at  $t_2$  is given by  $I/I_0 = 0.58$

disagreement with the theoretical predictions of enhanced magnetic moments for ultrathin Fe films proposed by Fu et al (1985) and Richter et al (1985).

A temperature dependence scan was made of the flipping ratio for a fixed  $q$  of  $1.31q_c$  in the range  $4K < T < 300K$ . The resultant data is shown in figure (5.6). The vertical scale is the spin asymmetry given by  $(F-1)/(F+1)$ . It can be seen that the asymmetry remains constant throughout the whole temperature range, indicating no Curie temperature below 300K. This result is consistent with the reduced Curie temperatures measured by Stampanoni et al (1987) of values greater than 400K for Fe thicknesses of one monolayer or greater.

In order to show that the Fe film was saturated by the applied field of 8000e used in the PNR data, surface magneto-optic Kerr effect (SMOKE) measurements have been made on the 8ML film. SMOKE relates the change in polarisation state of light reflected from a ferromagnetic surface to the magnetisation in the region of the skin depth. It has important applications in the field of magnetic data storage (Connell, 1986) and has been shown to be a sensitive means of studying the magnetic properties of epitaxial thin films and multilayers (Katayama et al, 1988 and Liu et al, 1988). The Kerr effect measurements were carried out on equipment that has been described in detail elsewhere (Bland et al, 1989), and the geometry of the experimental arrangement is shown in figure (5.7).

With reference to figure (5.7), transverse geometry is given by the applied field  $\underline{B}$  being perpendicular to both the plane of incidence and surface normal  $\underline{n}$ . Polar geometry is defined by  $\underline{B}$  being parallel to both the plane of incidence and  $\underline{n}$ . The corresponding SMOKE results obtained

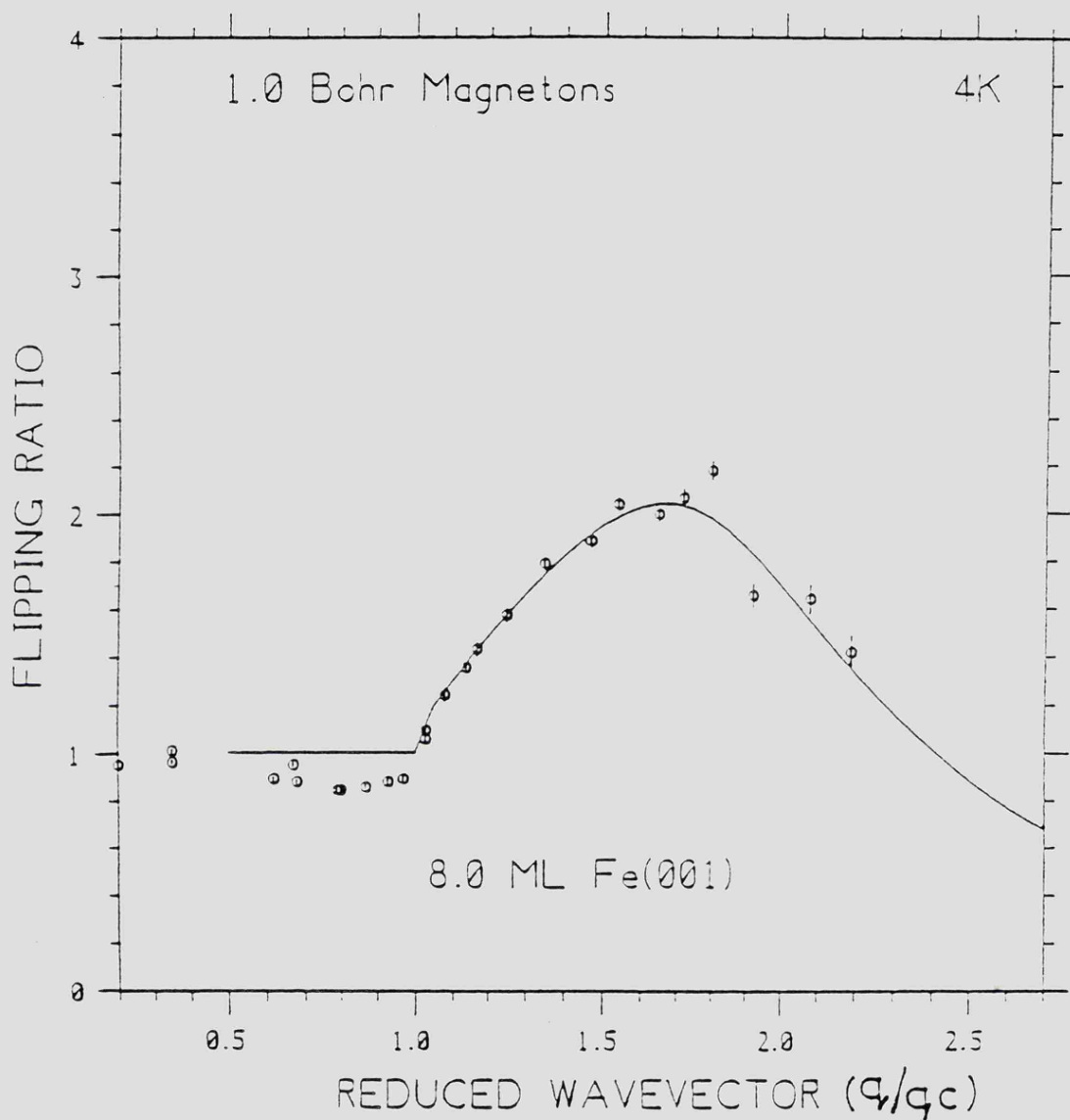


Figure (5.5) Variation of flipping ratio  $F(q)$  with the reduced wavevector for the 3ML Fe sample. The solid line is a prediction for a ferromagnetic layer with magnetic moment  $1.0\mu_B$  and overlayer thickness  $95\text{\AA}$ .

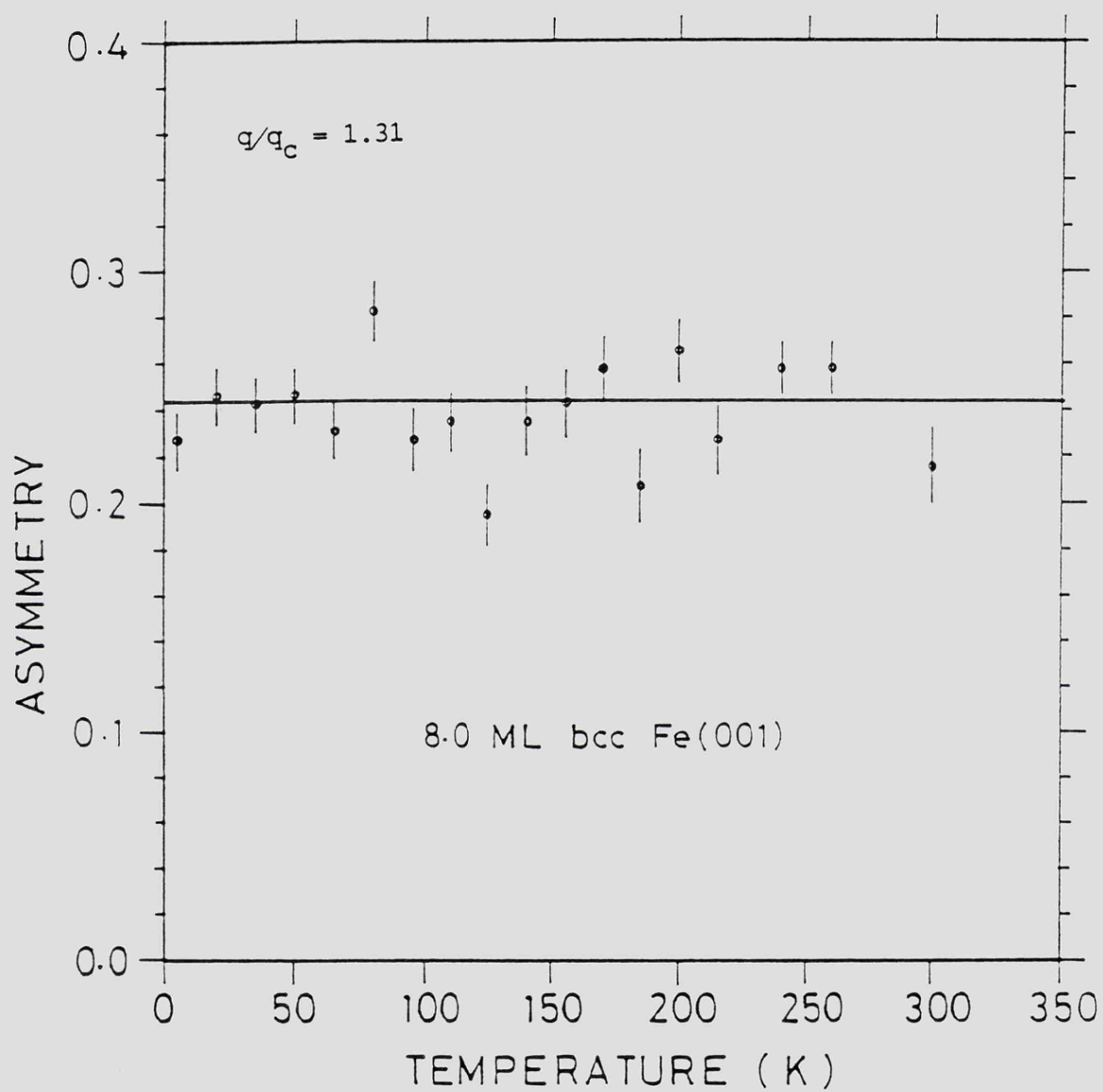


Figure (5.6) Variation of neutron spin asymmetry with temperature for the 8ML Fe sample at  $q/q_c = 1.31$ .

from the Fe sample are given in figure (5.8). It can be seen that with the polar geometry the Fe layers cannot be saturated by the swept field of  $\pm 2700\text{e}$ , in agreement with the earlier work of Jonker et al (1986) and Araya-Pochet et al (1988). The transverse geometry however is totally saturated within the swept field indicating that during the PNR experiment, the Fe layers were fully saturated.

### 5.3.3 DISCUSSION

The PNR results indicate a reduced moment per atom for the Fe layers of  $1.0 \pm 0.15\mu_B$ , in contrast to the earlier theoretical predictions of greatly enhanced moments for ultrathin Fe films. Several factors could possibly explain the lower asymmetry of the flipping ratio curve shown in figure (5.5). Interdiffusion of Fe into the Ag layers at either or both interfaces is a mechanism that could cause the observed data. The effect of a diffuse interface would be to reduce the amplitude of the oscillation in  $F(q)$ . Since the amplitude goes as the product of the layer thickness and the average magnetic moment per atom, a diffuse interface could mistakenly be taken for a reduced moment. However, in all previous studies of the Fe/Ag(001) system, no mention has ever been made of such behaviour. During the growth of the sample used in this work, no such behaviour could be detected either with LEED or AES, even at very low Fe coverage. Further evidence for the absence of a diffuse interface comes from the PNR data itself, as fits to the data in figure (5.5) involving non-sharp interfaces were not possible. The only good fit obtained is the one shown in the figure, involving two sharp interfaces and the reduced moment.

If the islanding reported for Fe/Ag(001) was very large and a large part of the Fe film was 'missing', then the PNR data could be interpreted as having a bulk moment with the reduced flipping ratio being due to that

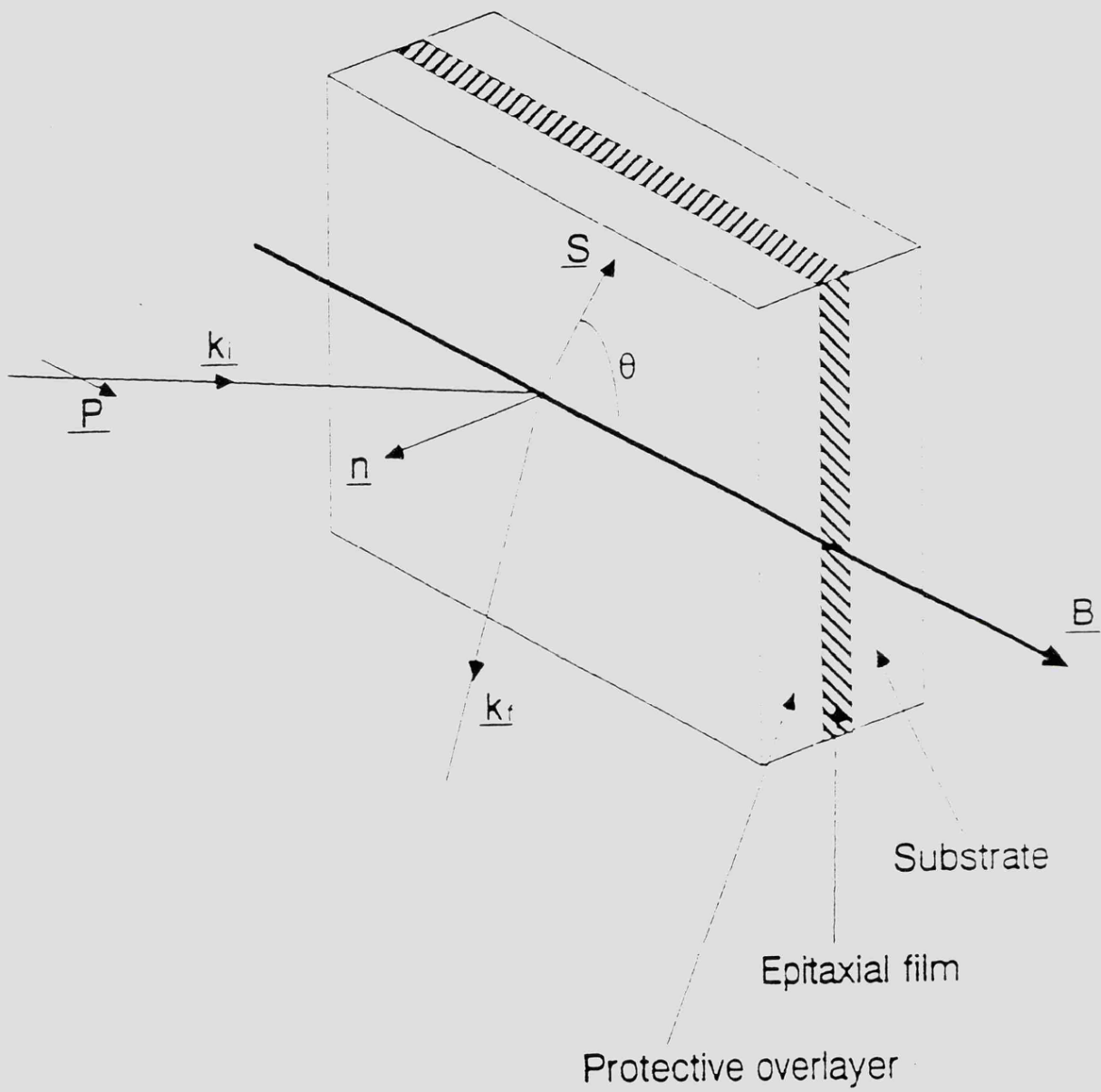


Figure (5.7) Experimental geometry for observing the magneto-optic Kerr effect.  $\underline{B}$  is the applied magnetic field.

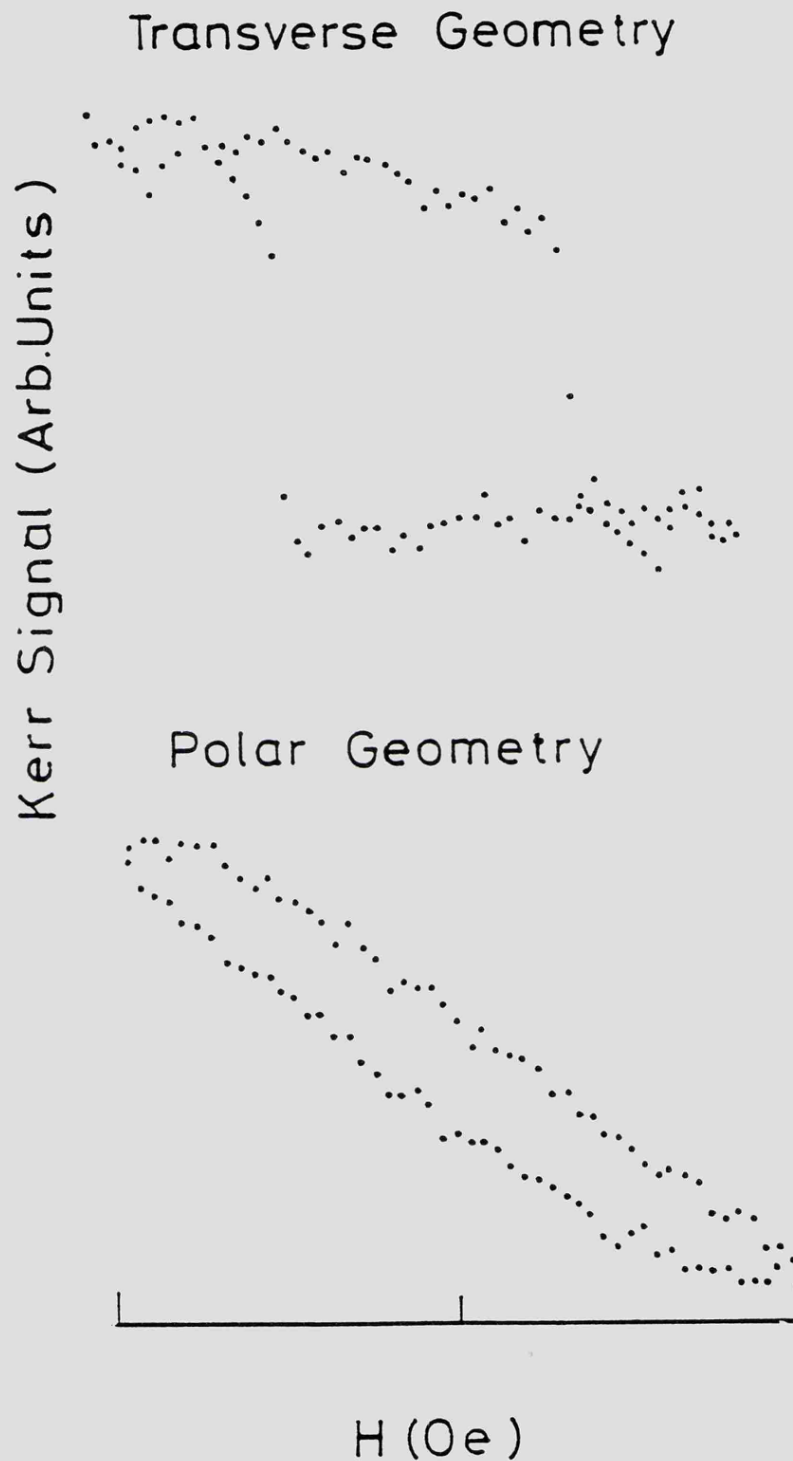


Figure (5.8) Surface Magneto-optic Kerr Effect hysteresis loops obtained from the 100ÅAg/8MLFe/Ag(001) sandwich structure in both transverse and polar geometries.

islanding. Scans across the sample after deposition found variations in Ag Auger signal corresponding to a variation in Fe thickness of  $\pm 4\%$ . For the observed flipping ratio curve to be explained in terms of Fe islanding, the coverage variation would have to be in the region of 50%, which is not the case. The small variation in Fe thickness across the substrate is not a problem as the neutron reflection technique measures the layer average which in this case is 8ML of Fe.

The possibility of the reduced moment being due to a reduced Curie temperature has already been shown to be unlikely (figure (5.6)). This suggests that there is no temperature dependence of the magnetisation in the film up to 300K as has been found for thinner Fe films by Araya-Pochet et al (1988). This indicates that the transition temperature  $T_c$  is determined by the film thickness and not the interface. That is, the double interface is not equivalent to two film each of 4ML thickness.

The only other possible explanation of the observed data would be a strong spin-anisotropy such that the Fe film could not be saturated in-plane. This has been shown not to be the case, as the Kerr effect data shows quite clearly in figure (5.8) that the Fe film is saturated in-plane at an applied field well below the 8000e used in the PNR experiment. It is therefore concluded that the Fe film must have a reduced magnetic moment of  $1.0 \pm 0.15\mu_B$ .

#### 5.4 SUMMARY

Polarised Neutron Reflection has been used to study metallic sandwich structures containing ultrathin layers of BCC Cr and Fe. For Cr layers of one atom thickness, the PNR data suggests in-plane ferromagnetic ordering with an enhanced magnetic moment. The large error bars on the 0.33ML Cr layer data prevents an accurate determination of

the magnetic moment per atom but the fitted curve in the figure suggests a value of  $5.1 \pm 2.5\mu_B$ . This is in agreement with the enhanced values predicted theoretically by Fu et al (1985) and experimentally by Hanf et al (1988) for Cr/Au(001).

For Cr thicknesses of 2.0 and 3.3ML, no in-plane ferromagnetism was detected and the layers have been assumed to be antiferromagnetic. The lack of any net magnetisation in the 3.3ML sample has been shown to indicate that the spins in that sample must be aligned perpendicularly with respect to the surface in the antiferromagnetic c(2x2) arrangement described by Blügel et al (1989) for the Cr(001) surface. No comment can be made about the spin alignment of the 2.0ML Cr sample.

PNR measurements on a  $100\text{\AA}\text{Ag}/8\text{MLFe}/\text{Ag}(001)$  structure have also shown in-plane ferromagnetic ordering, as found in previous studies of the Fe/Ag(001) system. An accurate estimate for the magnetic moment per atom of the Fe film has been possible and has yielded a reduced moment of  $1.0 \pm 0.15\mu_B$ , in disagreement with previous theoretical estimates. The Fe layers have been shown to be well ordered structurally with no alloying between the Ag and Fe taking place. SMOKE measurements from the sample show that in-plane saturation of the film is achieved and that the film cannot be magnetised out of plane. A further temperature dependent study using PNR has shown that the reduced moment is not a consequence of a reduced Curie temperature and also that the influence of the Ag overlayer is not to cause the 8ML Fe film to be equivalent to two 4ML films, but for its properties to be dependent on its complete thickness.

## CHAPTER 6

### X-RAY SCATTERING FROM Ge(001) SURFACES

- 6.1 Introduction
  
- 6.2 Thermal Disordering of the Ge(001) Surface
  - 6.2.1 Introduction
  - 6.2.2 Results
  - 6.2.3 Three Level Model
  - 6.2.4 Monte-Carlo Simulation
  - 6.2.5 Discussion
  
- 6.3 X-ray Scattering From a Vicinal Ge(001) Surface
  - 6.3.1 Introduction
  - 6.3.2 Results
  - 6.3.3 Discussion
  
- 6.4 Summary

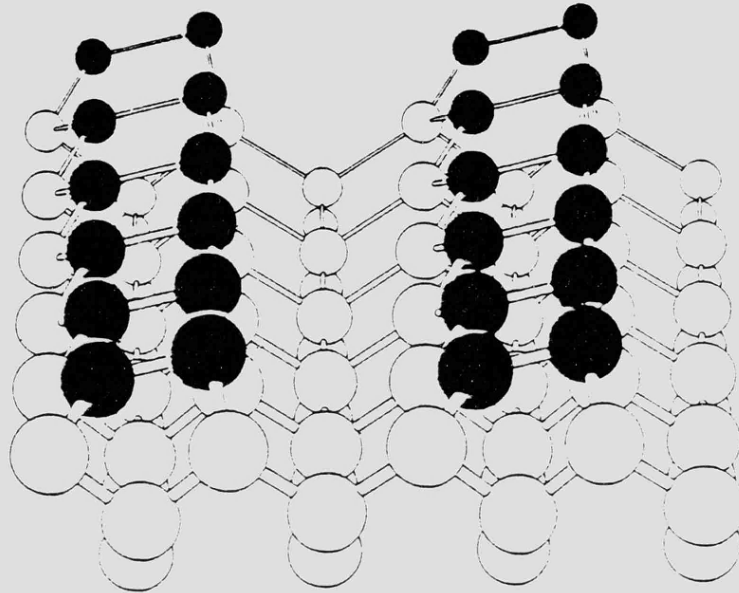
## CHAPTER 6

### X-RAY SCATTERING FROM Ge(001) SURFACES

#### 6.1 INTRODUCTION

The (001) surface of Ge is of much current interest as, along with Si(001), it is a typical example of a system possessing both a strong short-range reconstruction as well as a moderate range, energetically weaker one. Termination of the bulk lattice leaves two dangling bonds per surface atom, and the short-range interaction is generally believed to consist of the formation of buckled dimers by nearest-neighbour surface atoms, one atom buckles away from the surface whilst the other buckles in (Chadi, 1979). Ihm et al (1983) predicted that the dimer orientation would be disordered at room temperature with possible ground state configurations of c(2x2), p(2x2) or c(4x2). Density-functional calculations by Needels et al (1988) predicted that the p(2x2) and c(4x2) reconstructions are the most stable at low temperatures with a phase transition to buckled p(2x1) at  $T = 380 \pm 100\text{K}$ . Figure (6.1) is a schematic representation of the p(2x1) and c(4x2) symmetry configurations where the p(2x1) reconstruction is made up of dimers buckled in the same orientation whilst the c(4x2) is made up of alternating buckling of nearest-neighbour dimers. Using LEED and angle resolved photoemission, Kevan (1985) has found that the surface undergoes a c(4x2)  $\rightarrow$  p(2x1) transition at  $T=220\text{K}$ . Surface X-ray diffraction measurements by Grey et al (1988) have shown agreement with the basic dimer structure, but were unable to conclude whether the dimers were buckled or not. Figure (6.2) shows schematically the basic structure of the Ge(001) surface and its corresponding unit cell in reciprocal space. By measuring in the 1 direction along reciprocal lattice rods, Grey et al were able to propose that there is subsurface relaxation of the Ge lattice over eight layers.

a



b

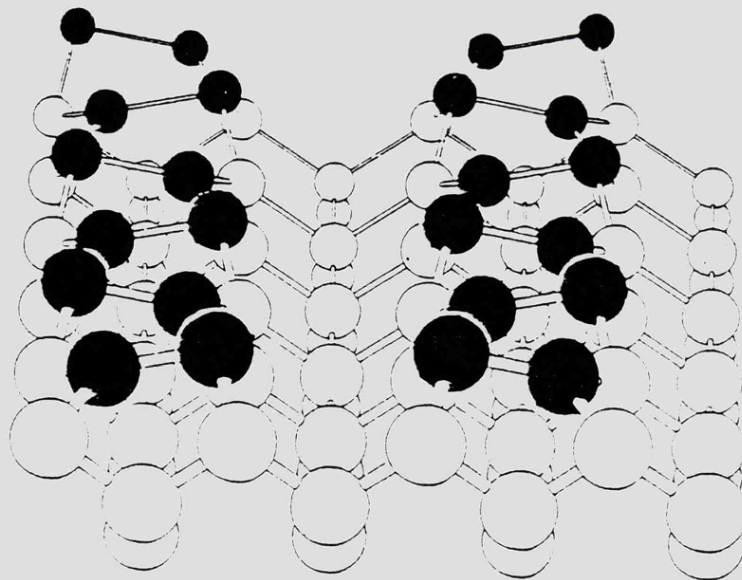


Figure (6.1) Perspective views of the dimer models on the Ge(001) surface. The dark atoms are the surface layer. (a) Buckled  $(2 \times 1)$  symmetry configuration. (b)  $c(4 \times 2)$  configuration, after Needels et al (1988).

Subsequent experiments by Lambert et al (1987) using He diffraction have shown that at temperatures <150K the surface orders into a c(4x2) reconstruction with some residual (2x2) areas, in agreement with Needels et al. Scanning Tunneling Microscopy studies by Kubby et al (1987) have shown regions of local (2x1), c(4x2) and p(2x2) symmetry with symmetric and asymmetric buckled dimer structure, although predicting that the asymmetric buckled dimer reconstruction does not require vacancy-type defects for stabilisation at room temperature as was previously thought.

In this chapter X-ray scattering studies from Ge(001) surfaces are presented that reveal a high temperature phase transition which has not previously been seen. In addition, scattering from a vicinal surface is proposed to be in broad agreement with previous results from such structures studied using LEED. Throughout this chapter the reflections from the surface are labelled using a surface notation defined by the unreconstructed tetragonal unit cell of side  $a_0/\sqrt{2}$  and depth  $a_0/4$  and given by the following relations:-

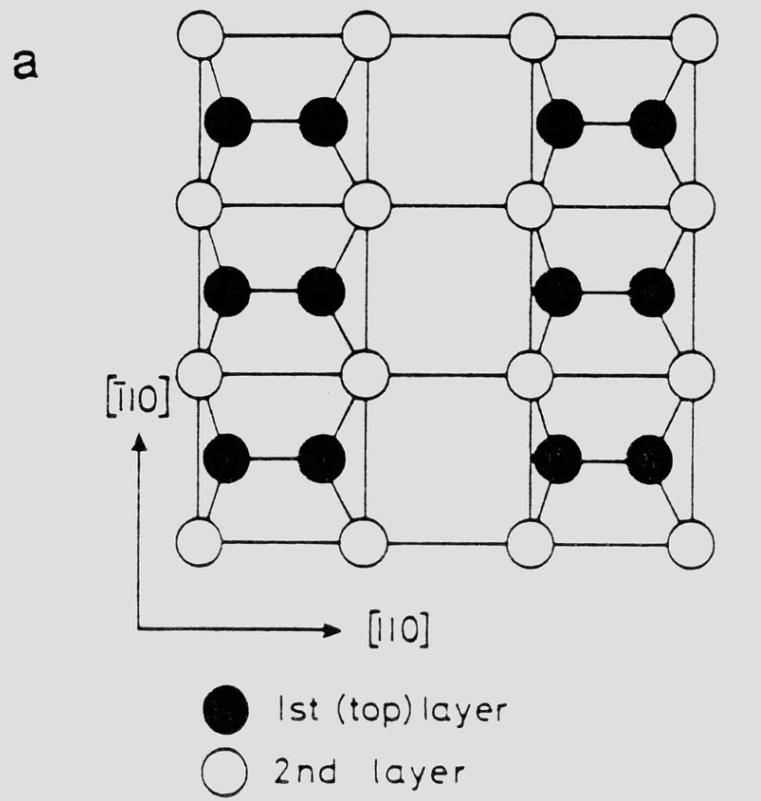
$$\begin{bmatrix} h \\ k \\ l \end{bmatrix}_{\text{surface}} = \begin{bmatrix} \frac{1}{2} & -\frac{1}{2} & 0 \\ \frac{1}{2} & \frac{1}{2} & 0 \\ 0 & 0 & \frac{1}{4} \end{bmatrix} \begin{bmatrix} H \\ K \\ L \end{bmatrix}_{\text{bulk}}$$

$$\begin{bmatrix} H \\ K \\ L \end{bmatrix}_{\text{bulk}} = \begin{bmatrix} 1 & 1 & 0 \\ -1 & 1 & 0 \\ 0 & 0 & 4 \end{bmatrix} \begin{bmatrix} h \\ k \\ l \end{bmatrix}_{\text{surface}}$$

## 6.2 THERMAL DISORDERING OF THE Ge(001) SURFACE

### 6.2.1 INTRODUCTION

In recent years the study of flat crystal surfaces has become widespread, not only due to fundamental interest, but also because of



RECIPROCAL SPACE

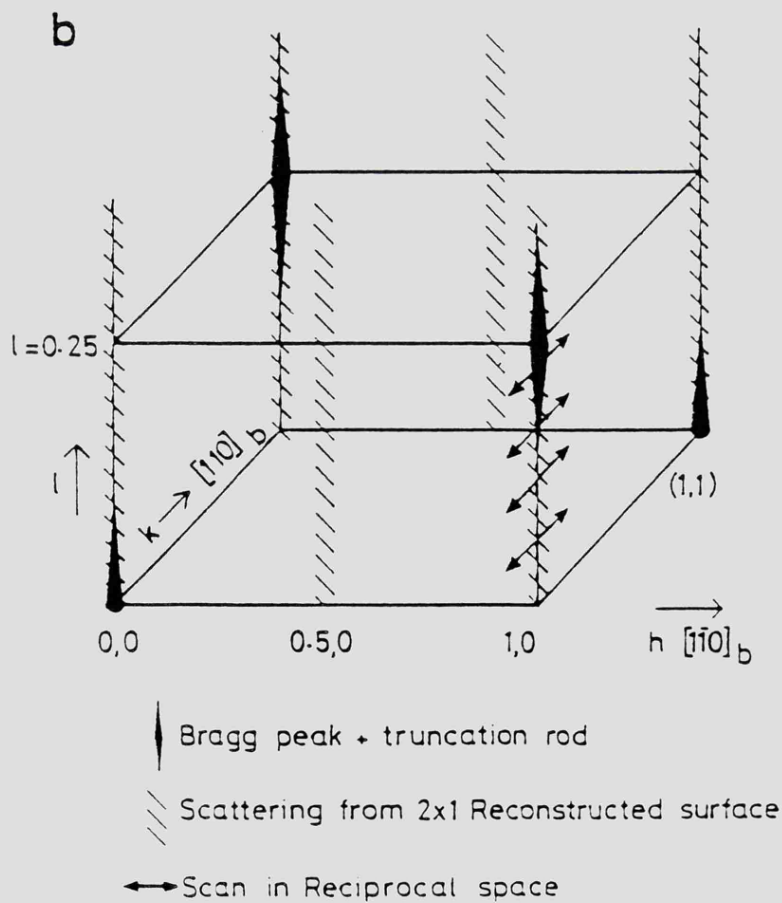


Figure (6.2) (a) Schematic view of the Ge(001) surface from above, the dark atoms are the top layer. (b) Unit cell in reciprocal space showing crystal truncation rods and diffraction rods due to the 2x1 reconstruction.

technological applications. Predictions of surface roughening transitions at much lower temperatures than those of the bulk melting points have been known for many years (for example Burton et al, 1951). In order to confirm these predictions, there has been much work in this field in the last decade. X-ray scattering has been used by Mochrie (1987) and Ocko and Mochrie (1988) to study the surface roughening of Cu(110) and proposed to be due to reversible faceting of the surface. Similarly, Robinson et al (1989) have studied the order-disorder transition on W(001) and concluded that it is due to the proliferation of steps or domain wall disordering. Other such experiments have been reported by Held et al (1987) using X-ray scattering on Ag(110) and by Salanon et al (1988) on Cu(113) using He diffraction.

McRae and Malic (1987) observed a new phase transition on Ge(111) at  $T = 1058\text{K}$  using LEED, and discussed their results in terms of surface melting of the outermost double layer. More recently, using further LEED results (McRae and Malic, 1988) and molecular dynamics simulations (McRae et al, 1988), the transition has been proposed to be due to lateral strain of domains to a depth of one atomic layer, and the disordering described as a loss of registry between the strained domains and the substrate. In order to discover if there is a surface phase transition on the (001) face of Ge, similar X-ray scattering measurements to those undertaken by Robinson et al (1989) on W(001) have been made on Ge(001) and the results presented in the following sections.

### 6.2.2 RESULTS

The  $8 \times 10 \times 2\text{mm}$  sample was cleaned with repeated cycles of  $\text{Ar}^+$  ions (800eV,  $1\mu\text{A}$ ) after a 15 minute pre-anneal at 751K before a final anneal at 983K with a slow cool ( $\sim 1^\circ/\text{sec}$ ). This procedure was repeated until there was no further decrease in the HWHM of the  $(0, 3/2, 0.03)$  or  $(3/2,$

0, 0.03) fractional order reflections. These fractional order reflections were used as they have been shown to be the most intense (Grey et al, 1987). The value of  $l = 0.03$  was chosen such that the angle of incidence  $\beta$  was  $0.64^\circ$  so that with an end of beamline slit of width  $300\mu\text{m}$ , the sample would be completely flooded by the beam to prevent intensity changes because of movement of the sample with temperature. It should be noted that the half order intensity was optimised at each temperature to ensure that there was no possibility of intensity variation due to sample movement.

It was found that the best surface was obtained after depositing 1ML of Ge from the Ge Knudsen cell fitted to the UHV chamber, onto the surface prior to cleaning . Using the alignment procedure described in section 3.4.4, the sample miscut was determined to be  $0.044^\circ$  along the bulk [110] azimuth, implying an average terrace size of  $3800\text{\AA}$  with the more stable double layer steps (Chadi, 1987) in the k direction. The domain sizes in the h direction would be even larger. Figure (6.3) shows transverse  $\phi$  scans of the Ge(001) (0, 3/2, 0.03) fractional order diffraction rod, which corresponds to the (1x2) reconstructed surface domain, for various sample temperatures. The y axis is on a scale of detector counts per  $10^5$  monitor counts, which is used throughout this chapter. The solid lines are lorentzian fits to the data points using the expression:-

$$I = \frac{A}{1 + q_T L^2} + B \quad - (6.1)$$

where B = constant background

$q_T$  = deviation in momentum transfer in transverse direction

L = surface correlation length

The shift in  $\phi$  of the peak centre with temperature corresponds to the change in lattice constant due to thermal expansion of the crystal. The surface correlation length is obtained from:-

$$L = 1/\Delta q_{\text{FWHM}} \quad - (6.2)$$

Where  $\Delta q_{\text{FWHM}}$  is the FWHM in momentum transfer  $q$  in  $\text{\AA}^{-1}$ . Using the fit to the curve at room temperature from figure (6.3) gives:-

$$L = 1621 \pm 43\text{\AA}$$

indicating a very flat surface. The correlation length  $L$  is significantly less than the instrumental resolution which is defined by the coherence length of the incident X-ray beam to be  $9000\text{\AA}$ . The correlation length of the  $(2 \times 1)$  domain is obtained from the width of the  $(3/2, 0, 0.03)$  reflection, and is calculated to be:-

$$L = 1216 \pm 30\text{\AA}$$

Thus both domains have dimensions of the same order.

The integrated intensity of the  $(0, 3/2, 0.03)$  reflection shown in figure (6.3) decreases by an order of magnitude above  $953\text{K}$ , indicating a reduction in the area of reconstructed surface, and then disappears into the background above  $973\text{K}$ . This can be seen more readily by reference to figure (6.4c). The plot shows the variation of integrated intensity of the  $(0, 3/2, 0.03)$  peak with temperature on a semi-log scale. As can be seen, the surface undergoes a phase transition at a temperature just below  $970\text{K}$ . This transition was found to be reversible as long as the

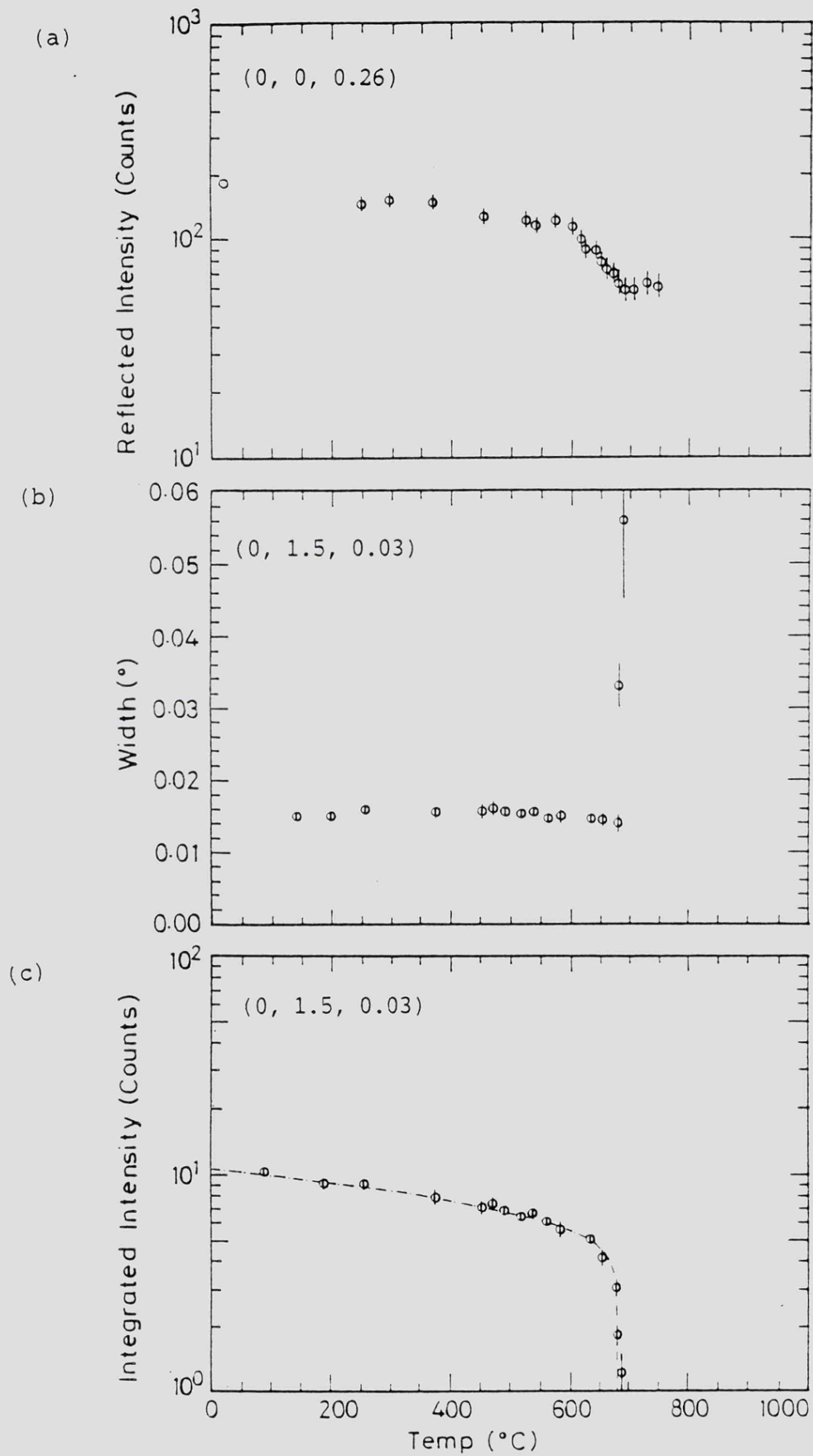


Figure (6.4) (a) Variation in the  $(0, 0, 0.26)$  reflected intensity with temperature. (b) HWHM of the  $(0, 3/2, 0.03)$  reflection with temperature. (c) variation of the  $(0, 3/2, 0.03)$  integrated intensity over the same temperature range.

crystal temperature was not raised above ~1010K and found to also occur in the (1x2) reconstructed domain, the integrated intensity of the (3/2, 0, 0.03) rod also rapidly decreasing above ~973K. RHEED study of the sample at the transition temperatures showed 2x1 → p(1x1) behaviour. There is also no variation in the linear background of the Lorentzian fits even above  $T_c$ . The intensity variation of a continuous transition with temperature can be written as (Als-Nielsen and Dietrich, 1967):-

$$I(T) = I_0 \exp(-2MT) [1-(T/T_c)]^{2\beta} \quad - (6.3)$$

for  $T < T_c$  where,

$T$  = temperature in K

$T_c$  = transition temperature

$I_0$  = integrated intensity at  $T=0K$

$\beta$  = a critical exponent associated with the transition

The expression  $[1-(T/T_c)]^{2\beta}$  describes the temperature dependence of the long range order parameter (Onsager, 1945). The dashed line in figure (6.4c) is a fit to the data using the above expression, with the following values;  $I_0 = 10.73 \pm 0.27$ ,  $M = (2.1 \pm 0.6) \times 10^{-4} \text{ K}^{-1}$ ,  $\beta = 0.094 \pm 0.010$  and  $T_c = 954 \pm 7K$ . The value of  $\beta = 0.094$  is less than the value obtained by McRae and Malic for Ge(111) of  $\beta = 0.15$ , and less than that derived from the Ising model of  $\beta = 0.125$  (see Onsager, 1945). The expression  $I(T) \propto \exp(-2MT)$  describes Debye-Waller reduction in intensity due to the vibration of atoms about their equilibrium positions.  $M$  is independent of temperature and is related to the mean thermal displacement of atoms about their equilibrium positions by:-

$$\langle u^2 \rangle^{1/2} = (2MT/q^2)^{1/2} \quad - (6.4)$$

where  $q$  is the momentum transfer associated with the diffraction rod and the angled brackets  $\langle \rangle$  denote a time average. From the fit using equation (6.3), the mean thermal vibrational amplitude of atoms at the surface of Ge(001) at 300K is:-

$$\langle u^2 \rangle^{1/2} = 0.15 \pm 0.05 \text{ \AA}$$

The value of  $M$  for bulk Ge can be obtained by the expression of Pendry (1974):-

$$M = 3q^2 / (2mk_B \theta_D^2) \quad - (6.5)$$

where  $m$  = mass of the atom in electron units =  $138.4 \times 10^3$  for Ge

$k_B$  = Boltzman's constant in Hartrees/K

$\theta_D$  = Debye Temperature = 370K for Ge

Using the above expression gives  $M_{\text{Ge}} = 2.65 \times 10^{-5} q^2$ , and so substitution into (6.4) gives:-

$$\langle u^2 \rangle^{1/2} = 0.07 \text{ \AA}$$

for bulk Ge at 300K. Thus, from the data it can be seen that at the surface of Ge(001) the mean thermal displacement about the mean atomic position is approximately double that of the bulk. This seems a reasonable result as Robinson et al quote mean vibrational amplitude of  $0.19 \pm 0.07 \text{ \AA}$  for atoms on the surface of W(001), a factor of four larger than the bulk value.

Figure (6.4b) shows the HWHM vs. temperature of the (0, 3/2, 0.03) fractional order rods shown in figure (6.3). As can be seen, the half

width remains completely constant below  $T_c$ , indicating that the surface correlation length remains constant at  $L = 1621 \pm 43 \text{ \AA}$ . This rules out the formation of steps below  $T_c$ , as such steps would mean a reduction in the surface correlation length with subsequent increase in the half-width. From the fitted curve to the fractional order peak at  $T = 962\text{K}$ , it is possible to obtain the reduced correlation length at that temperature of:-

$$L = 434 \pm 85 \text{ \AA}$$

It can be seen that the correlation length rises significantly only when the fractional order integrated intensity is ~10% of its value at room temperature.

Figure (6.4a) shows the specular reflectivity from the Ge surface corresponding to the (0, 0, 0.26) on a semi-log plot against temperature. Again there is a linear decrease in the intensity until a critical temperature  $T_c$  where the intensity falls off sharply to a noise level which remains constant. It can be seen that the transition temperature  $T_c$  is the same for the fractional order intensity, half width and reflectivity to within  $\pm 5\text{K}$ . Reflectivity scans have been made as a function of  $l$  for various sample temperatures by varying the angle of incidence  $\beta$ . Figure (6.5) shows such scans for sample temperatures of room temperature, 948K, 973K and 1023K. Als-Neilsen (1985) has shown that X-ray reflectivity can be used as a probe of surface roughness and that for a perfectly flat surface the Fresnel reflectivity can be approximated to:-

$$R_F = \left( \frac{\beta_c}{2\beta} \right)^4 \quad \beta \gg \beta_c \quad - (6.6)$$

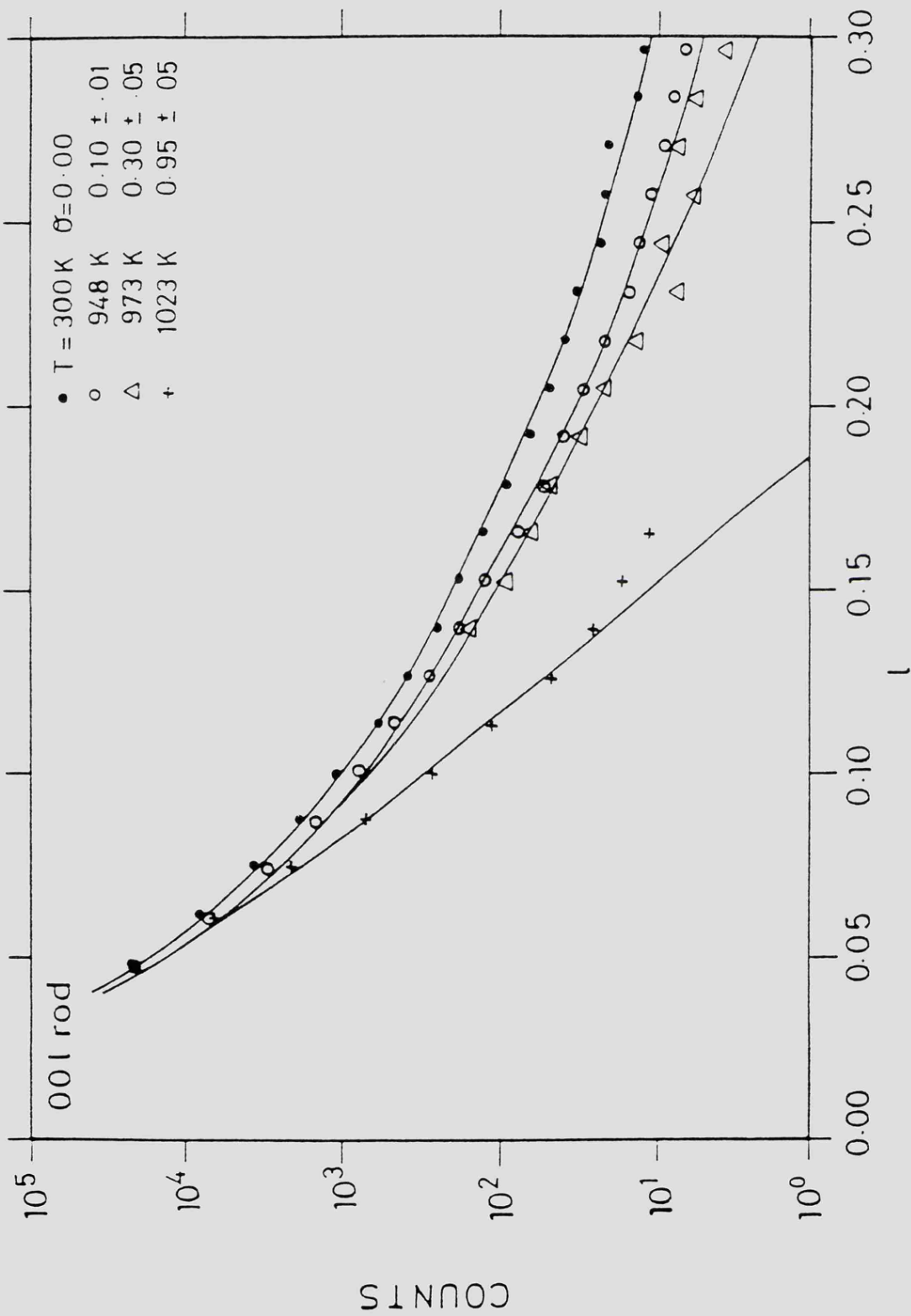


Figure (6.5) (0, 0, l) reflected intensity at various sample temperatures. The solid lines are fits to the data using the three level model.

Where  $\beta_c$  is the critical angle for total external reflection. For a non perfectly flat surface, the reflectivity deviates from the Fresnel curve but can be used to calculate an rms roughness value using the following expression:-

$$\log_e(R/R_F) = -\sigma^2 Q^2 \quad - (6.7)$$

where R is the reflectivity,  $R_F$  is the Fresnel reflectivity, Q is the perpendicular momentum transfer and  $\sigma$  is the rms variation in height of the surface. Fits to the (0, 0, 1) rod scans at different temperatures give the following values to the rms roughness of the surface:-

<u>Temp(K)</u>	<u>rms roughness</u>
300	1.74 $\pm$ 0.02Å
868	1.74 $\pm$ 0.02Å
948	2.67 $\pm$ 0.11Å
973	3.94 $\pm$ 0.20Å
983	4.79 $\pm$ 0.10Å
1023	8.45 $\pm$ 0.10Å

It can be seen that there is a significant roughening behaviour above ~950K. When taken to 1023K and above, it was not possible to recover the surface to its original condition by cooling indicating a different roughening behaviour from that which occurs at  $T_c$ . Repetition of the initial cleaning cycle was required to restore the surface to its original condition.

There are several disordering mechanisms that can be considered to explain the change in intensity at  $T_c$ . Surface melting has been studied on Pb(110) by Frenken et al (1985), but the surface melting transition

occurs at millidegrees less than the bulk melting temperature, which is not the case for this experiment. McRae and Malic (1987) initially suggested that the phase transition they measured with LEED on Ge(111) at 150K below the bulk Ge melting temperature was surface melting, but later rejected this argument in favour of a loss of lateral registry in the outermost double layer of the crystal associated with strained domains (McRae and Malic, 1988 and McRae et al,1988). Robinson et al (1989) have studied the order-disorder transition on W(001) using surface X-ray diffraction, but in that case the superlattice reflection integrated intensity remains constant through the transition with concurrent increase in half width indicating domain wall movement. This is in contrast to this data on Ge where the integrated intensity rapidly decreases but the half width remains constant until almost the end of the transition.

The possibility of the proliferation of steps would explain the change in reflectivity with increasing temperature but not the behaviour of the half width of the fractional order reflection. Across a double step the correlations between reconstructed domains are lost, as is described in section 6.3 of this chapter. Thus the fractional order half width should increase at the onset of the transition, reflecting the decrease in the terrace size distribution. The breaking of dimer bonds at random positions would explain the decrease in the integrated intensity of the fractional order, but the energy required to produce this mechanism is far greater than the energy available at this temperature.

Desorption of Ge atoms from the surface is negligible; reference to vapour pressure tables predicts that at  $T_c$  a single of Ge layer would take ~27hrs to desorb but at the transition temperature at which McRae and Malic measured the phase transition on Ge(111), desorption becomes

much more significant.

Therefore it is proposed that the disordering process involves an assisted breakup of dimers along with significant vertical movement of the Ge atoms. Thus when a dimer is broken a point defect or vacancy is created as one of the atoms in the broken dimer jumps up onto the surface to create an adatom. Thus the number of dimers would decrease with consequent decrease in the integrated intensity of the fractional order but if the creation of adatom-vacancy pairs was random over the reconstructed domain, the dimension of the domain would remain constant. Thus there would be no change in the half width of the fractional order reflection until the number of adatom-vacancy pairs was so great that instead of one large domain the reconstruction became a series of smaller domains, and hence the fractional order half width would increase, as is observed in the data.

### 6.2.3 THREE LEVEL MODEL

X-ray scattering from rough surfaces has been described in terms of a two level model by Vlieg et al (1989). It was shown that the scattered intensity can be written as the sum of a sharp (Bragg) component  $I_B$  and a diffuse component  $I_D$ . The diffuse component is dependent on a correlation function  $C(\underline{r}_{//})$  which describes the height-height correlation of the surface and varies from 0 to 1. If there is no correlation between surface heights then  $C(\underline{r}_{//}) \rightarrow 0$ , but as the surface height correlation increases then  $C(\underline{r}_{//}) \rightarrow 1$ . The Bragg component  $I_B$  is independent of the correlation function.

The two level model of Vlieg et al has been extended to three levels to describe the observed disordering. Assuming that the surface is initially flat (level 0) and no steps occur during the transition, when

an adatom (level 1) is created is also created a corresponding vacancy (level -1) as is shown in figure (6.6). Then assuming there is no desorption the population of levels can be given by:-

$$\theta_{\text{adatom}} = \theta_{\text{vacancy}} = \theta \quad - (6.8)$$

The one position probability of finding an atom at level N is given by:-

$$P_1(N) = (1-2\theta)\delta_{0,N} + \theta(\delta_{-1,N} + \delta_{+1,N}) \quad - (6.9)$$

If the positions of the adatoms and vacancies are uncorrelated ( $C(\underline{r}_{//})=0$ ) then the two-position probability is simply the product of two one-position probabilities:-

$$P(N,M,\underline{r}_{//}) = P(N)P(M) \quad - (6.10)$$

and the reflected intensity is then given by:-

$$I_{(001)} = C \sum_{N,M} e^{2\pi i l(N-M)} P(N)P(M) \quad - (6.11)$$

Where C is a prefactor that contains a constant term and also contains  $|F_{001}|^2 |F_{\text{CTR}}|^2$ , which is the scattered intensity from one column of unit cells. Substitution of equation (6.9) into (6.11) and summation over the three levels gives:-

$$I_{(001)} = C\{1-2\theta[2-3\theta+2(2\theta-1)\cos 2\pi l - \theta\cos 4\pi l]\} \quad - (6.12)$$

As  $\theta \rightarrow 0.5$  the model becomes unphysical as there are almost no atoms left in the original level and then double layer steps are more abundant than single layer steps. The fits to the  $I_{(001)}$  reflectivity curves in figure

## Vacancy - adatom creation

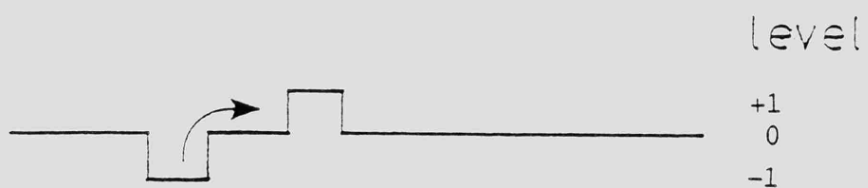


Figure (6.6) Schematic diagram showing the origin of the three level model, the levels being labelled -1, 0, and +1.

(6.5) are fitted using equation (6.12) with the prefactor given by:-

$$C = \frac{A}{q_3^2 \sin^2 q_3 a_3} \quad - (6.13)$$

Where A is a fitted constant. Note that for small  $q_3$ , (6.13) reduces to the  $\beta^{-4}$  behaviour shown in equation (6.9) as  $q_3 = 2k\sin\beta$ . the fitted values of  $\theta$  for each temperature are given below:-

<u>TEMP(K)</u>	<u><math>\theta</math></u>
300K	0.08 $\pm$ 0.01
868K	0.08 $\pm$ 0.01
948K	0.19 $\pm$ 0.01
973K	0.30 $\pm$ 0.01
983K	0.37 $\pm$ 0.01
987K	0.38 $\pm$ 0.01
1023K	1.00 $\pm$ 0.01

As can be seen there is a significant increase in  $\theta$  above ~950K in agreement with the fractional order intensity. The value of  $\theta$  at 1023K of 1.00 is obviously physically unreal as it implies that the vacancy level is empty and the adatom level is completely filled. therefore the three-level model cannot adequately describe the roughness at this temperature and so adds weight to the argument that a separate roughening mechanism, possibly step creation, occurs above this temperature. For lower temperatures  $\theta$  remains constant below 900K and then rises rapidly through  $T_c$  before tending to a limit at ~0.38. This seems to be reasonable as  $\theta=0.33$  corresponds to each of the three levels being equally occupied. If adatom-vacancy creation is assumed to be the only roughening mechanism at these temperatures it is plausible that an equilibrium would be reached at, or near, the point where each level is

equally occupied.

#### 6.2.4 MONTE-CARLO SIMULATION

To try and model the roughening of the surface, a Monte-Carlo program has been written by Dr J W M Frenken from the F.O.M. Institute Amsterdam. The starting point is a perfectly flat surface comprised of a diamond lattice with dimers on the surface (one dimer bond per two surface atoms), in an array of 25x25 atoms. The dynamics of the transition is studied by counting the number of dimer bonds on the surface. The energy involved in creating adatom-vacancy pairs is proportional to the change in the total number of dimer bonds. Thus by counting the number of bonds, the intensity of the half-order peak can be monitored. Figure (6.7) shows the values of  $\theta$  obtained from the Monte-Carlo simulation as a function of  $kT/E$ , where  $T$  is the temperature and  $E$  is the activation energy required to break the dimer bonds. As can be seen, the value of  $\theta$  rises rapidly at  $kT/E=0.2$  until it tends to a limit of  $\theta \approx 0.35$ , in agreement with the values of  $\theta$  obtained from the fits to the specular reflectivity curves shown in figure (6.5). Figure (6.8) shows the half-order intensity versus  $kT/E$  obtained from the number of dimer bonds counted by the Monte-Carlo program. The sharp transition shown at  $kT/E \approx 0.2$  compares favourably with the sharp transition seen in the experimental data at  $T_c = 954 \pm 7K$ . Substitution of the value for  $T_c$  into  $kT/E$  gives a estimate of the effective dimer rupture energy of  $0.41 \pm 0.05$  eV.

#### 6.2.5 DISCUSSION

From the observation that the width of the half-order reflection remains constant until almost through the transition, the phase transition must be of a local nature. That is, the proliferation of steps can be discounted as each terrace would scatter incoherently with respect

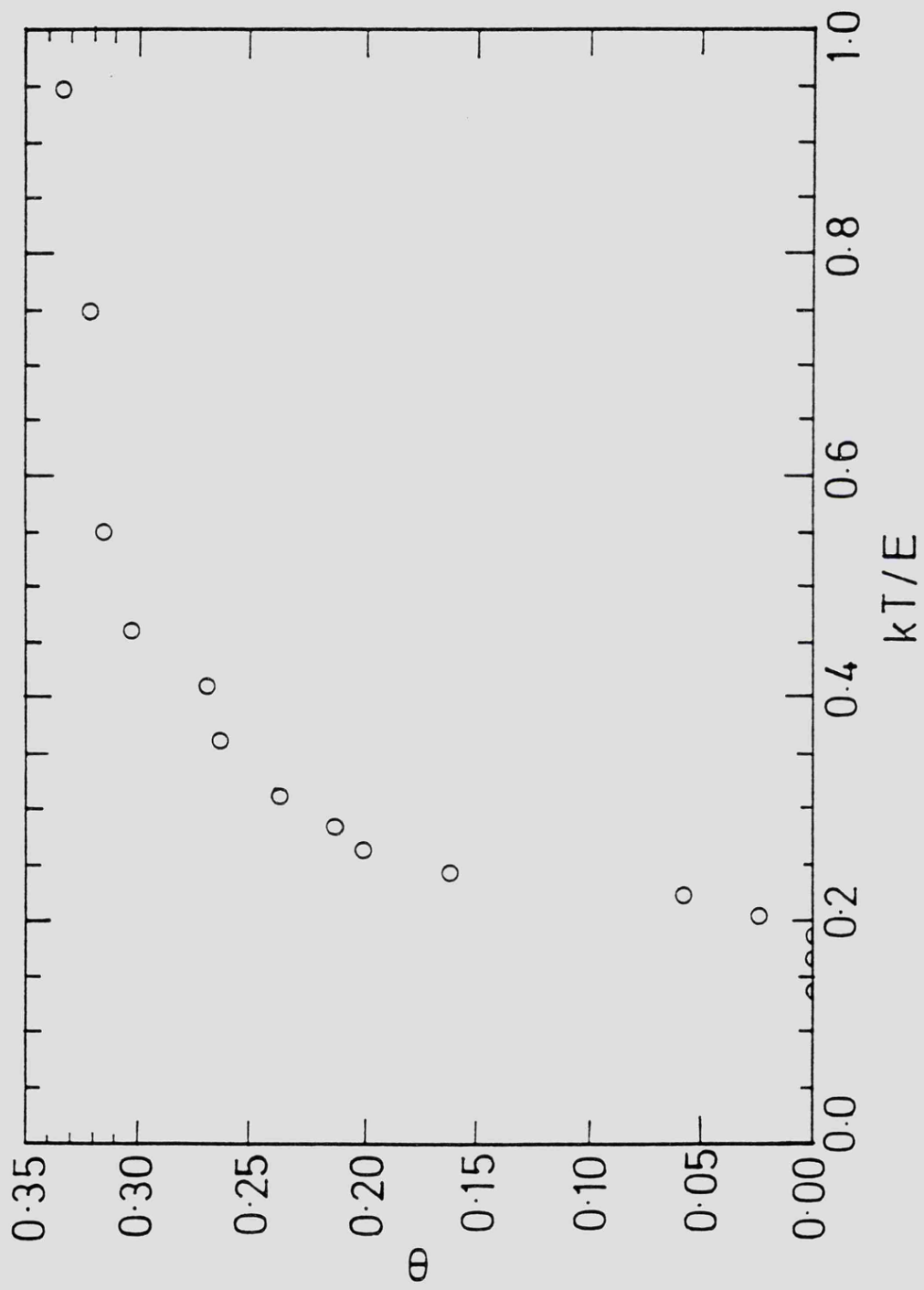


Figure (6.7) Variation of the number of adatoms  $\theta$  with reduced temperature  $kT/E$ , obtained from the Monte-Carlo program.

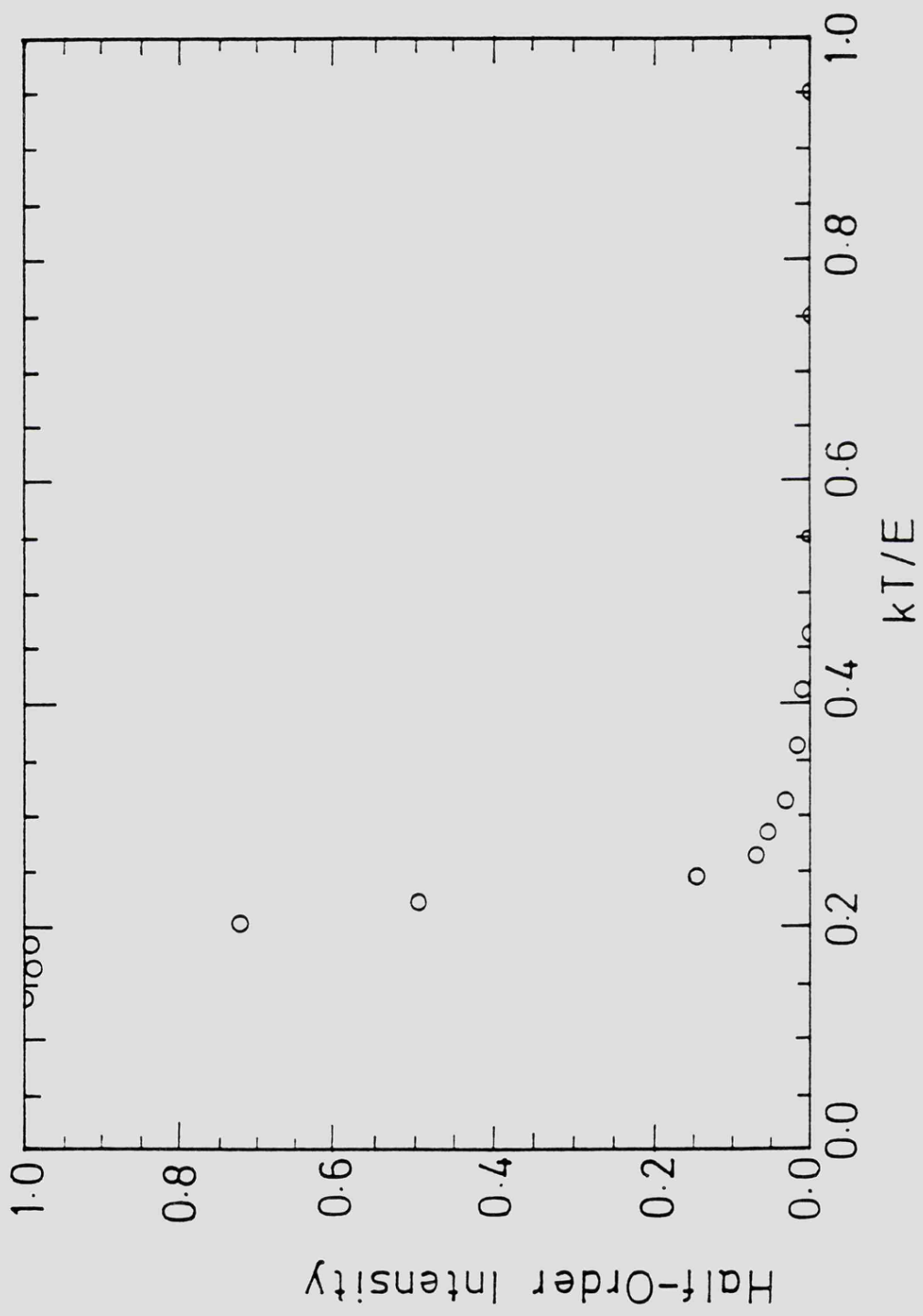


Figure (6.8) Variation of fractional order intensity with  $kT/E$ , obtained from the Monte-Carlo program.

to other levels with consequent changes in the half-order profile. At high temperatures it becomes possible for atoms or dimers to jump on top of the surface thus leading to a decrease in the number of dimer bonds and hence a decrease in the integrated intensity of the half-order reflection. The transition might be expected to be a smooth reduction of all the intensities but nevertheless the measured intensities decrease abruptly at the transition temperature  $T_c$ . The sharpness of the transition may be explained in terms energy required for atoms to become adatoms. Initially the energy cost in terms of the number of broken dimer bonds is large when atoms leave the surface layer. However, when the surface already contains some adatoms and vacancies, the movement of atoms to the upper level might lead to less energy cost in terms of broken dimers. This reduction in energy for a rougher surface configuration then leads to an avalanche effect: rough surface  $\rightarrow$  lower energy cost for roughening  $\rightarrow$  rougher surface, which could explain the sharpness of the phase transition. Then, close to the end of the transition, the number of surviving dimers becomes so small that they do not form a connected reconstructed network over the surface. Then these unconnected domains show up in the sharp increase in the width of the half-order reflections just above  $T_c$ .

### 6.3 X-RAY SCATTERING FROM A VICINAL Ge(001) SURFACE

#### 6.3.1 INTRODUCTION

Vicinal Ge and Si surfaces are of significant interest, mainly because of the possibility of growing highly ordered layers of III-V and/or alloy semiconductor structures on such substrates. Also, a single layer step results in an anti-phase domain of the reconstruction whereas a bilayer step results in a coherent domain. Thus by using samples with bilayer steps, it has been shown that single domain (2x1) reconstructions can be produced with dimer bonds oriented parallel to the steps (Kaplan

Ge (001)

1x2+2x1 reconstruction

E = 12.00 keV

$\Psi = 0.00^\circ$

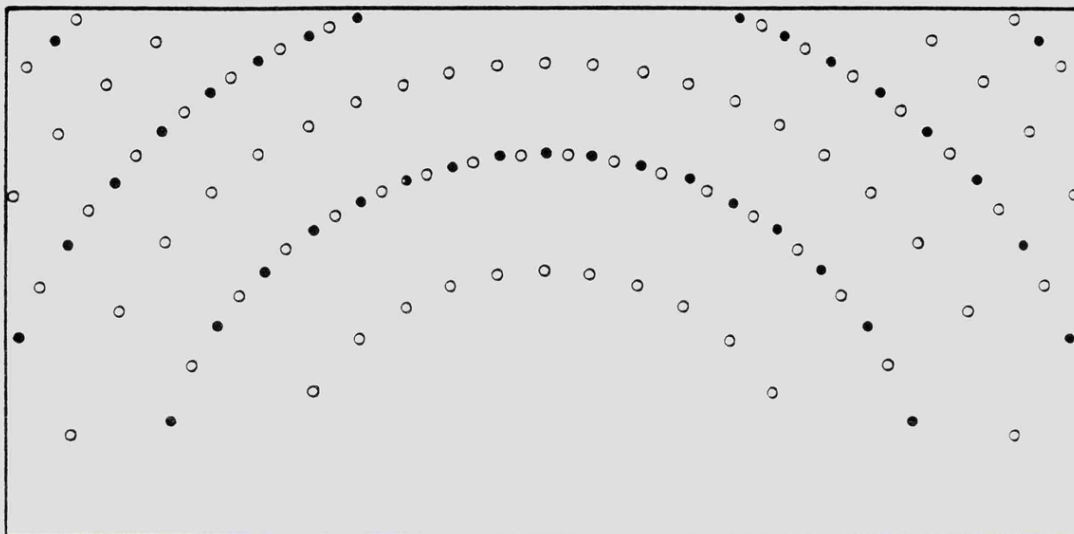
Azimuth =  $0.0^\circ$

$a_1 = 4.0005 \text{ \AA}$

$a_2 = 4.0005 \text{ \AA}$

$\alpha = 90.00^\circ$

Screen = 30.0 cm



Ge (001)

2x1+1x2 reconstruction

E = 12.00 keV

$\Psi = 0.00^\circ$

Azimuth =  $45.0^\circ$

$a_1 = 4.0005 \text{ \AA}$

$a_2 = 4.0005 \text{ \AA}$

$\alpha = 90.00^\circ$

Screen = 30.0 cm

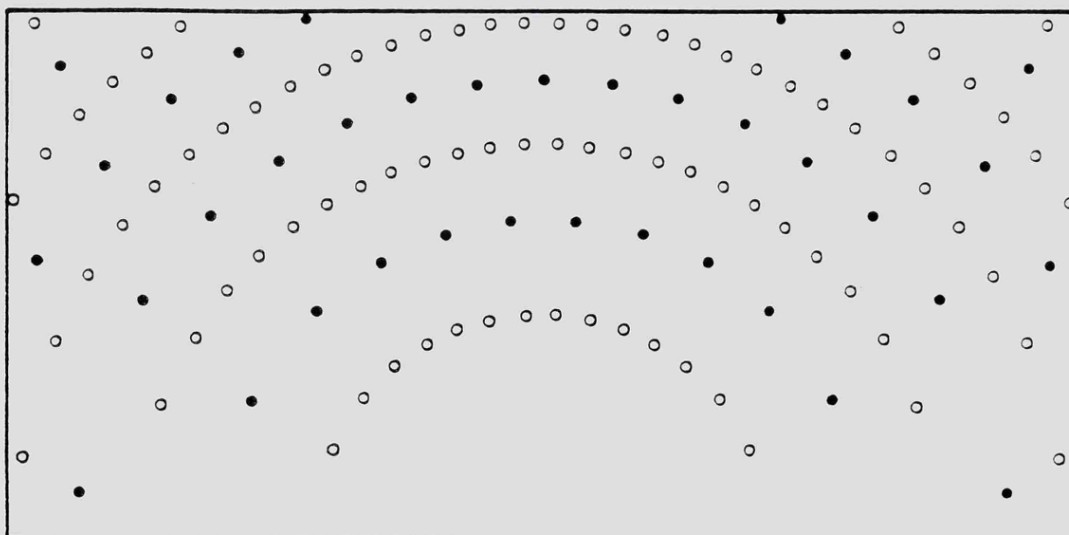


Figure (6.9) Calculated RHEED patterns for Ge(001) in the (0, 1) azimuth (top), and (1, 1) azimuth (bottom).

Plate (6.1) RHEED patterns obtained from the vicinal Ge(001) surface. Top photograph is in the (0, 1) azimuth (normal to the steps), and the bottom photograph is in the (1, 1) azimuth.

1980), although single domain reconstructions on nominally flat samples have been produced with high temperature annealing (Sakamoto and Hashiguchi 1986).

Low energy electron diffraction (LEED) studies of surfaces with miscuts in excess of  $3^\circ$  towards the [110] axis have shown the presence of double layer steps. For Si(001) and Ge(001) single domain (2x1) reconstructions results have been consistent with dimer bonds oriented parallel to the step edges (Kaplan 1980, Olshanetsky et al 1977). Similar results have been found on Si(001) using transmission electron microscopy (TEM, Nakayama et al, 1987), and scanning tunneling microscopy (STM, Wierenga et al, 1987). For non-vicinal (001) surfaces and surfaces oriented towards the [100] axis, single layer steps have been found. An explanation of this tendency in Silicon has been given by Chadi (1987), who calculated the formation energies per unit length for different configurations of single (S) and double (D) layer steps where the dimerization axes on the upper terrace were perpendicular (subscript A) or parallel (subscript B) using a semi-empirical tight binding calculation (see figure (6.12)). Chadi showed that a  $D_B$  type double step is energetically more favourable than two single steps  $S_A$ ,  $S_B$  on surfaces misoriented towards the [110] or [110] because of rebonding of atoms on the lower edge. Aspnes and Ihm (1986), and Gadiyak et al (1985, for Ge) agreed with the basic conclusions of Chadi although the precise structure of the steps considered was different.

### 6.3.2 RESULTS

The sample used was 8x10x1.5mm Ge(001) crystal nominally miscut by  $1.5^\circ$  at Phillips Research Laboratories, Eindhoven, The Netherlands. After repeated cycles of Argon bombardment (800eV,  $1\mu\text{A}$ ) and annealing (983K, 2 hours) a sharp RHEED pattern containing both 2x1 and 1x2 superlattice

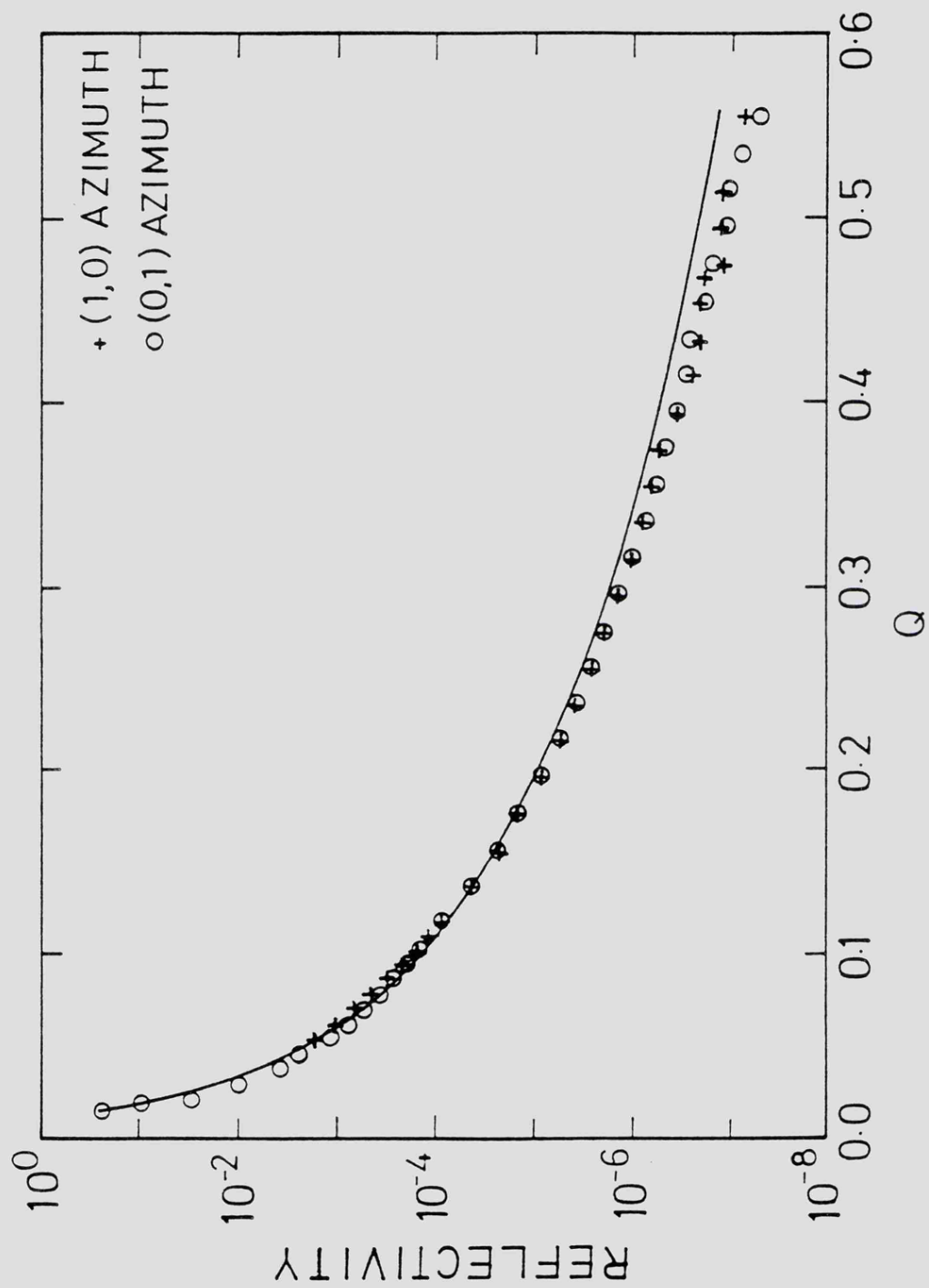


Figure (6.10) (0, 0, 1) reflectivity scans both normal and parallel to the steps on Ge(001). The solid line is the Fresnel reflectivity calculated using equation (6.6).



reflections. Figure (6.9) shows calculated RHEED patterns for Ge(001) in both [100] and [110] azimuths showing both superlattice domains. Plate (6.1) is a photograph of RHEED patterns obtained for the same azimuths as calculated in figure (6.9); note that some of the integer order spots are split into doublets in the top photograph as has been described by Ellis and Schwoebel (1968) and Henzler (1970,1982). After alignment of the sample with X-ray diffraction from bulk Bragg peaks, the miscut in the crystal was measured to be  $1.34 \pm 0.02^\circ$  away from the bulk [001] axis towards the bulk [110] axis (in surface notation, the normal is oriented in the (h00) plane with steps parallel to the [100] axis). Reflectivity scans along axes both parallel and perpendicular to the step edges are shown in figure (6.10) along with the calculated Fresnel reflectivity for a perfectly flat surface. By using equation (6.7), an rms height deviation of the surface of  $0.9 \pm 0.2\text{\AA}$  has been obtained for both orientations, indicating flat terraces between step edges (see figure (6.11)).

Figure (6.14) shows k-scans at different l values for the (0 2 l) rod (bulk (220) reflection) plotted on a semi-log scale. With increasing l there is a rapid reduction of the integrated intensity as is expected due to the termination of the surface, and a satellite peak develops. Diffraction from stepped surfaces has been treated in detail elsewhere (see Henzler (1970),(1982), Ellis and Schwoebel (1968) and Pukite et al (1985)), but one can understand the origin of the satellite peak by consideration of a one dimensional regular stepped array. If the terrace length between steps is  $t = M\mathbf{a}$ , with M integer and  $\mathbf{a}$  the primitive lattice vector and the step height  $\mathbf{d}$  then an arbitrary vector along the step array will be given by:-

$$\mathbf{b} = M\mathbf{a} + \mathbf{d}$$

# Double layer steps on Ge (001)

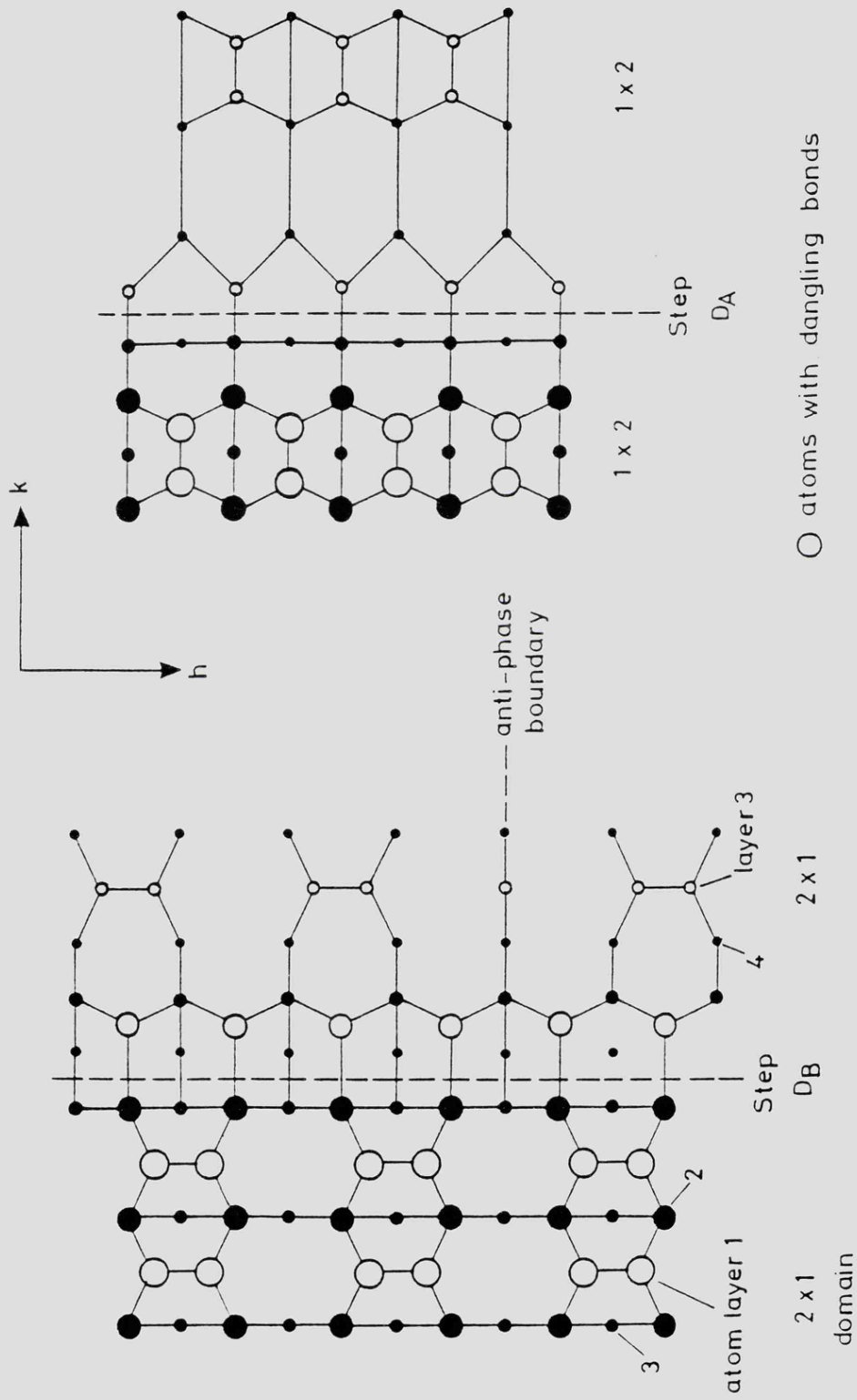


Figure (6.12) Schematic diagram showing the double layer steps considered by Chadi (1987).

# Stepped Ge(001) 1x2

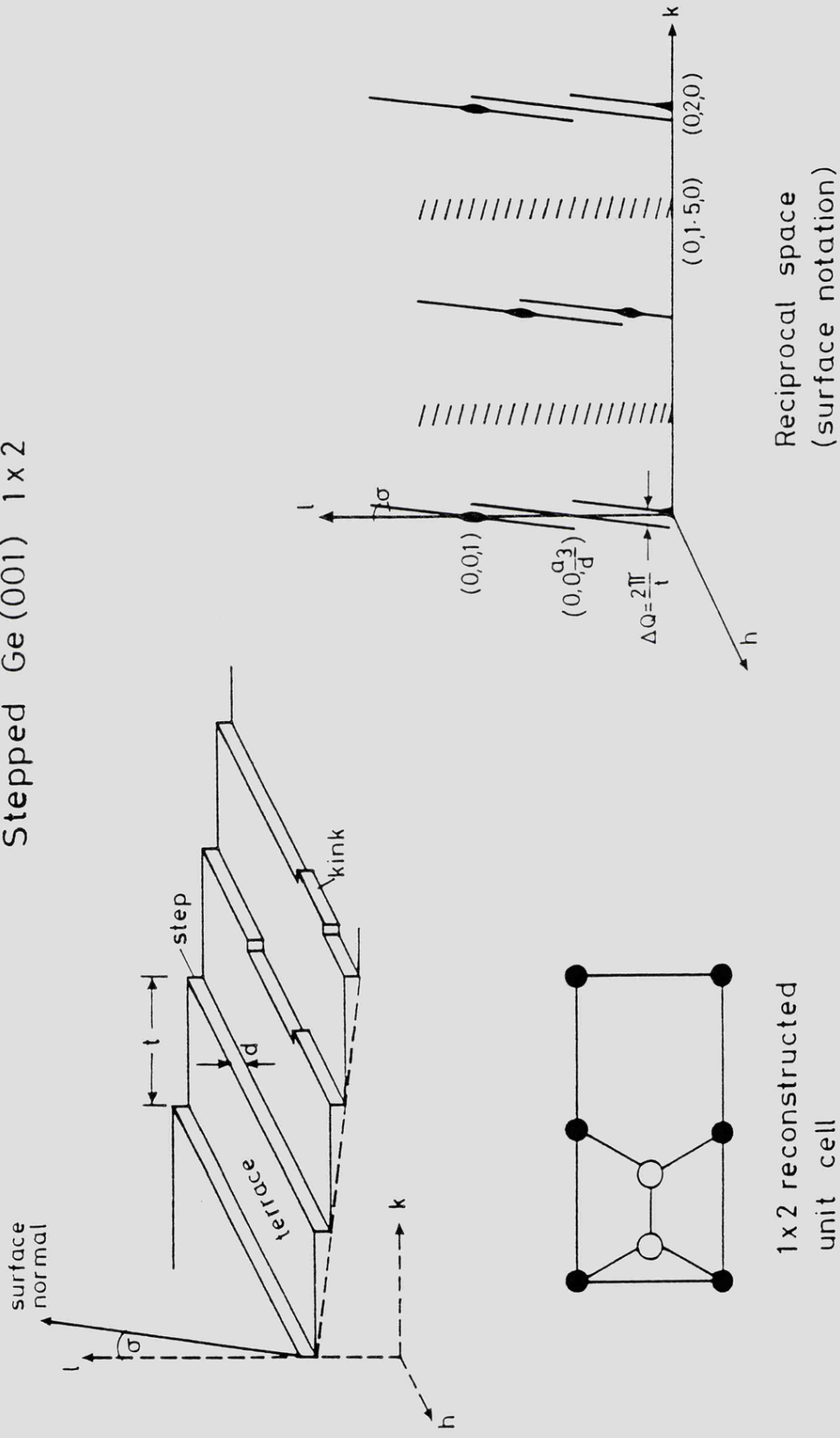


Figure (6.13) Schematic diagram of a vicinal Ge(001) surface, both in real space and reciprocal space.

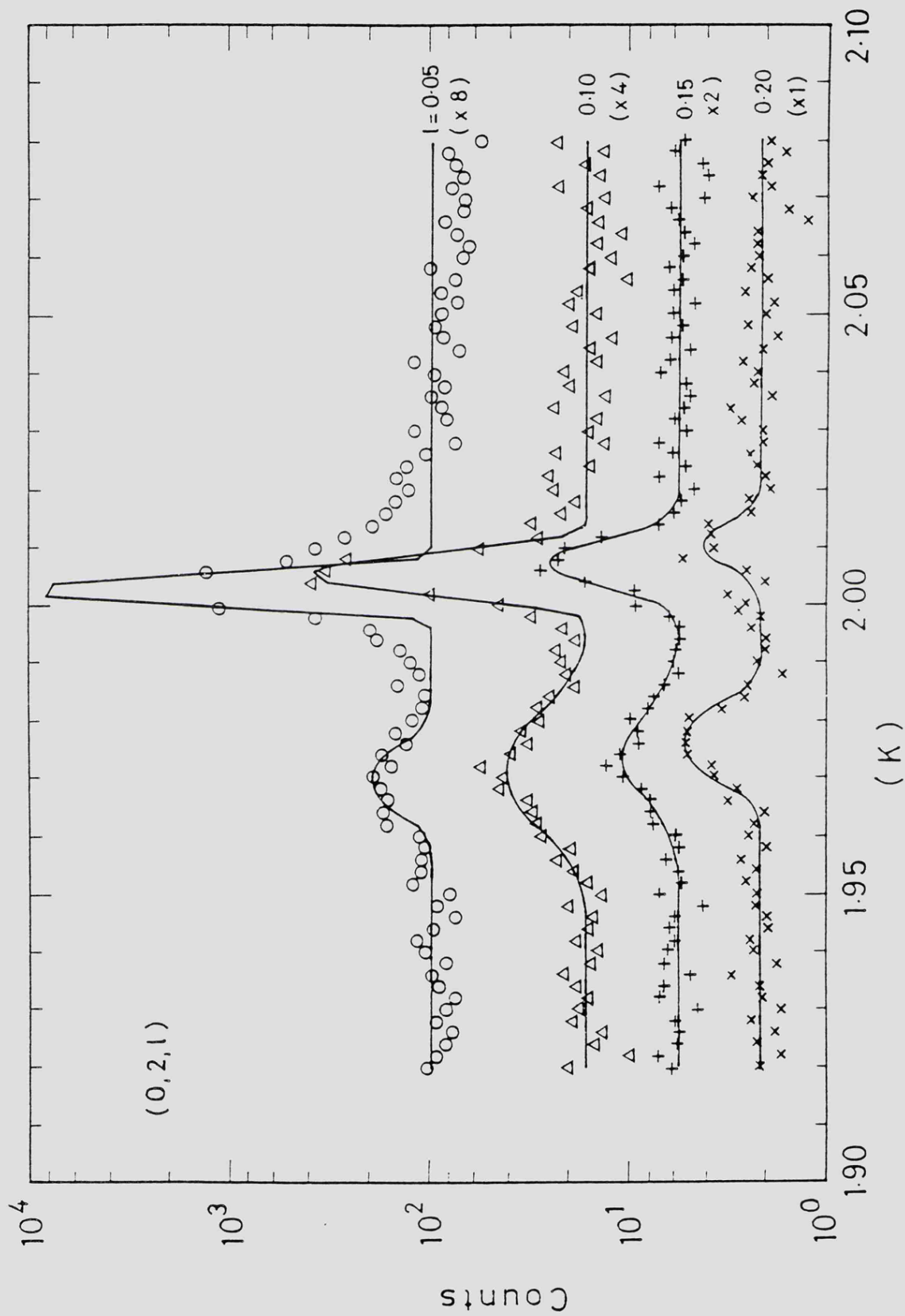


Figure (6.14) k-scans of the (0, 2, 1) truncation rod at various values of  $l$ . The scans show the bulk Bragg peak and its satellite due to the steps on the surface.

and any position on the step array can be denoted by vector  $\underline{r}$  where:-

$$\underline{r} = m\underline{a} + n\underline{b} \quad m, n \text{ integer}$$

The diffracted electric field amplitude is then given by:-

$$E \sim \sum \exp -i\underline{Q} \cdot \underline{r} \quad - (6.14)$$

$$= \sum_{m=0}^{M-1} \exp -i\underline{Q} \cdot m\underline{a} \sum_{n=0}^{N-1} \exp -i\underline{Q} \cdot n\underline{b}$$

$$\therefore EE^* \sim \frac{\sin^2(\frac{1}{2}\underline{Q} \cdot M\underline{a})}{\sin^2(\frac{1}{2}\underline{Q} \cdot \underline{a})} \times \frac{\sin^2(\frac{1}{2}\underline{Q} \cdot N\underline{b})}{\sin^2(\frac{1}{2}\underline{Q} \cdot \underline{b})} \quad - (6.15)$$

Then, letting  $\underline{Q} \cdot \underline{a} = 2\pi h$  and  $\underline{Q} \cdot \underline{b} = \underline{Q} \cdot (M\underline{a} + \underline{d}) = 2\pi(Mh+1)$ , the diffracted intensity is given by:-

$$I \sim \frac{\sin^2 \pi h M}{\sin^2 \pi h} \times \frac{\sin^2 \pi (Mh+1) N}{\sin^2 \pi (Mh+1)} \quad - (6.16)$$

The left hand term in the above equation is maximum for  $h = \text{integer}$ , whereas the right hand term is maximum for  $(Mh+1) = \text{integer}$ . The left hand term is an envelope function of  $\text{HWHM} = 0.94/2M$  which is multiplied with the right hand term which corresponds to a maximum of  $N^2$  when  $Mh+1$  is integer such that one will see one or two satellite peaks depending on the value of  $1$  (see figure (6.13)). Thus the number of unit cells  $M$  on the terrace is given by the separation of the satellite from the bulk Bragg peak in reciprocal space is given by:-

$$\Delta k = 1/M \quad - (6.17)$$

where  $k$  is in reciprocal lattice units. Reference to figure (6.14) in which the x-axis is on a scale of  $k$  gives:-

$$M = 29.5 \pm 2.2$$

or  $t = 118.0 \pm 8.6\text{\AA}$

where  $t$  is the terrace length as shown in figure (6.13). From the miscut angle of  $1.34 \pm 0.02^\circ$  the mean step height is therefore obtained to be:-

$$d = 2.76 \pm 0.25\text{\AA}$$

This compares very favourably with the value of  $2.829\text{\AA}$  which is the value of a double layer step expected from the bulk Ge lattice parameter, and agrees within error with the value of  $2.68\text{\AA}$  obtained for step heights on Ge samples with larger miscuts by Olshanetsky et al (1977) using LEED. The movement of the peaks in  $k$  with increasing  $l$  in figure (6.14) reflect the alignment of the rod to the surface normal rather than the crystallographic axis.

RHEED study of the vicinal surface indicated the presence of both  $2 \times 1$  and  $1 \times 2$  reconstructed domains, see plate (6.1), and the X-ray scattering pattern revealed the presence of both  $1.5, 0, 1$  and  $0, 1.5, 1$  rods corresponding to both such domains. The integrated intensities of both reflections indicated that both domains were equal in area to  $\sim 10\%$ .

Figure (6.15) shows profile measurements of the  $(0, 1.5)$  fractional order reflection made at  $l = 0.05$  by scanning parallel to both  $h$  and  $k$ . If the size of the domains does not vary significantly one can approximate the quotient from equation (2.36) such that:-

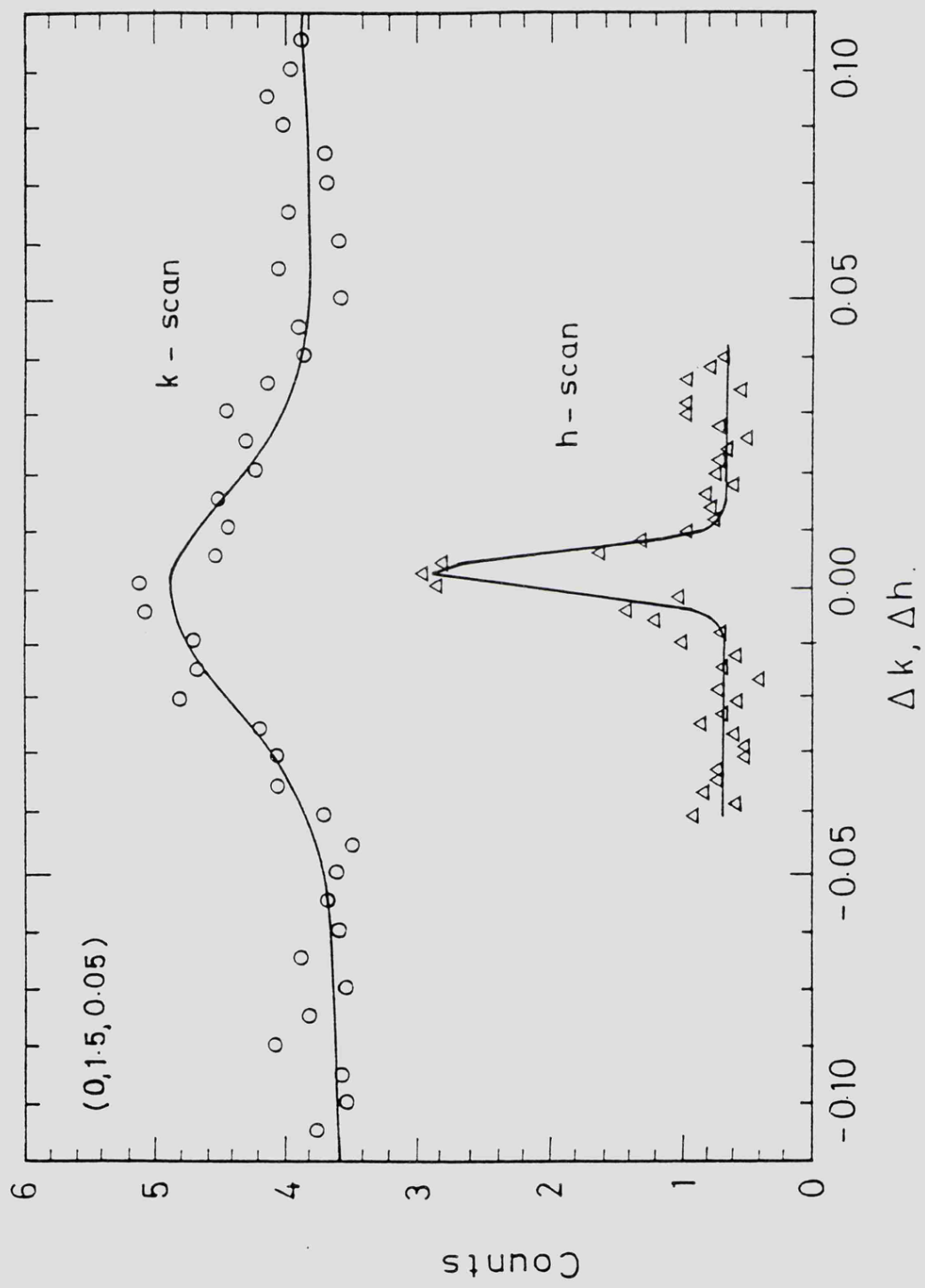


Figure (6.15) Reciprocal space scans across the  $(0, 3/2, 0.05)$  fractional order reflection. The difference in the HWHM of the scans in h and k reflect the variation in domain size in each direction.

$$\frac{\sin^2 Nx}{\sin^2 x} \rightarrow N^2 e^{-(Nx)^2/\pi} \quad - (6.18)$$

which is a gaussian such that its HWHM is given by (see Warren (1969)):-

$$\text{HWHM} = \frac{0.94 \pi}{d b_2} \quad - (6.19)$$

Where the HWHM is in units of h or k,  $b_2$  is a reciprocal lattice parameter and d is the domain size in real space in Å. From figure (6.15) it can be seen that the k-scan (normal to the steps) is much broader than the h-scan (parallel to the steps), indicating a smaller domain size normal to the steps. The solid line curves in the figure are gaussian fits to the data and after correction for the instrumental resolution function the following domain sizes were obtained for both 2x1 and 1x2 reconstructions, both perpendicular and parallel to the steps:-

Reflection	Scan	d(Å)
1.5 0 0.05	k	116.0 ± 10.6
1.5 0 0.05	h	531 ± 120
0 1.5 0.05	k	105.3 ± 16.0
0 1.5 0.05	h	1415 ± 380

As can be seen, the domain sizes parallel to the step edges are much larger than those in the k direction. The domain sizes in the k direction, perpendicular to the step edges, are in agreement within error with the terrace length  $d = 118.0 \pm 8.6\text{Å}$  indicating that the domains extend almost across the whole of the terraces. In the h direction, or parallel to the steps, it can be seen that the domain sizes are much larger in than in the k direction, with the 1x2 domain being significantly larger than the 2x1.

### 6.3.3 DISCUSSION

Previous experiments on vicinal surfaces of both Si and Ge have shown that for miscuts in excess of  $3^\circ$  in the [110] axis exhibit double layer steps with single domains of 2x1 reconstruction (for example, Kaplan 1980, Olshanetsky 1977). Furthermore, this has been predicted theoretically (Chadi 1987) and it has also been shown that dimers immediately adjacent to steps align themselves parallel to those steps (type B dimers). Thus if domains extended over the whole of the terrace it would be expected that only 2x1 domains would be present on the surface whereas in fact both 2x1 and 1x2 domains are seen.

Thus although the terrace length limits the length of the reconstructed domains, with those domains extending almost totally across the whole of the terraces, the steps do not influence the orientation of the domains. As type A dimers are less likely to occur at step edges, it must be assumed that when the dimers are being created, after annealing of the sample, the 1x2 domains must be formed initially in the centre of the terraces, with subsequent growth of the domains from these sites and that the terraces are sufficiently large enough in size to allow this mechanism to take place. The fractional order scans also show that the 1x2 domain dimension perpendicular to the step, although limited by the terrace size, is slightly smaller than the 2x1 domain indicating that close to the steps type B dimers are preferred.

In the direction parallel to the steps the 1x2 domain is seen to be much larger in size than that of the 2x1 domain. Figure (6.12) shows the two types of double layer step,  $D_A$  and  $D_B$ , and by considering bonding in the direction parallel to the steps it can be seen that anti-phase domain boundaries are more likely to occur in the 2x1 domain rather than the 1x2

domain. It is the formation of these anti-phase domain boundaries that is proposed to reflect the relative difference in size of the domains parallel to the steps.

#### 6.4 SUMMARY

A new reversible surface phase transition has been measured at a transition temperature of  $T_c = 954 \pm 7\text{K}$  on Ge(001). The transition has been proposed to be due to the formation of vacancies by atoms in the surface jumping out of the surface to form adatoms. A three level model has been used to describe the reflectivity data and the results are in agreement with those derived from the Monte-Carlo simulation, in accordance with all three levels being almost equally occupied after the transition. A further roughening event that takes place at  $\sim 1010\text{K}$  is irreversible and attributed to the formation of steps, the surface only being recovered on repeating the initial cleaning cycle. It should be noted that the cleaning cycle used contains a short anneal at a temperature just above  $T_c$ , followed by a slow cool through the transition. In contrast other workers who have annealed at temperatures lower than  $T_c$ , have found it necessary to anneal for much longer periods ( $\sim 2\text{hrs}$ ) before a surface of sufficient quality can be achieved (for example, Grey et al, 1988). Thus it is probable that for best results, it is preferable to anneal at a temperature of  $954\text{K} < T < 1010\text{K}$  with a slow cool through the transition to achieve a flat surface.

X-ray scattering from the vicinal Ge(001) surface indicate the presence of mainly double layer steps, in agreement with previous theoretical and experimental results. Both  $2 \times 1$  and  $1 \times 2$  domains are found to coexist on the surface, explained by the length of the terraces between steps. The relative difference in domain sizes in a direction parallel to the steps is explained in terms of the formation of

anti-phase domain boundaries due to dangling bonds left on the surface after dimerisation. The results emphasise the high resolution of X-ray diffraction for this type of experiment.

## CHAPTER 7

### SUMMARY AND SUGGESTIONS FOR FURTHER WORK

- 7.1 Introduction
- 7.2 Overlayer Growth
- 7.3 Polarised Neutron Reflection Results
- 7.4 X-ray Scattering Results
- 7.5 Suggestions For Future Work

## CHAPTER 7

### SUMMARY AND SUGGESTIONS FOR FURTHER WORK

#### 7.1 INTRODUCTION

This chapter makes a brief summary of the data presented in the preceding three chapters. The results are discussed in the context of previous results by other authors on similar systems. For a more in depth discussion of each studied system the reader is advised to read the appropriate chapter where more detailed analysis is presented.

Section 7.2 deals with the study of the epitaxial growth of Cr and Co on Ag(001). The magnetic studies of Ag/Cr/Ag(001) and Ag/Fe/Ag(001) sandwich structures with polarised neutron diffraction are discussed in section 7.3, with the X-ray scattering measurements from Ge(001) surfaces summarised in section 7.4. A further section, 7.5, deals with the likely direction of any further studies in each of the three types of experiment undertaken.

#### 7.2 OVERLAYER GROWTH

As-t and LEED studies have been performed on the initial stages of epitaxy of Cr on Ag(001). The results obtained are in good agreement with previous work on the same system undertaken by Newstead et al (1987). It was therefore decided to use the same coverage calibration used by Newstead et al, whereby deposition to the first break in the As-t plot at  $I/I_0=0.80$  corresponds to 0.33ML coverage.

Further measurements of polar angle dependence of the emitted Auger electron intensity of both the clean substrate and the Cr overlayers have been undertaken in order to understand the mode of growth and structure

of the first few Cr layers. Scans from the clean Ag substrate are in good agreement with what would be expected from a bulk FCC crystal. Scans from thick Cr layers however indicate that the overlayers are ordered in the BCC phase but with a  $45^\circ$  rotation of the BCC lattice relative to the FCC Ag lattice. Consideration of the Ag lattice nearest-neighbour distance and Cr lattice parameter reveal that this involves a 0.2% lateral expansion of the Cr lattice. Such behaviour has previously been proposed for Cr adsorbed on Au(001), which has a similar structure to Ag, by Zajac et al (1985) but other studies on the same system (Brodsky, 1981 and Durbin et al, 1988) have indicated FCC growth of Cr involving a lateral expansion of the Cr lattice of 41%.

The polar angle Auger scans have also been discussed in terms of the growth mode of Cr/Ag(001) as proposed by Newstead et al. In their electron spectroscopy studies, Newstead et al proposed that the Cr grows as single layer platelets to the first break in the As-t plot at 0.33ML, with bilayer formation then continuing until the completion of the second monolayer followed by island growth. Polar scans at low Cr coverage ( $<0.33\text{ML}$ ) support the view of single layer platelets as there is an absence of any intensity peaks in the data. However, by 1.3ML, it is clear that third Cr layers have formed indicating the absence of a complete Cr bilayer as previously predicted. It is impossible to say whether this corresponds to island formation immediately after the first break in the As-t plot.

Further As-t and LEED measurements have been made on Co/Ag(001), a system not previously studied. The As-t data shows an initial exponential decay followed by a series of straight lines defined by three clear breaks which are equally spaced. It is proposed that the Co initially diffuses into the Ag substrate to form a substitutional alloy until

$I/I_0=0.77$  in the As-t plot. Further deposition of Co is suggested to then grow layer-by-layer until 3ML is adsorbed after which island formation occurs as supported by the degradation of the  $p(1 \times 1)$  LEED pattern.

Polar angle dependence of Auger electron intensity from both the clean Ag substrate and Co overlayers support the proposed growth model. Polar scans on the clean Ag give an FCC signature as expected, but scans of 0.5ML Co layers suggest either island formation or a surface Ag-Co alloy which does not extend more than two layers into the substrate lattice. Comparison with the As-t and LEED data indicate that the more likely occurrence is interdiffusion, this being a similar growth mechanism to that proposed by Hanf et al (1987) for Cr/Au(001). Moreover, the Co layers have been shown to stabilise in the FCC phase, in contrast to other 3d transition metals such as Fe and Cr, which have been shown to grow epitaxially in the BCC phase on Ag(001). There is no means of estimating the FCC lattice constant of the Co layers to see if it has stabilised either in its bulk FCC phase with lattice constant  $3.56\text{\AA}$ , or whether there is a lateral expansion of the Co by 14% to match the FCC Ag lattice. Possible shifts in the position of forward scattered peaks may suggest a vertical compression of the Co lattice, indicating an in plane expansion, but no accurate estimate of the compression can be made at present.

### 7.3 POLARISED NEUTRON REFLECTION RESULTS

PNR measurements on Ag/Cr/Ag(001) sandwich structures indicate the presence of in-plane ferromagnetism with a greatly enhanced magnetic moment for single atom thicknesses of Cr (0.33ML). No accurate estimate for the magnetic moment can be made but the obtained value of  $5.1 \pm 2.5 \mu_B$  is consistent with previous calculated values (Fu et al, 1985). Thicker Cr layers are shown to have no in plane ferromagnetism and are proposed

to have either perpendicular spin anisotropy or to be antiferromagnetic. Comparison to theoretical calculations of layer dependent magnetic moments (Fu and Freeman, 1986 and Hirashita et al, 1981) shows that the 3.3ML Cr sample cannot be antiferromagnetically coupled in-plane with the spins being aligned normal to the surface.

LEED and As-t measurements have been used to prepare an Ag/Fe/Ag(001) sandwich structure with an Ag overlayer thickness of 100Å and a 8ML thickness of Fe. It has been shown that the Fe layer is well ordered and is assumed to be in the BCC phase. PNR measurements indicate a significantly reduced ferromagnetic moment of  $1.0 \pm 0.15\mu_B$  in contrast with theoretical predictions of an enhanced moment for this system (Fu et al, 1985 and Richter et al, 1985). It also contradicts theoretical calculations by Bagayoko and Calloway (1983) who have shown the magnetic moment to increase with increasing lattice parameter for BCC Fe. The in-plane ferromagnetism is consistent with previous SMOKE measurements on Fe layers of similar thickness and agrees with the calculations of Wang et al (1985) who proposed that ferromagnetic ordering is the most energetically stable configuration for BCC Fe. In order to show that the applied field of 8000e used in the PNR experiment saturated the Fe layers in plane SMOKE measurements have been performed on the sandwich structure. The results prove that the Fe layers are saturated in-plane at a field much less than 8000e but cannot be saturated in the plane normal to the Fe layers. No temperature dependence of the measured moment was detected up to 300K indicating no reduced Curie temperature, which suggests bulk-like behaviour.

#### 7.4 X-RAY SCATTERING RESULTS

Measurements from a flat Ge(001) surface show a surface roughening transition at  $954 \pm 7K$  not previously observed. Data from fractional

order rods and specular reflectivity are in good agreement about the value of the transition temperature  $T_c$ . The data precludes many roughening mechanisms such as step formation and surface melting but is consistent with adatom-vacancy creation. The data has therefore been interpreted in terms of a three level model to describe the proposed roughening mechanism. Fits to reflectivity scans are in good agreement with values for the number of adatom-vacancy pairs obtained from a simple Monte-Carlo program. An estimate of the activation energy needed to break the dimer bonds on the Ge surface has thus been made of  $0.41 \pm 0.05$ .

Further measurements from a vicinal Ge(001) surface reveal the presence of double layer steps which have previously been predicted to be the most stable type of step (Chadi, 1987). Scans across fractional order rods show that perpendicular to the steps the domain sizes are limited by the terrace length between steps. Parallel to the steps the domains are much larger, as expected but with the 1x2 domain having greater dimension than the 2x1 domain. This is attributed to the formation of antiphase domain boundaries in the 2x1 domain. Measurement of the fractional order integrated intensities reveal that the domains are of approximately the same area indicating that the terraces between steps are large enough to prevent the creation of a single domain as has previously been observed with LEED (Kaplan, 1980).

#### 7.5 SUGGESTIONS FOR FUTURE WORK

The forward scattering of electrons has been shown to be a useful technique in the study of the initial stages of epitaxy. A useful system to study would be the Cr/Au(001) as it should be possible to determine whether there is an interfacial Au-Cr alloy or not. As has been previously described, more accurate measurement of the positions of forward scattered intensity peaks should prove invaluable in determining

lateral strain and compression of adsorbed overlayers. More accurate measurements on the Co/Ag(001) system need to be performed to properly understand the true phase of the Co layers. A more distant extension of the work would be to include a complete photoelectron diffraction approach with calculated photoemitted intensities. The technique is becoming more widely used in the study of surfaces and adsorbed layers (see Fadley, 1984 and references therein).

The most obvious experiment that can next be undertaken using PNR would be a single monolayer of Fe on Ag as there is some dispute as to the spin-alignment in the Fe layer. Preliminary results on the Co/Ag(001) system indicate a significantly enhanced moment for 2.0ML of Co (Bland et al, 1989) which could indicate that the Co layers are indeed laterally strained. Rare earth metals also provide a new source of interest as the unfilled 4f shell characteristic of these metals can lead to highly localised magnetic moments. Other possible areas of further work include the magnetic coupling of layered magnetic structures. Antiferromagnetic coupling between Fe layers across Cr and Au interlayers has already been suggested (Grünberg et al, 1986). The measurement of such coupling using PNR has been calculated to be easily measurable for a variety of different magnetic layered structures (Bland and Johnson, 1989). The growth of magnetic layers on optically flat substrates such as semiconductor wafers also provides an opportunity to improve the signal to noise ratio of the collected neutron reflection. A preliminary study of neutron reflection from a GaAs wafer has shown that the reflected intensity is easily measurable up to  $3q_c$  and beyond, a factor of two better than has so far been achieved from metal samples.

The possible experiments that may be further performed with surface X-ray diffraction is vast. Roughening, surface melting, structure

analysis and X-ray growth oscillations are all experiments that have been already undertaken using the technique. The extension of these experiments to other systems provides a rich source of work yet to be exploited. Furthermore, although most SXRD work has until now concentrated on semiconductors, the installation of focussing optics on the SXRD beamline at Daresbury Laboratory will permit the study of metal surfaces and the growth of metal adsorbates on such substrates.

## REFERENCES

- Als-Neilsen J and Dietrich O W 1967, Phys Rev 153, 706.
- Als-Neilsen J 1985, Z Phys B61, 411.
- Als-Neilsen J in 'Handbook on Synchrotron Radiation, Vol. 3', North Holland, Amsterdam.
- Andrews S R and Cowley R A 1985, J Phys C 18, 6427.
- Araya-Pochet J, Ballentine C A and Erskine J L 1988, Phys Rev B 38, 7846.
- Ashcroft N W and Mermin N D 1976, 'Solid State Physics', Holt-Saunders.
- Aspnes D E and Ihm J 1986, Phys Rev Letts 57, 3054.
- Auger P 1925, J Phys Radium 6.
- Bacon G E 1961, Acta Cryst 14, 823.
- Bagayoko D and Callaway J 1983, Phys Rev B 28, 5419.
- Barthès M-G and Rolland A 1981, Thin Solid Films 76, 45.
- Bauer E 1987 in 'Structure And Dynamics Of Surfaces Vol III', Edited By W Schommens and P von Blackenhagen, Springer-Verlag.
- Binns C, Norris C, Williams G P, Barthès M-G and Padmore H A 1986, Phys Rev B 34, 8221.
- Bland J A C, Pescia D and Willis R F 1987, Phys Rev Letts 58, 1244.
- Bland J A C, Padgett M J, Butcher R J and Bett N 1989, J Phys E Rev Sci Instrum 22, 308.
- Bland J A C, Johnson A D, Norris C and Lauter H J 1989, to be published.
- Bland J A C and Johnson A D 1989, to be published.
- Blügel S, Weinert M and Dederichs P H 1988, Phys Rev Letts 60, 1077.
- Blügel S, Pescia D and Dederichs P H 1989, Phys Rev B 39, 1392.
- Born M and Wolf E W, 'Principles Of Optics' 1975, Pergamon Press Oxford.
- Brodsky M B 1981, J Appl Phys 52, 1665.
- Brodsky M B, Marikar P, Friddle R J, Singer L and Sowers C H 1982, Solid State Comm 42, 675.
- Brodsky M B 1983, J Magn Magn Mater 35, 99.
- Brodsky M B, Sill LR and Sowers C H 1986, J Magn Magn Mater 54-57, 779.
- Bullock E L and Fadley C S 1985, Phys Rev B 31, 1212.
- Burton W K, Cabrera N and Frank F C 1951, Philos Trans R Soc London Ser A 243, 299.

Carbone C and Alvarado S F 1987, Phys Rev B 36, 2433.

Chadi D J 1979, Phys Rev Letts 43, 43.

Chadi D J 1987, Phys Rev Letts 59, 1691.

Chambers S A, Anderson S B and Weaver J H 1984, Phys Rev B 32, 4872.

Chambers S C, Chen H W, Vitomirov I M, Anderson S B and Weaver J H 1986, Phys Rev B 33, 8810.

Chambers S A, Anderson S B, Chen H-W and Weaver J H 1987, Phys Rev B 35, 2592.

Charles A and Jackson D C 1975, Phil Mag 31, 1357.

Clarke A, Jennings G, Willis R F, Rous P J and Pendry J B 1987, Surf Sci 187, 327.

Connell G A N 1986, J Magn Magn Mater 54, 1561.

Davis L E, MacDonald N C, Palmberg P W, Riach G E and Weber R E 1976, 'Handbook Of Auger Electron Spectroscopy 2nd Edition' Physical Electronics Inc, Eden Prairie Minn.

Durbin S M, Berman L E, Batterman B W, Brodsky M B and Hamaker H C 1988, Phys Rev B 37, 6672.

Dürr W, Taborelli M, Paul O, Germer R, Gudat W, Pescia D and Landolt M 1989, Phys Rev Letts 62, 206.

Egelhoff W F 1984, Phys Rev B 30, 1052.

Eisenberger P and Marra W C 1981, Phys Rev Letts 46, 1081.

Ellis W C and Greiner E S 1941, Trans Am Soc Met 29, 415.

Ellis W P and Schwoebel R L 1968, Surf Sci 11, 82.

Fadley C S 1984, Prog Surf Sci 16, 275.

Fawcett E 1988, Rev Mod Phys 60, 209.

Feidenhans'l R 1986, PhD Thesis, Risø National Laboratory, Denmark.

Felcher G P 1981, Phys Rev Letts 24, 1595.

Felcher G P, Felici R, Kampwirth R T and Gray K E 1985, J Appl Phys 57, 3789.

Ferguson P E 1978, J Appl Phys 49, 2203.

Freeman A J and Fu C L 1987, J Appl Phys 61, 3356.

Frenken J W M and Van Der Veen J F 1985, Phys Rev Letts 54, 134.

Fu C L and Freeman A J 1986, Phys Rev B 33, 1755.

Fu C L, Freeman A J and Oguchi T 1985, Phys Rev Letts 54, 2700.

- Fuoss P H and Robinson I K 1984, Nucl Instr and Meth 222, 171.
- Gadiyak G V, Morokov Y N, Kushkova A S, Repinskii S M and Shklyayev A A 1985, Phys Chem Mech Surfaces 3, 1978.
- Gardiner M K 1983, PhD Thesis, Leicester University.
- Gay J G and Richter R 1986, Phys Rev Letts 56, 2728.
- Gibbs D, private communication.
- Goldberg M L and Seitz F 1947, Phys Rev 71, 294.
- Gonzalez L, Miranda R, Salmerón, Vergés J A and Yndurain F 1981, Phys Rev B 24, 3245.
- Grey F, Johnson R L, Skov Pedersen J, Feidenhans'l R and Nielsen M 1988, The Structure Of Surfaces II, Springer Series In Surface Sciences 11, Springer-Verlag.
- Grünberg P, Schreiber R, Pang Y, Brodsky M B and Sowers H 1986, Phys Rev Letts 57, 2442.
- Hanf M C, Pirri C, Peruchetti J C, Bolmont D and Gewinner G 1987, Phys Rev B 36, 4487.
- Hanf M C, Pirri C, Peruchetti J C, Bolmont D and Gewinner G 1989, Phys Rev B 39, 1546.
- Harris L A 1968, J Appl Phys 39, 1419.
- Hayter J B, Penfold J and Williams W G 1978, J Phys E (Sci Instr) 11, 454.
- Held G A, Jordan-Sweet J L, Horn P M, Mak A and Birgeneau R J 1987, Phys Rev Letts 59, 2075.
- Henzler M 1970, Surf Sci 19, 159.
- Henzler M 1982, Appl Surf Sci 11/12, 450.
- Hezaveh A A, Jennings G, Pescia D, Willis R F, Prince K, Surman M and Bradshaw A 1986, Solid State Commun 57, 329.
- Hirashita N, Yokoyama G, Kambara T and Gondaira K I 1981, J Phys F 11, 2371.
- Hughes D J 1954, 'Neutron Optics', Interscience New York.
- Idzerda Y U, Elam W T, Jonker B T and Prinz G A 1989, Phys Rev Letts 62, 2480.
- Ihm J, Lee D H, Joannopoulos J D and Xiong J J 1983, Phys Rev Letts 51, 1872.
- Johnson A D, Bland J A C, Norris C and Lauter H J 1988, J Phys C 21, L899.
- Jonker B T and Prinz G A 1986, Surf Sci 172, L568.

- Jonker B T, Walker K-H, Kisker E, Prinz G A and Carbonne C 1986, Phys Rev Letts 57, 142.
- Kaplan R 1980, Surf Sci 93, 145.
- Katayama T, Suzuki Y, Awano H, Nishihara Y and Koshizuka N 1988, Phys Rev Letts 60, 1426.
- Keune W, Halbauer R, Gonser U, Lauer J and Williamson D L 1977, J Appl Phys 48, 2976.
- Kevan S D 1985, Phys Rev B 32, 2344.
- Klebanoff L E, Robey S W, Liu G and Shirley D A 1984, Phys Rev B 30, 1048.
- Kono S, Goldberg S M, Hall N F T and Fadley C S 1978, Phys Rev Letts 41, 1831.
- Kono S, Goldberg S M, Hall N F T and Fadley C S 1980, Phys Rev B 22, 6085.
- Kubby J A, Griffith J E, Becker R S and Vickers J S 1987, Phys Rev B 36, 6079.
- Lambert W R, Trevor P L, Cardillo M J, Sakai A and Hamann D R 1987, Phys Rev B 35, 8055.
- Liu C, Moog E R and Bader S D 1988, Phys Rev Letts 60, 2422.
- Maglietta M and Zannazzi E 1978, Appl Phys 15, 409.
- 'Magnetic Properties of Low Dimensional Systems' - Springer Proceedings in Physics 14, edited by L M Falicov and J L Morán-López 1986.
- Marcus P M and Moruzzi V L 1985, Solid State Comm 55, 971.
- Marée P M J, De Jong A P, Derks J W and Van Der Veen J F 1987, Nucl Instr and Meth B28, 76.
- Marra W C, Eisenberger P and Cho A Y 1979, J Appl Phys 50, 6927.
- McRae E G and Malic R A 1987, Phys Rev Letts 58, 1437.
- McRae E G and Malic R A 1988, Phys Rev B 38, 13163.
- McRae E G, Landwehr J M, McRae J E, Gilmer G H and Grabow M H 1988, Phys Rev B 38, 13178.
- Meier F, Pescia D and Schrieber T 1982, Phys Rev Letts 48, 645.
- Mezei F 1972, Z Phys 255, 146.
- Miranda R, Chandesris D and Lecante J 1983, Surf Sci 130, 269.
- Mochrie S G J 1987, Phys Rev Letts 59, 304.
- Moog E R, Bader S D, Montano P A, Zajac G and Fleisch T H 1987, Superlattices and Microstructures 3, 435.

Nakayama T, Tanishiro Y and Takayanagi K 1987, Jap Journ Appl Phys 26, L280 and Jap Journ Appl Phys 26, L1186.

Needels M, Payne M C and Joannopoulos J D 1988, Phys Rev B 38, 5543.

Newstead D A 1987, Ph.D. Thesis, University of Leicester.

Newstead D A, Norris C, Binns C and Stephenson P C 1987, J Phys C 20, 6245.

Newstead D A, Norris C, Binns C, Johnson A D and Barthès M-G 1988, J Phys C 21, 3777.

Netzer F P and Matthew J A D 1986, Rep Prog Phys 49, 621.

Nöller H G, Polaschegg H D and Schillalies H 1974, J Elect Spect and Rel Phen 5, 705.

Norris C, Taylor J S G, Moore P R and Harris N W, to be published.

Ocko B M and Mochrie S G J 1988, Phys Rev B 38, 7378.

Olshanetsky B Z, Repinsky S M and Shklaev A A 1977, Surf Sci 69, 205.

Onsager L 1945, Phys Rev 65, 117.

Pendry J B 'Low Energy Electron Diffraction', Academic, London 1974.

Pendry J B and Gurman S J 1975, Surf Sci 49, 87.

Polaschegg H D 1974, Appl Phys 4, 63.

Polaschegg H D 1976, Appl Phys 9, 223.

Poon H C and Tong S Y 1984, Phys Rev B 30, 6211.

Prinz G A and Krebs J J 1981, Appl Phys Letts 39, 397.

Prinz G A 1985, Phys Rev Letts 54, 1051.

Pukite P R, Lent C S and Cohen P I 1985, Surf Sci 161, 39.

Richter R, Gay J G and Smith J R 1985, Phys Rev Letts 54, 2704.

Robinson I K, in 'Handbook on Synchrotron Radiation Vol. 3', North Holland, Amsterdam.

Robinson I K 1986, Phys Rev B 33, 3830.

Robinson I K, MacDowell A A, Altman M S, Estrup P J, Evans-Lutterodt K, Brock J D and Birgeneau R J 1989, Phys Rev Letts 62, 1294.

Sakamoto T and Hashiguchi G 1986, Jap Journ Appl Phys 25, L78.

Salanon B, Fabre F, Lapujoulade J and Selke W 1988, Phys Rev B 38, 7385.

Seah M P and Dench W A 1979, Surf Interface Anal 1, 2.

Schaerpf O 1975, J Phys E (Sci Instr) 8, 269.

Shirane G and Takei W J 1962, J Phys Soc Jap Suppl B111 17, 35.

Smith G C 1982, Ph.D. Thesis, University of Leicester.

Smith G C, Padmore H A and Norris C 1982, Surf Sci 119, L287.

Smith G C, Norris C and Binns C 1984, J Phys C 17, 4389.

Stampanoni M, Vaterlaus A, Aeschlimann M and Meier F 1987, Phys Rev Letts 59, 2483.

Stoyanov S and Markov I 1982, Surf Sci 116, 313.

Taylor J S G and Newstead D A 1987, J Phys E (Sci Instr) 20, 1288.

Taylor N J 1969, Rev Sci Instr 40, 792.

Teraoka Y and Kajamori J 1977, Phys Of Transition Metals, Toronto.

Thomson K A and Fadley C S 1984, J Elec Spect Rel Phen 33, 29.

Vlieg<sup>1</sup> E, Van't Ent A, De Jongh A P, Neerings H and Van Der Veen J F 1987, Nucl Instr and Meth A262, 522.

Vlieg<sup>2</sup> E, Van Der Veen J F, Macdonald J E and Miller M 1987, J Appl Cryst 20, 330.

Vlieg E 1988, PhD Thesis F.O.M. Institut, Amsterdam.

Vlieg E, Denier Van Der Gon A W, Van Der Veen J F, Macdonald J E and Norris C 1988, Phys Rev Lett 61, 2241.

Wang C S, Klein B M and Krakauer H 1985, Phys Rev Letts 54, 1852.

Warren B E 1969, 'X-ray Diffraction', Addison Wesley.

Wesner D A, Coenen F P and Bonzel H P 1986, Phys Rev B 33, 8837.

Wesner D A, Pinnig G, Coenen F P and Bonzel H P 1986, Surf Sci 178, 608.

Wierenga P E, Kubby J A and Griffith J E 1987, Phys Rev Letts 59, 2169.

Williams W G 1988, 'Polarised Neutrons', Clarendon Press Oxford.

Xu J H, Freeman A J, Jarlborg T and Brodsky M B 1984, Phys Rev B 29, 1250.

Zajac G, Bader S D and Friddle R J 1985, Phys Rev B 31, 4947.

EPITAXIAL GROWTH AND SURFACE MORPHOLOGY OF SOME  
METAL AND SEMICONDUCTOR STRUCTURES

by A.D.Johnson

ABSTRACT

Forward focussing of medium energy Auger and photoelectrons have been used along with LEED and Auger electron spectroscopy to investigate the initial stages of growth of both Cr and Co on Ag(001). Cr was found to grow epitaxially on Ag in the bcc phase up to ~2ML, in agreement with previous results. Co also grows epitaxially on Ag up to 3ML although it is proposed that the Co lattice is in the FCC phase but no comment can be made as to whether the overlayer is laterally expanded.

Polarised Neutron Reflection measurements have been made on Ag/Cr/Ag sandwich structures with varying thicknesses of Cr. It is shown that for Cr thicknesses of 2 and 3.3ML the Cr is ordered non-ferromagnetically and it is proposed that at these thicknesses the Cr has reverted to its bulk antiferromagnetic order. However measurements on samples with Cr thicknesses of 0.33ML indicate ferromagnetic ordering with a greatly enhanced magnetic moment per atom over the bulk Cr value, in partial agreement with previous theoretical predictions. PNR measurements on a Ag/Fe/Ag(001) structure with thickness of Fe of 8ML have yielded an accurate measurement of the magnetic moment per atom for the Fe film of  $1.0 \pm 0.15\mu_B$ , indicating a reduced value from that of bulk Fe of  $2.22\mu_B$ .

X-ray scattering from a Ge(001) surface has been used to show that the surface undergoes a reversible phase transition at  $T = 954 \pm 7K$ . It is proposed that the transition occurs due to the formation of vacancy-adatom pairs as some of the surface dimers break with increasing temperature. The data is explained in terms of a three level model used to describe the vacancy-adatom creation. The three level model results are compared with results from a simple Monte-Carlo simulation and an energy of  $0.41 \pm 0.05eV$  is deduced as the energy required to break the dimer bonds on the surface of Ge(001). Further X-ray scattering from a miscut Ge(001) surface shows that the surface is made up of regularly spaced steps of double atomic height, in agreement with theoretical and previous experimental studies. It is shown that perpendicular to the steps the reconstructed domains are limited in dimension by the steps, although both orientations of the reconstruction are possible